

MARCH 2018

Ph.D in Mechanical Engineering

HASAN DEMİRTAŞ

**UNIVERSITY OF GAZİANTEP
GRADUATE SCHOOL OF
NATURAL & APPLIED SCIENCES**

**CATHODE DESIGN FOR COMPLEX SHAPES IN
ELECTROCHEMICAL MACHINING**

**Ph.D THESIS
IN
MECHANICAL ENGINEERING**

**BY
HASAN DEMİRTAŞ
MARCH 2018**

**CATHODE DESIGN FOR COMPLEX SHAPES IN ELECTROCHEMICAL
MACHINING**

Ph.D Thesis

in

Mechanical Engineering

University of Gaziantep

Supervisor

Prof. Dr. Oğuzhan YILMAZ

Co-Supervisor

Prof. Dr. Bahattin KANBER

by

Hasan DEMİRTAŞ

March 2018



© 2018 [Hasan DEMİRTAŞ]

REPUBLIC OF TURKEY
UNIVERSITY OF GAZİANTEP
GRADUATE SCHOOL OF NATURAL & APPLIED SCIENCES
MECHANICAL ENGINEERING

Name of the thesis: Cathode Design for Complex Shapes in Electrochemical Machining

Name of the student: Hasan DEMİRTAŞ

Exam date: 26/03/2018

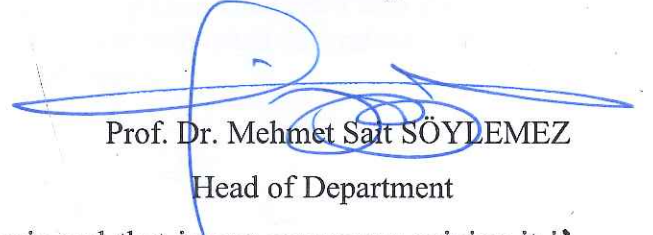
Approval of the Graduate School of Natural and Applied Sciences



Prof. Dr. Ahmet Necmeddin YAZICI

Director

I certify that this thesis satisfies all the requirements as a thesis for the degree of Doctor of Philosophy.



Prof. Dr. Mehmet Sait SÖYLEMEZ

Head of Department

This is to certify that we have read this thesis and that in our consensus opinion it is fully adequate, in scope and quality, as a thesis for the degree of Doctor of Philosophy.



Prof. Dr. Bahattin KANBER

Co-Supervisor



Prof. Dr. Oğuzhan YILMAZ

Supervisor

Examining Committee Members

Prof. Dr. Ömer EYERCİOĞLU

Prof. Dr. Metin BEDİR

Prof. Dr. Ömer KELEŞ

Prof. Dr. Rahmi ÜNAL

Prof. Dr. Oğuzhan YILMAZ

Signature



I hereby declare that all information in this document has been obtained and presented in accordance with academic rules and ethical conduct. I also declare that, as required by these rules and conduct, I have fully cited and referenced all material and results that are not original to this work.

Hasan DEMİRTAŞ

ABSTRACT

CATHODE DESIGN FOR COMPLEX SHAPES IN ELECTROCHEMICAL MACHINING

DEMİRTAŞ, Hasan

Ph.D. in Mechanical Engineering

Supervisor: Prof. Dr. Oğuzhan YILMAZ

Co-Supervisor: Prof. Dr. Bahattin KANBER

March 2018

122 pages

Electrochemical machining (ECM) is one of the most efficient nontraditional machining processes to provide bright surface finish, machining difficult to cut materials and manufacturing complex shapes. However, due to some challenges like the lack of dimensional accuracy, process control and monitoring and environmental factors, implementation of ECM process has been limited. This study presents a mathematical model to design cathode surfaces for machining freeform surfaces. This mathematical model is based on solving 3D Laplace equation by using Finite Element Method (FEM) to determine the potential distribution between the anode and cathode surfaces. A desktop size electrochemical (EC) machine was designed and constructed to carry out the experimental works. Experimental studies were carried out on AISI 1040 carbon steel using copper, brass and stainless steel as cathodes. Nine different cathodes have been designed via feed rate and electrical conductivity variables to investigate the validity of this mathematical model. A 3D scanner was used to measure and compare of the electrochemical machined anode surfaces with the CAD model. The experimental results showed that *NaCl* type electrolyte cause over machining at the edge where the electrolyte transferred to the gap domain. In the middle of gap domain similar dimensional error (DE) values have been obtained due to well-made electrolyte transition. From the 3D scanned machined surfaces, it has been observed that higher value of electrical conductivity with higher feed rate has been producing a more accurate shape. Furthermore, three different ECM freeform surface drawbacks investigated and designed control mechanisms have been presented.

Keywords: ECM, FEM, cathode design, freeform surface.

ÖZET

ELEKTROKİMYASAL İŞLEME YÖNTEMİNDE KARMAŞIK ŞEKİLLER İÇİN KATOT TASARIMI

DEMİRTAŞ, Hasan

Doktora Tezi, Makine Müh. Bölümü

Tez Yöneticisi: Prof. Dr. Oğuzhan YILMAZ

Yardımcı Tez Yöneticisi: Prof. Dr. Bahattin KANBER

Mart 2018

122 sayfa

Elektrokimyasal İşleme (EKİ) yöntemi; parlak yüzey sonlandırma, işlenmesi zor malzemelerin üretimi ve karmaşık şekillerin imalatı için en etkili alışılmamış imalat yöntemlerinden biridir. Ancak boyutsal hassasiyetin gerçekleştirilememesi, işlem sürecinin kontrolü ve çevresel faktörler gibi bazı zorluklardan dolayı EKİ yönteminin kullanılabilirliği sınırlıdır. Bu çalışmada serbest formlu yüzeylerin işlenmesinde kullanılacak olan katot tasarımı için bir matematiksel model sunulmuştur. Bu matematiksel model anot ve katot arasındaki potansiyel dağılımının tespiti için Sonlu Elemanlar Yöntemi (SEY) kullanarak üç boyutlu Laplace denkleminin çözülmesi prensibine dayanmaktadır. Deneysel çalışmaların yapılabilmesi için masaüstü boyutlarda bir EKİ tezgahı tasarlanmış ve imal edilmiştir. Deneysel çalışmalarda AISI 1040 karbon çeliği anot malzemesi, bakır pirinç ve paslanmaz çelik ise katot malzemesi olarak kullanılmıştır. İlerleme hızı ve elektrik iletkenlik katsayısı gibi değişkenler kullanılarak dokuz farklı katot tasarlanarak matematiksel modelin geçerliliği incelenmiştir. EKİ yöntemi uygulanmış anot yüzeyleri bir üç boyutlu tarayıcı kullanılarak yüzey ölçümleri ve CAD model ile karşılaştırmaları yapılmıştır. Deneysel çalışmalarda, NaCl tip elektrolitin işlem bölgesine transferinin yapıldığı bölgelerde aşırı işleme oluşturduğu gözlemlenmiştir. İşlem bölgesinin orta kısımlarında ise düzgün yapılan elektrolit iletiminden dolayı boyutsal hata değerlerinin benzer çıktığı tespit edilmiştir. Üç boyutlu taranmış yüzeyler incelendiğinde, yüksek elektrik iletkenliği ve yüksek ilerleme hızlarında daha hassas şekiller oluşturulduğu gözlenmiştir. Buna ek olarak serbest form yüzeylerin işlenmesi sırasında karşılaşılan üç farklı zorluk incelenmiş olup, tasarlanmış olan kontrol mekanizmaları sunulmuştur.

Anahtar Kelimeler: EKİ, SEY, katot tasarımı, serbest formlu yüzeyler



To My Family

ACKNOWLEDGEMENTS

The author wishes to express his deepest gratitude to his supervisor Prof. Dr. Oğuzhan YILMAZ and co-supervisor Prof. Dr. Bahattin KANBER for their guidance, advice, criticism, encouragements and insight throughout the research.

The author would also like to thank Prof. Dr. Ömer EYERCİOĞLU, Prof. Dr. Metin BEDİR, Prof. Dr. Ömer KELEŞ, Prof. Dr. Rahmi ÜNAL and Prof. Dr. Oğuzhan YILMAZ for serving on the committee and their valuable suggestions and comments.

Last but not least, I want to express my sincere appreciation to my wife, Selma and our lovely kids, Zümra, İzgi and Bilge for their love, understanding, patience and support. Also, all gratitude and appreciation to my parents.

This study was supported by the Gaziantep University Scientific Research Project (BAP) Department [grant number MF.14.19].

TABLE OF CONTENTS

	Pages
ABSTRACT	v
ÖZET	vi
ACKNOWLEDGEMENTS	viii
TABLE OF CONTENTS	ix
LIST OF TABLES	xiii
LIST OF FIGURES	xiv
LIST OF SYMBOLS	xviii
CHAPTER 1	1
INTRODUCTION	1
1.1 Introduction	1
1.2 Statement of the Problem	3
1.3 Aim of the Thesis	4
1.4 Research Objectives and Tasks	4
1.5 Structure of the Thesis.....	5
CHAPTER 2	7
LITERATURE REVIEW	7
2.1 Introduction	7
2.2 Cathode Design	9
2.3 Electrochemical Machining Process	12
2.4 Process Parameters Effects on ECM.....	13
2.4.1 Static Parameters	13

2.4.2	Dynamic Parameters	17
2.5	Drawbacks of ECM	20
CHAPTER 3	22
MATHEMATICAL AND FINITE ELEMENT MODELLING OF FREE-FORM CATHODE SURFACE.....		22
3.1	Introduction	22
3.2	Mathematical Modelling of a Free-form Surface	22
3.2.1	B-Spline Curves	23
3.2.2	Knot Vectors	24
3.3	Mathematical Modelling of Cathode surface	25
3.4	Finite Element Modelling of Cathode Surface	27
3.5	Case Study	33
CHAPTER 4	39
ELECTROCHEMICAL MACHINE DESIGN AND CONSTRUCTION		39
4.1	Introduction	39
4.2	Electrochemical Machine Setup	39
4.2.1	EC Machine Base	40
4.2.2	Direct Current (DC) Power Supply	43
4.2.3	Electrolyte Control Unit	44
4.3	Case Study: Electrochemical Drilling	45
4.3.1	Effect of Voltage	47
4.3.2	Effect of Feed Rate	49
4.3.3	Effect of Initial Gap	51
CHAPTER 5	54
EXPERIMENTAL STUDY.....		54
5.1	Introduction	54
5.2	Experimental Procedure	54

5.3	Mathematical Modelling of the Cathode Surface.....	55
5.4	Materials and Methods	58
5.4.1	Electrolytes.....	58
5.4.2	Anode and Cathode Material	59
5.5	Equipment and Instrumentation	61
5.5.1	EC Machine.....	61
5.5.2	Electrical Conductivity Measurements	61
5.5.3	Material Removal Rate Measurements	61
5.5.4	Surface Measurements	62
CHAPTER 6		63
VERIFICATION OF ELECTROCHEMICAL MACHINED (ECMed) FREE-FORM SURFACES.....		63
6.1	Introduction	63
6.2	Drawbacks of Free-Form Surface Machining	63
6.2.1	Effect of Short Circuiting.....	63
6.2.2	Effects of Cavitation	65
6.2.3	Effect of Oxide Layer.....	67
6.2.4	Short Circuit Control.....	68
6.2.5	Cavitation Control	69
6.2.6	Oxide Layer Control	75
6.3	Cathode Design Considerations	75
6.3.1	Effect of the Electrolyte	78
6.3.2	Effect of Feed Rate.....	86
6.3.3	Effect of Electrical Conductivity	88
6.3.4	Effect of Vf/kc	90
CHAPTER 7		93
CONCLUSIONS AND FUTURE WORKS		93

7.1	Conclusions	93
7.2	Future Works	96
	REFERENCES	98
	APPENDIX	105
	Appendix A: Flow Chart of Developed Computer Program.....	106
	Appendix B: Developed Mathematica Program.....	107
	Appendix C: Variation of DE Along u Direction for Experimental Conditions.....	116
	CURRICULUM VITAE	121



LIST OF TABLES

	Pages
Table 1.1 MRR values for different machining processes [4]	3
Table 3.1 Skewness values for mesh quality	35
Table 3.2 ECM process parameters	36
Table 3.3 FEM parameters for the freeform surface	36
Table 3.4 Potential distribution inside the gap domain	37
Table 4.1 Specifications of the EC machine base	40
Table 4.2 Specifications of the DC power supply	43
Table 4.3 Specifications of the AC drive	45
Table 4.4 Experimental conditions	46
Table 5.1 Experimental Conditions	55
Table 5.2 Calculated θ and α angles for some points on a freeform surface	57
Table 5.3 FEM parameters for cathode design	58
Table 5.4 Electrolyte properties	58
Table 5.5 Chemical and mechanical properties of cathode materials	59
Table 5.6 Specifications of conductivity meter	61
Table 6.1 Chemical composition of 1040 carbon steel	67
Table 6.2 Parameters for ANSYS simulation	72
Table 6.3 Minimum and maximum DE for experimental conditions	77
Table 6.4 <i>MER</i> values for experimental conditions	78

LIST OF FIGURES

		Pages
Figure 1.1	Schematic of an electrolysis process	2
Figure 2.1	Diagram of electrochemical reactions during ECM of iron in sodium chloride (<i>NaCl</i>) electrolyte [3]	9
Figure 2.2	Predicted and experimental erosion profile [41].....	10
Figure 2.3	Convergence of BE values for different time intervals [46].....	11
Figure 2.4	Schematic structure of BP network for blade [47]	11
Figure 2.5	Effect of different types sludging electrolytes on <i>MRR</i> [56].....	15
Figure 2.6	Relationship between microhole diameter and tool feed rate [52]	17
Figure 2.7	Relationship between <i>MRR</i> and tool feed rate [56].....	18
Figure 2.8	Relationship between side gap (overcut) and machining voltage [80].	18
Figure 2.9	Influence of voltage on MR [41]	19
Figure 2.10	Variation of electrical conductivity of (a) NaCl and (b) H2SO4 as a function of molar concentration [81]	19
Figure 2.11	Variation of <i>MRR</i> with electrolyte concentration (Electrolyte type:NaNO3) [52]	20
Figure 3.1	Mapping of a NURBS surface	23
Figure 3.2	Representation of the biparametric coordinates for 5x4 points along the <i>u</i> and <i>v</i> directions.....	26
Figure 3.3	The angels due to normal vector	26
Figure 3.4	Solid model of the electrolyte between the anode and the cathode	27
Figure 3.5	Effect of the temperature on the electrical resistivity of the <i>NaCl</i> electrolyte for different concentrations [27].....	30
Figure 3.6	Hexahedron with eight nodes and the mapped cube.	30
Figure 3.7	Sample freeform surface	34
Figure 3.8	Free-form surface with mesh points	35

Figure 3.9	Finite element model of anode, cathode and electrolyte developed in ANSYS (Model 01)	36
Figure 3.10	Finite element model of anode, cathode and extended electrolyte developed in ANSYS (Model 02)	36
Figure 3.11	Potential distribution along the electrolyte thickness	38
Figure 4.1	Schematic of electrochemical (EC) machine.....	39
Figure 4.2	Photograph of the electrochemical machine	40
Figure 4.3	Linear motion system.....	41
Figure 4.4	Schematic of the EC machine stepper motor control system	42
Figure 4.5	Electrical cabinet of the EC machine.....	42
Figure 4.6	Machining cell	43
Figure 4.7	Specifications of the pump	44
Figure 4.8	Brass tool and the copper workpiece	45
Figure 4.9	Effect of voltage on (a) <i>MRR</i> and (b) <i>Overcut</i> for $V_f=5 \text{ mm/min}$	48
Figure 4.10	Effect of voltage on (a) <i>MRR</i> and (b) <i>Overcut</i> for $V_f=3 \text{ mm/min}$	49
Figure 4.11	Effect of feed rate on <i>MRR</i> for 10 V	50
Figure 4.12	Effect of feed rate on <i>Overcut</i> for 0.5 mm initial gap	51
Figure 4.13	Effect of initial gap on <i>MRR</i> for $V_f = 3 \text{ mm/min}$	51
Figure 4.14	Effect of initial gap on <i>Overcut</i> for (a) 5 V and for (b) $V_f=5 \text{ mm/min}$	52
Figure 4.15	Effect of initial gap on <i>Overcut</i> for $V_f = 3 \text{ mm/min}$	53
Figure 5.1	Jet engine and compressor blade with suction and pressure surfaces [102].....	56
Figure 5.2	Modelled freeform surface via control points (a) on space and (b) on surface	56
Figure 5.3	Anode and trial cathode surface with layers	57
Figure 5.4	Drawing (a) and photographic view (b) of the anode.....	59
Figure 5.5	Drawing (a) and photographic view (b) of the cathode.....	60
Figure 5.6	Surface measurement reports of prepared anode and cathode surfaces	60

Figure 5.7	Photographic view of (a) conductivity meter and (b) multimeter	61
Figure 5.8	Photographic view of Radwag balance.....	62
Figure 5.9	Photographic view of 3D scanner	62
Figure 6.1	Short circuit occurrence	64
Figure 6.2	Short-circuit control system.....	64
Figure 6.3	Schematic of apparatus for electrolyte transfer	66
Figure 6.4	Photographic view of (a) apparatus 1, (b) apparatus 2, (c) apparatus 3 and (d) apparatus 4.....	66
Figure 6.5	Variation of voltage (a) and current (b) for different feed rates	68
Figure 6.6	Damaged cathode surface due to short-circuiting.....	69
Figure 6.7	Flow chart of the short-circuit control system.....	70
Figure 6.8	Electrochemical machined surfaces of apparatus 1 (a), apparatus 2 (b) and apparatus 3 (c)	71
Figure 6.9	Average velocity vs. number of elements for all pieces of apparatus ..	71
Figure 6.10	Velocity distribution via ANSYS simulation for apparatus 1	72
Figure 6.11	Velocity distribution via ANSYS simulation for apparatus 3	73
Figure 6.12	Velocity distribution for apparatus 4	73
Figure 6.13	Edges of gap domain: CD is the input edge, AB is the output edge.....	74
Figure 6.14	Variation of velocity along (a) CD edge and (b) AB edge	74
Figure 6.15	Electrochemical machined surface with oxide layer (a) and without oxide layer (b)	75
Figure 6.16	Schematic of DE measurement.....	76
Figure 6.17	The u and v directions of the workpiece surface.....	77
Figure 6.18	Variation of DE with the u and v directions for experimental conditions	82
Figure 6.19	Schematic of the over-machining phenomenon during electrolyte transition.....	83
Figure 6.20	Variation of DE with the u direction for (a) Group 1 for $v = 1$ and (b) Group 2 for $v = 0$	84
Figure 6.21	Schematic of electrolyte transition via (a) left and (b) right edges.....	85
Figure 6.22	Variation of (a) α and (b) θ angels with u direction for left and right edges	86

Figure 6.23	Variation of DE with the u direction for different feed rates (for $v = 0.5$).....	88
Figure 6.24	Variation of DE with the u direction for differing electrical conductivity (for $v = 0.5$)	90
Figure 6.25	Variation of Vf/kc with (a) average DE and (b) standard deviation various values of electrical conductivity.....	92



LIST OF SYMBOLS

C	Column vector for anode surface control points
d_m	Machining depth
DE	Dimensional error
e	Element number
I	Current
J	Jacobian matrix
K	Stiffness matrix
k, l	Orders of B-Spline basis functions
k_{ii}	Global stiffness matrix component
k_c	Electrical conductivity of the electrolyte
k_v	Electrochemical machinability of the anode material
L_C	Characteristic length of the geometry
M	Mass amount of the substance liberated at any electrode
MER	Machining error rate
MRR	Material removal rate
m	Node number
m_{dw}	Mass of distilled water
$m_{el.}$	Mass of electrolyte
m_s	Mass of salt
m_{uw}	Not machined workpiece mass
m_{mw}	Machined workpiece mass
N	Shape function

n	Normal vector of control points
P_{ij}	Three-dimensional control net vertices
P_{∞}	Reference pressure of the electrolyte
P_V	Vapor pressure of the electrolyte
Q	Cavitation number
Q_i	Incipient cavitation
R	Resistance of a circuit
Re	Reynolds number
S	Surface area of a hexahedron element
$S(u, v)$	NURBS surface function
$S_u(u, v)$	Derivative of $S(u, v)$ along u direction
$S_v(u, v)$	Derivative of $S(u, v)$ along v direction
T	Non-rotational basis function
t	Layer number
t_m	Machining time
U	Applied voltage
u, v	The biparametric directions
V	Voltage
V_U	Upstream velocity of the fluid
V_f	Feed rate of cathode
V_{∞}	Reference velocity of the electrolyte
w_{ij}	The weight of the P_{ij}
X_e, Y_e, Z_e	Transformation functions for mapping the hexahedron element
x_a	Coordinate of control points on anode surface along x coordinates
x_c	Coordinate of control points on trial cathode surface along x coordinates
y_a	Coordinate of control points on anode surface along y coordinates

y_c	Coordinate of control points on trial cathode surface along y coordinates
z_a	Coordinate of control points on anode surface along z coordinates
z_c	Coordinate of control points on trial cathode surface along z coordinates
α	Angle between the normal vector's project on $x - y$ plane and y direction
γ	Skewness ratio of a hexahedron element
θ	Angle between the z direction and normal vector
μ	Dynamic viscosity of the fluid
ξ, η, ζ	Global coordinate system directions
ρ	Density of the fluid
ρ_w	Density of the workpiece material
φ	Electric potential

CHAPTER 1

INTRODUCTION

1.1 Introduction

Manufacturing methods use various techniques to shape materials to the required geometries and forms. In a broad sense, these methods have been classified as material removal, additive and forming processes. Depending upon the material's properties, geometry, dimensions and accuracy, a manufacturing method is chosen intuitively or based on the experience. In the past two decades, new manufacturing methods have been developed and have emerged in the manufacturing industry since new high-tech materials have been introduced, part sizes are getting smaller and more accurate dimensions and tolerances are required. In addition, a reduction in the number of manufacturing processes used is always the key factor for reducing overall cost. Electrical discharge machining (EDM), electrochemical machining (ECM), electrodischarge chemical machining and grinding (EDCM and ECG), laser machining, thermal machining and water jet machining are some of the manufacturing processes that are used effectively in many industrial applications.

ECM has been used for many years as a non-traditional machining process for electrically conductive materials. Due to complexities in operation, difficult-to-control process parameters such as electrolyte, voltage, inter-electrode gap, etc. and environmental reasons, ECM has not been widely used in common industrial applications. However, ECM is a key manufacturing method for aerospace, defence and micro-manufacturing applications, since it produces very accurate surface quality, it does not leave residual stresses after machining and ECM is not limited to workpiece hardness. Thus, jet engine manufacturers such as General Electric (GE), Rolls-Royce (RR), etc. have established ECM systems for manufacturing of some engine components, particularly engine blades and blisks (bladed disks). If the geometry of these components and their dimensional accuracies are considered, cathode design as

well as control of other process parameters will play a great role in the manufacturing of these components by increasing ECM accuracy.

The first ECM process was patented by Gusseff in the late 1920s. As the opposite of electrode position process ECM was confirmed as a manufacturing method in the late 1950s. ECM is capable of machining complex hard materials such as super alloys, carbides and composites. This makes ECM an important manufacturing method in the die and mould making, nuclear, aircraft and aerospace industries [1, 2].

ECM's material removal mechanism is based on Faraday's laws of electrolysis. Electrolysis is a chemical process that takes place when electron transfer occurs between two electrodes in a liquid solution. Figure 1.1 shows a schematic representation of an electrolysis process.

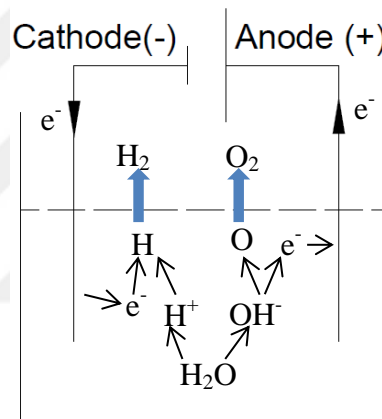


Figure 1.1 Schematic of an electrolysis process

For this type of machining, the tool (cathode) and workpiece (anode) are connected via the negative and positive signs of a direct current (DC) power supply, respectively. DC power supply has capacity at a high current ranges from 50–40000 A and a low voltage of 5–30 V. A liquid with electrical conductivity, called an electrolyte, is transferred into the gap between the anode and the cathode at high velocity. The electrolyte removes the dissolution products, such as metal hydroxides, heat and gas bubbles that are generated between anode and cathode [3]. As a variable parameter, the electrolyte will be discussed in Section 2.4.1.1. Chemical reactions occur on the anode surface via electron transfer from the cathode to the anode and the anode surface is machined in an atomic scale in these chemical reactions.

1.2 Statement of the Problem

Turbomachinery systems such as aero engines, stationary gas and steam turbines as well as turbochargers for engines can be manufactured by different machining process. ECM, EDM and 5 axis milling machines are the most encountered machining process to manufacture turbomachinery components.

Table 1.1 MRR values for different machining processes [4]

	<i>MRR (mm³/min)</i>	
	Ti-6Al-4V	Inconel 718
Milling	6035	3401
EDM	220	500
ECM	4838	4163

Table 1.1 shows the *MRR* values for two different materials that are widely used in aerospace industry. ECM and EDM are non-mechanical machining process unlike milling operations. As can be seen from Table 1.1 ECM is more effective to machine hard-to-cut materials than EDM. Additionally, ECM is the most effective process to machine Inconel 718. In ECM high material removal rates can be realized at best surface qualities without developing any white layer or heat affected zone. In addition to that via ECM it is possible to achieve finished surfaces qualities during rough machining operations, which saves the need for further treatment like cost-intensive finish milling steps or polishing operations [5, 6]. But due to cost-intensive tool pre-developing processes and rather high investment costs for the machine tools, ECM is mostly used in large scale productions [7].

The complex interactions of the ECM characteristics are still not completely understood. Therefore, it is very difficult to achieve a good surface accuracy particularly for the shaping of free-form surfaces. Trial and error seems to be the only way to accomplish this but this is a time-consuming process and increases the cost. Extensive research efforts and continuing advancements in technologies required for the improvements in ECM tool design, monitoring and control, electrolyte processing and disposal, process accuracy and power supply are expected to further enhance the industrial applications of ECM technology.

1.3 Aim of the Thesis

This research work aims to design electrode (cathode) shapes for complex geometry surfaces for ECM applications. Complex geometries mainly cover free-form surfaces having a variant radius of curvatures along the surface. This may lead to accurate control of the potential difference between electrode and workpiece, electrolyte flow rate and gap distance during ECM process. Therefore, electrode design considering the above parameters is crucial for producing the correct form for workpiece shapes with the required curvatures. The surface identification and potential distribution must therefore be determined. The surface identification will be determined with Non-Uniform Rational B-spline Surface (NURBS) surface modelling and potential distribution within the gap will be determined using the Laplace equation and the finite element method (FEM).

The parameters used in ECM must be controlled and optimised with the cathode design. Hence, the construction of an ECM machine has an important role in this research. With this machine, different values for different parameters will be applied to machine the workpieces that are widely used for ECM machining. In this way, the effects of the process parameters can be determined for cathode design and machining.

1.4 Research Objectives and Tasks

To achieve the goals and objectives, the following research tasks were carried out:

- Reviewing the related literature on ECM, ECM process parameters, cathode design and micro-ECM
- Surface modelling of cathode shape
 - Mathematical background of NURBS surfaces
 - Simple NURBS surface modelling
 - Free-form NURBS surface modelling
- Numerical solution to determine the electrode geometry
 - Simple surfaces
 - Finite element modelling in Mathematica (provided by wolfram in Oxfordshire, UK).
 - Solution of FE model
 - Free-form surfaces

- Finite element modelling in Mathematica
 - Solution of FE model
- Miniature ECM machine design and construction for micro and macro applications
 - Designing of the machine structure
 - Designing of the electrolyte control unit
 - Designing of DC power supply
 - Construction of the ECM machine
- Experimental works
- Drawbacks of free-form surface machining in ECM
 - Short circuiting
 - Cavitation
 - Oxide layer
- Design of control mechanisms for drawbacks
 - Short circuiting
 - Cavitation
 - Oxide layer
- Analysis of experimental and theoretical results

1.5 Structure of the Thesis

This thesis presents a FEM model for cathode design of free-form surface applications, design and construction of an EC machine, some drawbacks of freeform surface machining and control mechanisms and analysis of experimental and theoretical results.

This thesis comprises four main sections:

- Cathode modelling
- EC machine design and construction
- Drawbacks of freeform surface machining and control mechanisms
- Analysis of experimental and theoretical results

This content is provided in eight chapters.

The first chapter introduces the subject. This chapter states the problem, aim and objective of the thesis.

The second part of the thesis deals entirely with the state of the technology. Readers can find a review related to ECM, EC machine construction, ECM parameters, cathode design and drawbacks of free-form surface machining in the literature.

The third chapter of the thesis is related to modelling of free-form cathode surfaces. The chapter outlines NURBS and FEM types for modelling surfaces and potential distribution between anode and cathode, respectively. In addition, this chapter provides several case studies for designing flat and simple free-form surfaces.

The fourth chapter describes electrochemical machine design and construction, giving details about the design and manufacture of a desktop-sized EC machine specifically to conduct the experimental work in this thesis. The selection criteria for ECM components are also highlighted in this chapter. In addition, the capabilities of the machines are identified through a series of preliminary experiments.

The fifth chapter describes the experiments that were performed. Experimental procedures and FEM results are given in this chapter. The chapter also provides an introduction to the equipment and instrumentation.

The sixth chapter details the drawbacks of machining of freeform surfaces. Drawbacks are categorised into three main groups: short circuiting, cavitation and oxide layer. This chapter also describes the control mechanisms to prevent these drawbacks. The chapter presents the experimental results and analysis of the work conducted to verify the mathematical model that is presented in Chapter Three. A discussion of the work conducted is presented in detail.

The final chapter provides the conclusions, discussions and considerations about the study. In addition, the potential future work is also described in this chapter.

CHAPTER 2

LITERATURE REVIEW

2.1 Introduction

ECM is a non-traditional machining process of which the theory is based on Faraday's laws of electrolysis. According to the law, the electron flow from one electrode to another (connected to a direct current power supply) is obtained with the help of an electrical conductive liquid [3]. In the ECM process, a workpiece and tool (electrode) are considered as anode and cathode, which are charged as positive and negative poles, respectively. In the machining mechanism, the material is removed from the anode without a contact between the anode and cathode. The liquid is called an electrolyte. It is pumped through the machining gap between the anode and cathode while direct current is passed through the gap at a low voltage to dissolve metal from the anode. ECM is more advantageous than conventional machining in some cases such as ECM can be applicable regardless of material hardness, tool wear and cutting forces. In fact, ECM is very useful for producing a bright surface finish; it is preferred for machining difficult-to-cut materials and manufacturing complex geometry components [8].

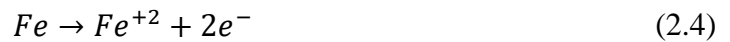
During ECM, chemical reactions occur between the anode and the cathode with the help of electrolyte. For machining of a steel containing mainly iron, generally a sludge type electrolyte sodium chloride (*NaCl*) is used. When voltage is applied, dissolution of water and *NaCl* occurs, as given in Eqs. 2.1 and 2.2.



Negative and positive ions move through the anode (workpiece) and the cathode (tool) respectively, via applied potential difference. Thus, the hydrogen ions remove electrons from the cathode and form hydrogen gas as:



Similarly, the iron atoms come out of the anode as:



within the electrolyte, iron ions combine with chloride ions to form iron chloride ($FeCl_2$); similarly, sodium ions combine with hydroxyl ions to form sodium hydroxide ($NaOH$):



In practice, $FeCl_2$ and $Fe(OH)_2$ form and are precipitated in the form of sludge. In this manner, the workpiece is gradually machined and is precipitated as the sludge. Moreover, there is no coating on the tool, only hydrogen gas evolving at the tool or cathode. Figure 2.1 shows the electrochemical reactions schematically. As the material removal takes place due to atomic level dissociation, the machined surface is of excellent surface finish and is stress free. With this metal-electrolyte combination, the electrolysis has involved the dissolution of iron from the anode, and the generation of hydrogen at the cathode. No other actions take place at the electrodes.

Due to the lack of contact between the anode and cathode that is discussed above, ECM has the following advantages: applicability to the machined materials with regard to their mechanical properties (hardness, elasticity, etc.), no tool wear and the ability to obtain stress-free surfaces. Therefore, ECM has found wider application and increasing acceptance in a variety of industries, from automobile manufacturing to defence [9-25].

The complex interactions of the ECM characteristics are still not completely understood. Therefore, it is very difficult to achieve good surface accuracy; trial and error seems to be the only way to accomplish this. This is a time-consuming process and increases the cost. Extensive research efforts and continuing advancements in technologies required for improvements in ECM tool design, monitoring and control, electrolyte processing and disposal, process accuracy and power supply are expected to further enhance the industrial applications of ECM technology.

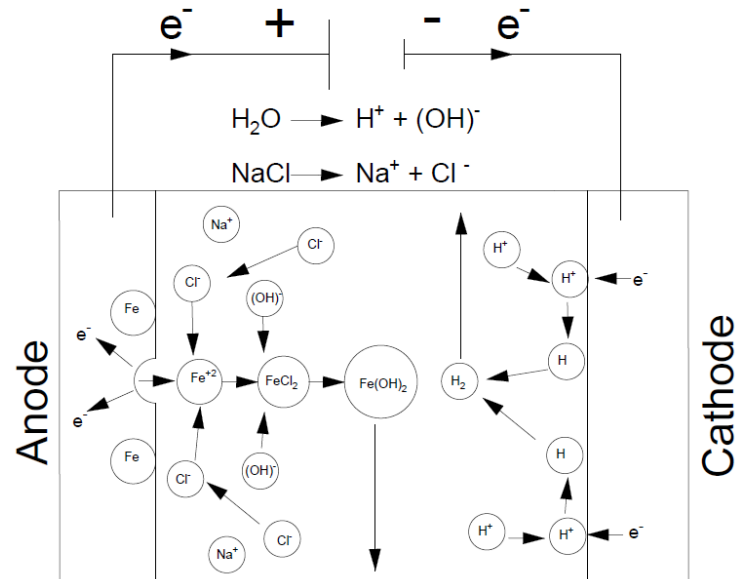


Figure 2.1 Diagram of electrochemical reactions during ECM of iron in sodium chloride (*NaCl*) electrolyte [3]

This chapter presents the literature review regarding related works to solve the problems discussed above. Section 2.2 presents works related to cathode design. Section 2.3 describes literature regarding EC machine design and construction. Section 2.4 presents ECM process parameters, categorised into static and dynamic parameters. Finally, Section 2.5 describes literature that examines the means to prevent certain drawbacks of ECM.

2.2 Cathode Design

Cathode design is an important challenge in ECM. Cathode design mainly deals with determining the tool shape that will produce a workpiece with the prescribed dimensions and accuracy. Ideally, it should be implemented by performing a simple calculation at the outset of the design procedure; however, this not yet practical due to the complex configuration of the inter-electrode gap, which is affected by many process parameters [8]. The tool is shaped to be nearly a mirror image of the machined cavity; its dimensions must be slightly different from the nominal dimensions of the cavity to allow for an overcut [26]. The tool design must permit electrolyte flow at a rate sufficient to dissipate generated heat to eliminate boiling of the electrolyte in the inter-electrode gap. To produce smooth surfaces on the workpiece, tool design must enable a uniform flow over the entire machining area. Ideally, flow should be laminar and free from eddies [27]. Given these conditions, tool design is a complex problem in ECM.

There are some studies examining ways to realise good cathode design to achieve an accurate surface. Early investigations were mainly limited to the simpler methods such as analytical, graphical, geometrical and complex variable techniques [28–31]. However, none of these methods yielded the desired accuracy owing to oversimplification of the current field in the inter-electrode gap. Rapid advancements in computer technology and numerical techniques make it possible to develop more comprehensive solutions. Some studies have been primarily directed to numerical solutions to the inverse boundary problem instead of simple geometric approximations [32–40].

Hocheng et al. [41] used the iteration integral method for 2D tool design; however, this model provides high accuracy with time and that means it cannot be used for high speed machining. The comparative results are shown in Figure 2.2.

Zhiyong et al. [42] investigated the model error between the 2D and 3D $\text{Cos}\theta$ method; their work shows the 3D method error to be less than the 2D $\text{Cos}\theta$ method.

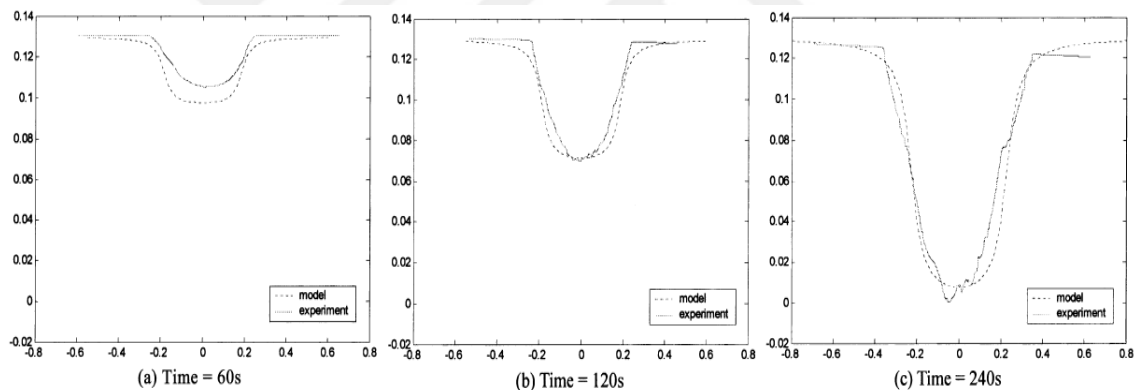


Figure 2.2 Predicted and experimental erosion profile [41]

Kozak et al. [43] used the electrochemical shaping theory to create a computer simulation for electrochemical shaping. Some studies were performed using boundary element methods (BEM) to create a computer simulation for ECM [44, 45]. Pattavanitch et al. [46] created an ECM process simulation by BEM; however, this model error increases with time. Convergence of BE values for different time intervals is shown in Figure 2.3.

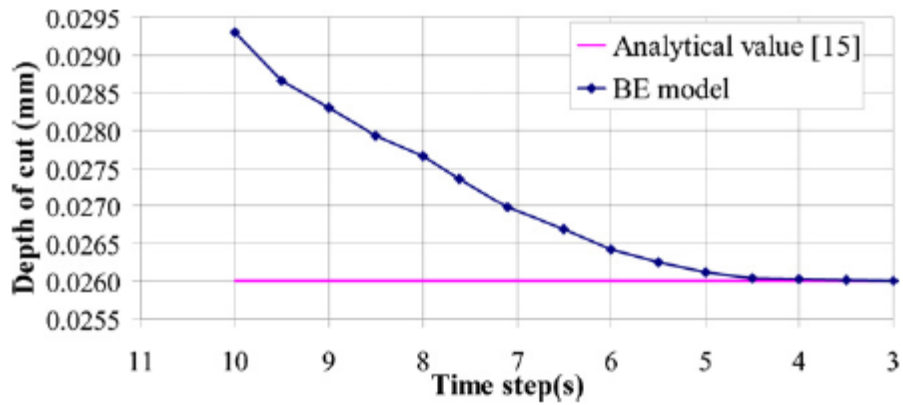


Figure 2.3 Convergence of BE values for different time intervals [46]

Zhiyong et al. [47] developed a model to machine aero-engine blades in ECM. This model is based on a Back Propagation (BP) neural network. Applied inputs are voltage, initial machining gap, feed rate of tool cathode, pressure difference between inlet and outlet of electrolyte and electrolyte temperature. The BP neural network model is shown in Figure 2.4.

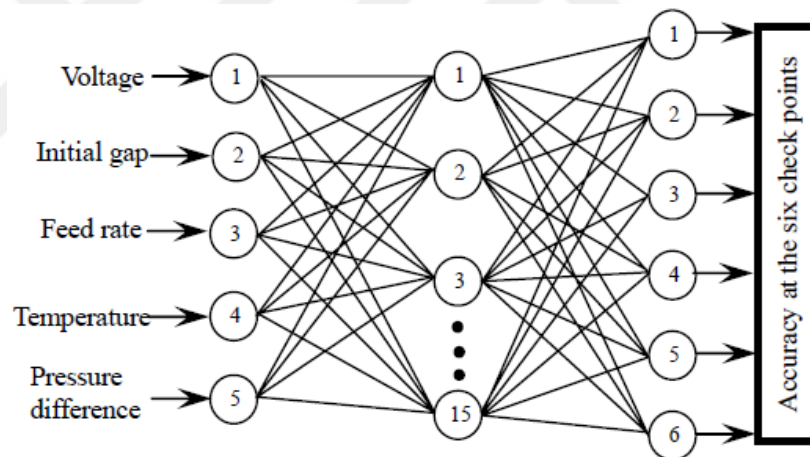


Figure 2.4 Schematic structure of BP network for blade [47]

An ECM cathode can also be designed using FEM [48–50]. Sun et al. [48] used the NURBS model to explain the workpiece surface. Cathode points were found by using electrochemical law. The distribution of electric potential within the gap in ECM was described by the Laplace equation and the gap was divided into five layers. The gap was divided into a series of elements by using the hexahedron-octonary node method. The Laplace equation was solved by using FEM to find the gap, which was used to obtain the cathode coordinates. This method possesses high computing efficiency, good accuracy and flexible boundary treatment without the need for an iterative procedure.

2.3 Electrochemical Machining Process

The literature reveals that various methods have been applied to improve the machining performance of the ECM process. Bhattacharyya et al. [50] designed an electrochemical micromachining (EMM) system in which the movement was controlled by screw and nut, the motor type was set to be stepper motor, and electrolyte concentration and voltage effects on overcut and material removal rate (*MRR*) were investigated. Li and Yuan [52] investigated the effect of pulse frequency, feed rate, voltage and electrolyte concentration on micro hole drilling of stainless steel. Movement in the system was controlled by stepper motors. Vanderauwera et al. [53] investigated the performance of macro electrochemical milling and experiments were performed on an EDM machine that was adapted for ECM milling; the results were compared to both continuous and pulsed DC machining. Thanigaivelan et al. [54] investigated the effect of acidified sodium nitrate on stainless steel. Designed experimental setup movement made on one axis and stepper motors were adjusted by microcontroller. Malapati and Bhattacharyya [55] designed an EMM system having a gantry moving bridge of type X-Y-Z, with the movement of the stage and axes controlled by stepper motors that were, in turn, controlled by a controller unit. Neto et al. [56] investigated the effects of feed rate, voltage and electrolyte types on overcut and *MRR* for ECM. According to this study, the feed rate has a greater influence than the other parameters. Mukherjee et al. [57] modelled the amount of *MRR* due to overvoltage and compared the results for the following parameters: equilibrium machining gap, feed rate, voltage and current density. *MRR* was found to be proportional with current density and inversely proportional with over voltage. Costa and Hutchings [58] presented a method for texturing metallic surfaces using ECM; their experiments show that the gap distance between the tool and the workpiece allow good flushing conditions with low *MRR*. To increase the *MRR*, gap distance can be decreased with increased electrolyte flow rate. Tehrani and Atkinson [59] investigated the pulsed voltage effect on electrochemical grinding (ECG) of two different materials, die steel and type 304 stainless steel. Under conditions in which an overcut of 0.03 mm is expected in conventional ECG using pulsed voltage, zero overcut was obtained.

2.4 Process Parameters Effects on ECM

The process parameters of ECM can be classified into two categories: static parameters, in which the parameters are set prior to the process once and dynamic parameters, which can be changed according to system the response.

2.4.1 Static Parameters

2.4.1.1 Electrolyte Type

As an important parameter, the electrolyte has three main functions in ECM: (i) to carry the current between the workpiece and the tool; (ii) to remove the products of the reaction from the machining area; (iii) to prevent the heat production of the operation while machining [27].

Therefore, the electrolyte must have some specific properties to ensure the conditions discussed above:

- High electrical conductivity to ensure high current density
- Low viscosity to ensure good flow conditions in an extremely narrow interelectrode gap
- High specific heat and thermal conductivity to be capable of removing the heat generated from the gap
- Resistance to the formation of a passive film on the workpiece surface
- High chemical stability
- High current efficiency and low throwing power
- Nontoxic and noncorrosive to the machine parts
- Inexpensive and available [27].

The choice of the electrolyte supply method depends on the part geometry, machining method, required accuracy and surface finish. Typical electrolyte conditions in the gap include a pressure of 70–2800 kPa and a maximum electrolyte velocity of 25–60 m/s [27].

Hourng and Chang [60] used a one-dimensional bubbly two-phase flow model [57] to simulate the flow field during electrochemical drilling and compared the experimental and simulation results. Experiments showed that increase in flow rate caused an increase in overcut. This was attributed to reduced void fraction between the electrodes

as gas bubbles were removed rapidly from the gap with an increase in electrolyte flow flux. Experimental investigations [56, 62] revealed that an increase in flow rate boosted *MRR* due to the greater ion transfer between the tool and the workpiece. Experimental investigations also showed that with increased flow rate, better surface finish was obtained because flow streak was prevented [62, 63].

Electrolytes can be classified into two main types: sludging and nonsludging.

Sludging electrolytes are the solutions of typical salts, such as sodium chloride. In water solutions, these salts provide the high conductivity that is used in ECM applications. The water is depleted, yielding hydrogen gas and the important hydroxide ions. The hydroxide ions combine with the metal ions that are removed by ECM, thus forming insoluble reaction products or sludge [27].

Sodium chloride is the preferred salt in sludging electrolytes. It can be kept at a constant strength by adding water, which maintains a constant concentration, and its electrical conductivity is stable over a wide pH range of 4–13 [27].

In some applications, sodium chloride can be used with sodium nitrate. Sodium nitrate is another preferred salt type that is used to prepare sludging electrolytes. Sodium nitrate results in smoother finishes on aluminium or copper alloys, but it is more expensive and is more likely to cause passivity that acts as a barrier between the workpiece and the electrolyte. This can generate undesired machining on workpiece surface. Its electrochemical action is also less efficient than that of sodium chloride [27]. Compression of *NaCl* and *NaNO₃* electrolyte effects on *MRR* is shown in Figure 2.5.

Sodium chlorate salt solution has some unusual properties as an ECM electrolyte; it can therefore be used in special applications. Additional precautions must be taken with sodium chlorate because of its flammability [27].

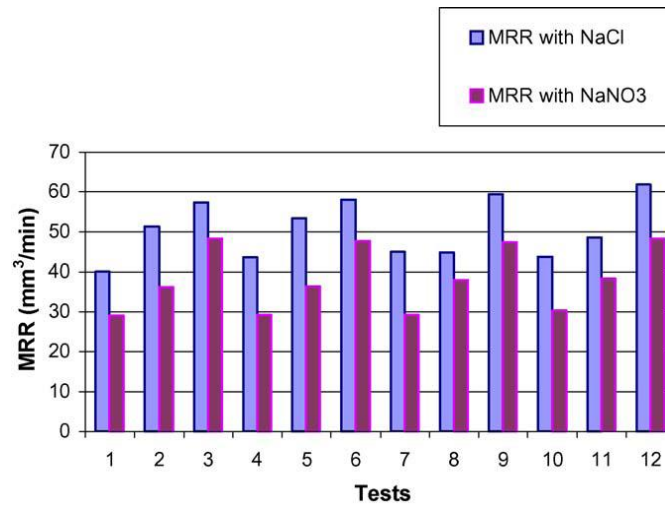


Figure 2.5 Effect of different types sludging electrolytes on *MRR* [56]

Nonsludging electrolyte strong alkali solutions (for example, *NaOH*) are used in ECM of heavy metals (such as tungsten and molybdenum) and their alloys [64-67]. This salt also provides high conductivity; however, via the sodium ions, salt is depleted and joined with metal that is removed by the ECM process. Therefore, new compounds such as sodium tungstate ($Na_2WO_4 \cdot 2H_2O$) and sodium molybdate ($Na_2MoO_4 \cdot 2H_2O$), form during the process, and the makeup of both the alkali salts and the water are required for process control. This type of ECM operation is referred to as ‘depletion mode’ because the alkali salt is depleted during the process. The new compounds in this process are quite soluble in water and heavy precipitate volumes do not occur. However, there is a tendency for the heavy metals to plate out from the solution and onto the cathode. Therefore, cathodes must be periodically cleaned because this coating is not desired in a well-controlled precision ECM process [27].

Mahdavinejad and Hatami [68, 69] observed that *NaOH* electrolytes cause higher overcut than *NaCl* electrolytes to machine steel 1.2726 materials.

Strong acids such as hydrochloric (*HCl*), nitric (*HNO₃*) and sulphuric (*H₂SO₄*) are also used in ECM. Kim et al. [66] used sulphuric acid as an electrolyte to machine stainless steel on a micro scale. But Bilgi et al. [71] reveal that the amount of *HCl* in a *NaCl* solution has a small effect on radial overcut deep-hole drilling of a super alloy.

Electrolytes can be mixed to machine different types of materials. Tang and Guo [72] used different types of electrolytes (*NaCl*, *NaNO₃*, *NaClO₃* and *NaNO₃ + NaClO₃*) in ECM of the novel special purpose S-03 stainless steel material. It was observed that a

mixed solution ($NaNO_3 + NaClO_3$) is the best choice to machine S-03 stainless steel material. $NaCl$ and $NaNO_3$ caused short circuiting and $NaClO_3$ was not preferred due to its cost. Thanigaivelan et al. [54] showed that mixing of H_2SO_4 and $NaNO_3$ gives higher *MRR* and lower overcut than a single $NaNO_3$ electrolyte on EMM of S-03 stainless steel material.

2.4.1.2 Tool Material

The metal used for a cathode or associated tooling should have electrically conductive stiffness, chemical resistivity to the electrolyte and be easy to machine.

Copper, brass, bronze, stainless steel and titanium are the most used materials for ECM tools. Titanium is especially useful when machining with an acid electrolyte that anodises it. The current can then be reversed periodically to remove plated deposits without excessive electrochemical machining of the cathode [27].

2.4.1.3 Workpiece Material

Workpieces of almost any material that has electrical conductivity can be machined by ECM. But as a specific property, electrochemical machinability of a workpiece is an important parameter for ECM. Electrochemical machinability is equal to the volume of material dissolved from the anode per unit electrical charge; this is shown in Eq. 2.6:

$$k_v = \frac{k}{\rho} \quad (2.6)$$

where ρ is the density of the workpiece and k is the electrochemical equivalent of the workpiece. For an alloy, this can be calculated by Eq. 2.7:

$$k = \frac{1}{F \sum \frac{z_i}{A_i}} \quad (2.7)$$

where i is the number of elements, A is the element's atomic weight, F is Faraday's constant (96500 C) and z is the element's valence.

The *MRR* in ECM depends on the electrochemical properties of the workpiece material (k_v). It is proportional to the total current (I).

$$MRR = k_v \cdot I \quad (2.8)$$

It is observed that shape accuracy of the electrochemical machined workpiece is better when k_v increases with increasing current density [27, 72]. Therefore, ECM is an effective method to machine super alloys that are manufactured via powder metallurgy (PM) techniques as these show the best electrochemical machinability [4].

2.4.2 Dynamic Parameters

2.4.2.1 Feed Rate

Tool feed rate, defined as the velocity of the tool traveling towards the workpiece [26], has a significant impact on the machined surface quality. Experimental investigations [59, 74, 75] have revealed that an increase in tool feed rate reduces the overcut. With an increase in tool feed rate, the void fraction increases and the electrolyte conductivity decreases, resulting in a decrease in overcut [60]. Figure 2.6 shows the effect of tool feed rate on overcut [52].

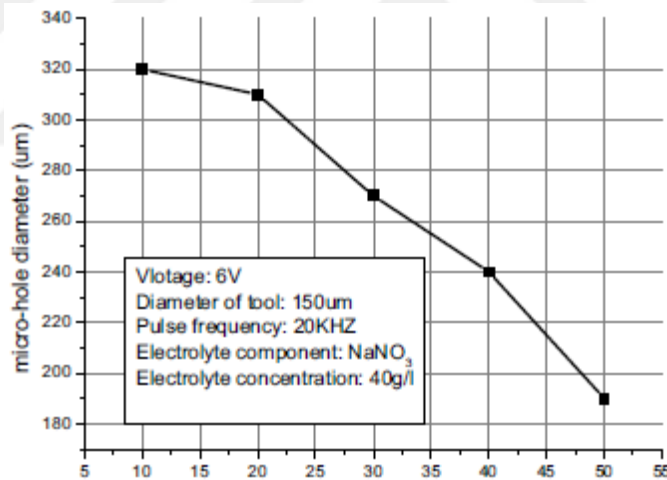


Figure 2.6 Relationship between microhole diameter and tool feed rate [52]

The distance across the frontal gap is a function of feed rate because, as the cathode is fed into the workpiece at a higher rate, the gap closes, causing resistance to drop. As can be seen in Figure 2.7, resistance drops and amperage increases; therefore, machining rate also increases until equilibrium is reached. At slower feed rates, MRR decreases as the gap increases because the cathode does not keep up with the workpiece surface. As the gap increases, the resistance rises and amperage drops [56].

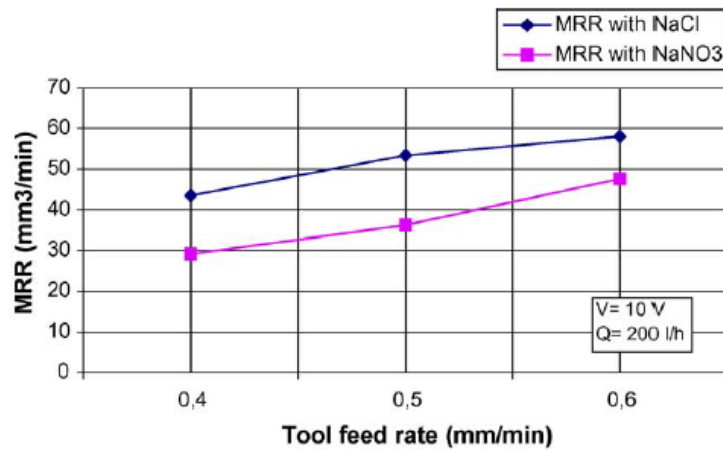


Figure 2.7 Relationship between *MRR* and tool feed rate [56]

2.4.2.2 Voltage

According to Faraday’s laws, voltage is the most effective factor for removing materials from a workpiece. The experiments conducted by many researchers [76-79] reveal that overcut increases with an increase in applied voltage. In higher voltage, electrochemical reactions generate hydrogen gas bubbles. These bubbles breakdown, resulting in the occurrence of micro-sparks. This sparking causes uncontrollable material removal in the larger area of the workpiece, which in turn produces a larger overcut [80]. Figure 2.8 shows the relationship between overcut and voltage.

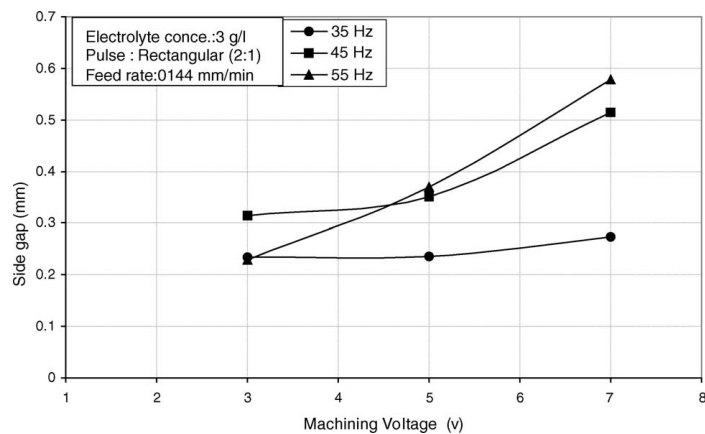


Figure 2.8 Relationship between side gap (overcut) and machining voltage [80]

Due to the increase in machining voltage, the current increases; this in turn leads to an increase in current density. According to Faraday’s laws, an increase in current density leads to an increase in chemical reaction rate. Therefore, the experiments conducted by many researchers [41, 51, 56, and 80] reveal that *MRR* increases with an increase in applied voltage. Figure 2.9 shows the influence of voltage on MR.

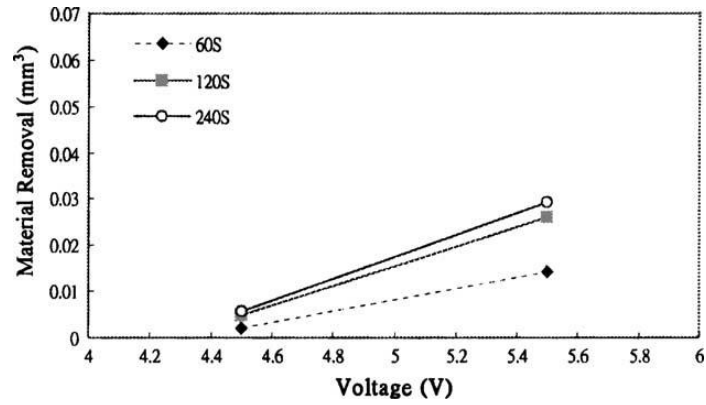


Figure 2.9 Influence of voltage on MR [41]

2.4.2.3 Electrolyte Concentration

Concentration of the electrolyte describes the amount of dissolved substance contained per unit of volume. It is associated with the electrical conductivity of the electrolyte.

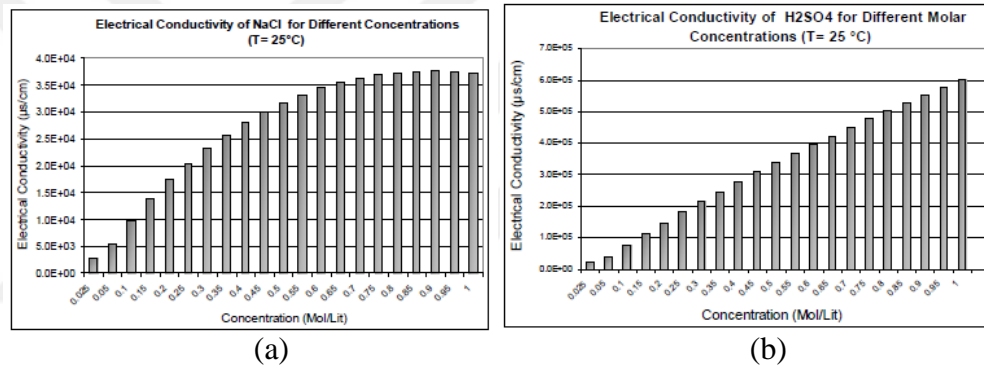


Figure 2.10 Variation of electrical conductivity of (a) NaCl and (b) H₂SO₄ as a function of molar concentration [81]

Figure 2.10 shows the influence of (a) NaCl and (b) H₂SO₄ electrolyte concentration on electrical conductivity at a constant temperature. As can be seen from Figure 2.10(b), electrical conductivity is directly proportional to electrolyte concentration.

Electrolyte concentration critically affects the hole size as the higher conductivity of the electrolyte facilitates the higher current flow, thus enhancing the removal of material. Figure 2.11 clearly illustrates that the material removal rate increases with an increase in electrolyte concentrations [52].

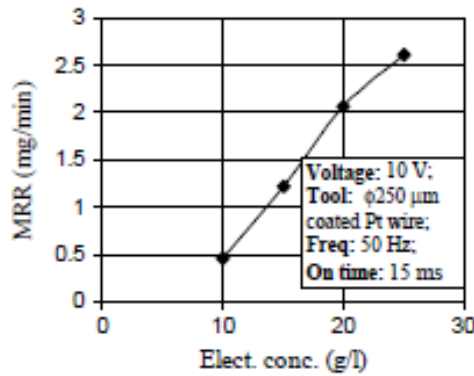


Figure 2.11 Variation of *MRR* with electrolyte concentration (Electrolyte type: NaNO_3)

[52]

2.5 Drawbacks of ECM

Short-circuiting and cavitation are critical drawbacks for ECM. Mithu et al. [79] investigated the effects of tool length, tool diameter and applied frequency on ECM issues such as the number of short circuits. Their study showed that using low frequencies during ECM prevented short circuits. Moreover, Tang and Guo [72] developed a special electrolyte composition to prevent short circuits in S-03 stainless steel. Fan et al. [83] demonstrated that NaNO_3 electrolyte types cause more short circuits and spark generation in ECM for low carbon steel. In addition, Labib et al. [84] developed a fuzzy logic control (FLC) system to prevent short-circuit formation. For electrochemical micromachining (EMM), Ghashol et al. [85] used H_2SO_4 for microhole drilling of stainless steel and observed that short circuits occurred with high electrolyte concentrations. Their study also showed that higher feed rates caused many cavitation bubbles. Furthermore, to minimise the formation of cavitation, high electrolyte pressure was suggested by Bannard [86]. The flow rate, which is an electrolyte parameter, also has an important effect on the occurrence of cavitation zones [87]. Higher voltages and frequencies cause increased cavitation formation [80].

The other important drawback for ECM is the formation of oxide layers on the anode (workpiece) surface. It has been reported that using NaCl as an electrolyte for machining of tungsten is too difficult due to the generation of an oxide layer [88]. However, this oxide layer has been used to avoid tool wear for tungsten cathodes [89]. Furthermore, Davydov et al. [90] described a drop in potential between the anode and cathode during generation of the oxide layer. For iron and iron-based alloys, different types of oxide layers have been observed. The most common oxide layers are Fe_2O_3

and Fe_3O_4 . The occurrence of oxide layers in the context of stainless steel is associated with oxygen generation [91]. It has also been reported that Fe^{2+} and Fe^{3+} formation increases with current density [92].



CHAPTER 3

MATHEMATICAL AND FINITE ELEMENT MODELLING OF FREE-FORM CATHODE SURFACE

3.1 Introduction

In chapter 2, it is seen that the modelling and control of machining accuracy are difficult issues in ECM. In this chapter, a simplified mathematical model is presented for the design of a free-form cathode surface in ECM process using FEM. A dedicated FEM algorithm was developed and implemented in Mathematica. The developed mathematical model can be applied as the symbolic and numeric computation as a hybrid method to solve the 3D Laplace equation with high precision and less computing time. Furthermore, to reduce the CPU time, nodal coordinates were transferred from local coordinates to a natural coordinate system. To increase the precision of the FEM results, mesh quality factors were considered, such as skewness ratio and aspect ratio. The developed method deals with the control points of free-form surfaces modelled through NURBS, which are obtained with a 3D computer-aided design (CAD) program; these points are then imported into Mathematica. The developed method simply uses these control points for the trial cathode shape, with consideration of the electric potential distribution between the anode and cathode surfaces; these surfaces are modelled using a 3D Laplace equation and a FEM solution.

3.2 Mathematical Modelling of a Free-form Surface

Free-form surfaces have been widely used in aerospace, automotive and die/mould industries. They are generally used to improve functional requirements. Their importance increases with the advancing technology. Thus NURBS is the best way to describe such surfaces. In CAD and computer graphics, NURBS is the most popular tool for defining curves and free-form surfaces. It can be used for many applications, from the manufacturing industry to the film industry [93]. Due to the capabilities of NURBS modelling for free-form surfaces, NURBS surfaces have been widely adapted

in CAD/CAM software and graphics applications [94]. A NURBS surface includes an intrinsic rational piecewise polynomial mapping from the 3D surface to the 2D parameter domain, as shown in Figure 3.1. Therefore, NURBS modelling is preferred for describing the anode and cathode surfaces in this work. Based on this, the anode surface is constructed and NURBS control points are obtained using 3D surface modelling software. To construct the trial cathode geometry in Mathematica, these NURBS control points are used. To obtain the optimum cathode geometry that satisfies Faraday's and Ohm's laws, a model is developed using FEM. To decrease analysis time, a natural coordinate system is used during construction of shape functions.

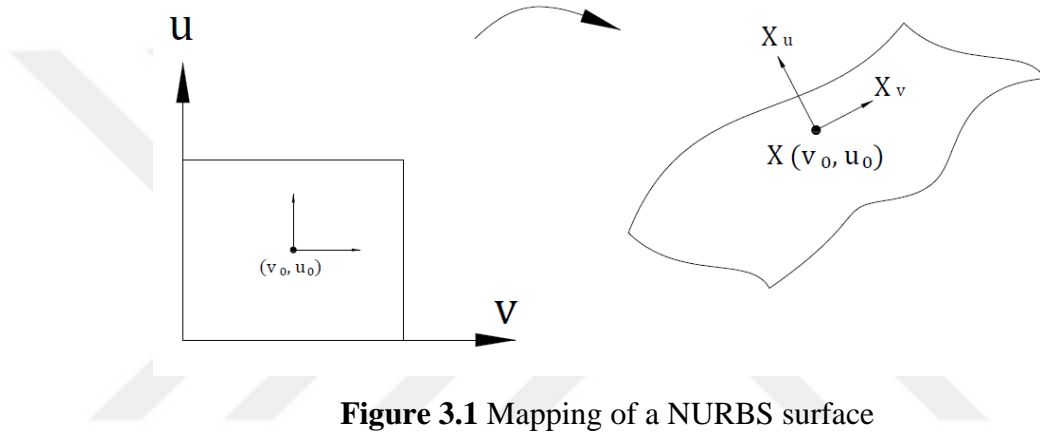


Figure 3.1 Mapping of a NURBS surface

NURBS modelling can be expressed as follows;

$$S(u, v) = \frac{\sum_{i=0}^m \sum_{j=0}^n w_{ij} P_{ij} T_{i,k}(u) T_{j,l}(v)}{\sum_{i=0}^m \sum_{j=0}^n w_{ij} T_{i,k}(u) T_{j,l}(v)} \quad (3.1)$$

where P_{ij} are the three-dimensional control net vertices, w_{ij} is the weight of the P_{ij} , u and v are the biparametric directions, $T_{i,k}(u)$ and $T_{j,l}(v)$ are the nonrotational basis functions in the biparametric u and v directions and k and l are orders of B-spline basis functions.

3.2.1 B-Spline Curves

B-splines are piecewise polynomials. They consist of separate sections of polynomial joined together at positions called knots. The joins are constructed to be as smooth as possible: degree p B-splines have $p - 1$ continuous derivatives across each knot. Given these constraints, the basis functions are uniquely defined by the property of minimal support, which in practice means they make it possible to construct a long, smooth

curve while still allowing a designer to modify only a small region at a time. This property is known as local control [94]. The base function of a B-spline can be expressed as:

$$N_{i,1}(u) = \begin{cases} 1 & \text{if } u_i \leq u \leq u_{i+1} \\ 0 & \text{otherwise} \end{cases} \quad (3.2)$$

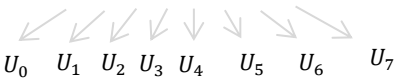
$$N_{i,p}(u) = \frac{u - u_i}{u_{i+p-1} - u_i} \cdot N_{i,p-1}(u) + \frac{u_{i+p} - u}{u_{i+p} - u_{i+1}} N_{i+1,p-1}(u) \quad p > 1 \quad (3.3)$$

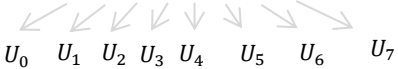
3.2.2 Knot Vectors

The collection of knots for a B-spline is known as its knot vector. To continue the analogy with a wooden spline, this corresponds to the list of positions for spline weights when measured along the spline. A non-uniform B-spline can have these knots almost arbitrarily positioned, whereas for a uniform B-spline, they must be equally spaced. All knot vectors with equal spacing are shifts and scales of each other. The effect of shifting or scaling every knot is to transform the parameter space, which is used as the domain of \mathcal{O} , but has no effect on its image. Describing a B-spline as uniform is therefore sufficient to characterise its knot vector completely [93].

$$l + 1 = (n + 1) + p \quad (3.4)$$

where $l + 1$ is the number of knots, $n + 1$ is the number of control points and p is the degree of the curve. For a uniform/periodic and nonuniform curve, the knot vector can be expressed as in Eqs. 3.5 and 3.6, respectively:

$$U = (0,1,2,3,4,5,6,7) \quad (3.5)$$


$$U = (0,3,5,3,4,2,7,7) \quad (3.6)$$


3.3 Mathematical Modelling of Cathode surface

As described in Section 3.2.1 and 3.2.2, it is difficult to identify the knots and B-spline functions. By using the surface control points, NURBS can be plotted in Mathematica, but surface function $S(u, v)$ cannot be obtained directly. Therefore, all the NURBS surface function components must be defined clearly. w_{ij} describes the point weight; for a point that on the surface, it is equal to 1. $T_{i,k}(u)$ and $T_{j,l}(v)$ are the complex functions, which change with the knots and degrees of the NURBS surface curves in the directions of u and v . To obtain the knots and curve degrees, the 'BSplineFunction' command was used. It represents a B-spline function for a curve defined by the control points. After defining the knots and curve degrees, to obtain the non-rotational basis functions $T_{i,k}(u)$ and $T_{j,l}(v)$, the 'PiecewiseExpand' and 'BSplineBasis' commands were used. 'PiecewiseExpand' expands nested piecewise functions in an expression to return a single piecewise function and 'BSplineBasis' returns the k^{th} non-uniform B-spline basis function of degree d with knots at positions u_i . 'PiecewiseExpand' can be used to expand symbolic B-Spline basis functions into explicit piecewise polynomials.

Due to NURBS surface function $S(u, v)$, the unit normal can be used to obtain the function of the normal vector for the freeform surface as follows:

$$n(u, v) = \frac{S_u(u, v) \times S_v(u, v)}{|S_u(u, v) \times S_v(u, v)|} \quad (3.7)$$

where $S_u(u, v)$ and $S_v(u, v)$ are the derivatives of the $S(u, v)$ along the u and v directions. As can be seen from Eq. 3.7, the normal vector n is a function of u and v . To obtain its numerical values at all points, u and v should have a value between 1 and 0 due to the biparametric coordinates of the model, as can be seen in Figure 3.2 ($0 \leq u \leq 1$, $0 \leq v \leq 1$). The aim of this is to describe the n function for every point due to point coordinates in a biparametric coordinate system. According to the electrochemical law, the trail coordinates of the cathode surface control points can be obtained due to anode surface control points as follows:

$$x_c = x_a - \Delta b \cdot \sin \theta \cdot \sin \alpha \quad (3.8)$$

$$y_c = y_a - \Delta b \cdot \sin \theta \cdot \cos \alpha \quad (3.9)$$

$$z_c = z_a + \Delta b \quad (3.10)$$

where Δb describes the distance along the z direction between the anode and cathode, x_a, y_a, z_a are the coordinates of the anode surface control point, θ is the angle between the feeding direction of the cathode and normal to the anode and α is the angle between the normal vector's project on the $x - y$ plane and y direction, as shown in Figure 3.3.

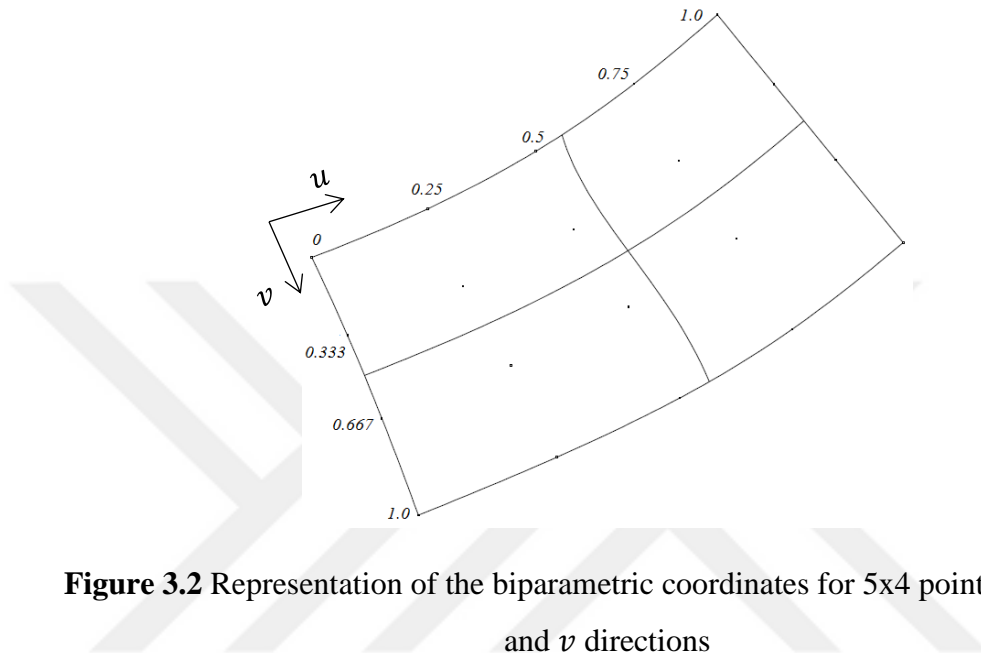


Figure 3.2 Representation of the biparametric coordinates for 5x4 points along the u and v directions

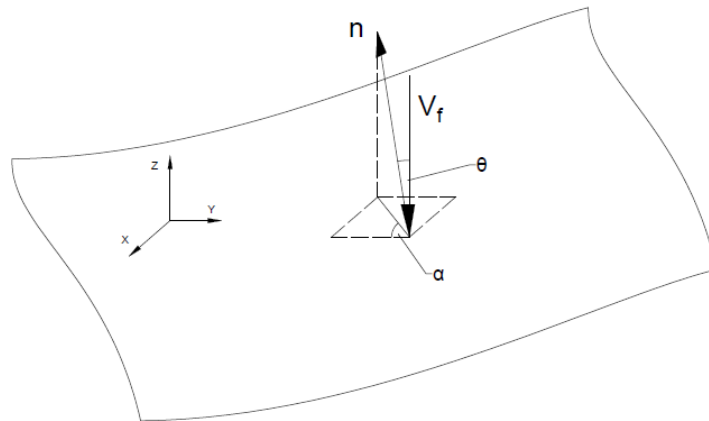


Figure 3.3 The angles due to normal vector

As can be seen from Figure 3.3, the θ and α angles associated with the components of the normal vector can be described as follows:

$$\alpha = \cos^{-1} \frac{n_x}{n_y} \quad (3.11)$$

$$\theta = \tan^{-1} \frac{\sqrt{n_x^2 + n_y^2}}{n_z} \quad (3.12)$$

3.4 Finite Element Modelling of Cathode Surface

The flow between anode and cathode was considered as a solid layer for meshing and numbering, as shown in Figure 3.4. In order to create such a solid layer, the flow within the gap had to be distributed uniformly, which is only possible in laminar flow.

$$Re = \frac{V_U \cdot L_C \cdot \rho}{\mu} \quad (3.13)$$

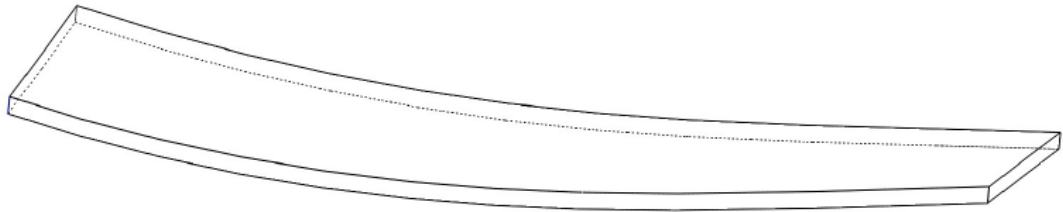


Figure 3.4 Solid model of the electrolyte between the anode and the cathode

Eq. 3.13 describes the Reynolds number that is used to characterise the different flow regimes within similar fluids, such as laminar and turbulent flow, where Re is the Reynolds number, V is the upstream velocity, L_C is the characteristic length of the geometry, ρ is the density and μ is the dynamic viscosity. For the same electrolyte velocity of the fluid (V), the flow rate defines the flow regimes; therefore, the flow rate of the electrolyte is considered to be constant.

In order to avoid the effects of over-potential and to make Faraday's law applicable for obtaining the material removal rate, some assumptions must be made. These are: (i) reaction rates of the electrode are very fast; (ii) to prevent the temperature gradient and concentration within the electrode gap, the electrolyte solution is completely mixed and (iii) machining is made by the current at the anode surface without any electrochemical machining [39]. In most ECM processes, the cathode is fed at a constant speed towards the anode so that the anode surface maintains its speed as a constant. In this situation, the distance between the anode and cathode can be accepted as a time-independent value. Therefore, the ECM system is acceptable as a quasisteady-state and free

boundary problem [48-50, 95]. According to the aforementioned assumptions, the electric potential distribution inside the gap domain can be expressed by Laplace's equation:

$$\frac{\partial^2 \varphi}{\partial x^2} + \frac{\partial^2 \varphi}{\partial y^2} + \frac{\partial^2 \varphi}{\partial z^2} = 0 \quad (3.14)$$

Due to Faraday's and Ohm's laws, anode and cathode boundaries as shown are as follows:

$$\frac{\partial \varphi}{\partial n} = \frac{V_f}{k_v * k_c} * \cos \theta \quad \left. \vphantom{\frac{\partial \varphi}{\partial n}} \right\} \text{On Anode} \quad (3.15)$$

$$\varphi_A = U \quad \left. \vphantom{\varphi_A} \right\} \quad (3.16)$$

$$\varphi_c = 0 \quad \left. \vphantom{\varphi_c} \right\} \text{On Cathode} \quad (3.17)$$

where φ describes the electric potential at each point on the anode, cathode surfaces and layers of the gap. U is the applied voltage and k_c is the electrical conductivity of the electrolyte, which is directly affected by the electrolyte temperature and concentration. The conductivity of an electrolyte changes substantially with temperature. Figure 3.5 shows the influence of temperature on the electrical resistivity of the *NaCl* electrolyte for different concentrations [27]. Any modification of the electrolyte temperature changes the electrolyte resistivity or conductivity. Based on Eq. 3.15, electrolyte conductivity was considered to be constant; therefore, the electrolyte temperature remained constant at room temperature. V_f is the feed rate of the cathode along the z direction, k_v is the electrochemical machinability of the anode material and θ is the angle between the movement direction of the cathode and normal to the anode. To satisfy the boundary conditions for the anode surface, the Laplace equation can be minimised based on the variation principle. It can be explained as follows:

$$G(\varphi) = \frac{1}{2} \int \int \int_V \left[\left(\frac{\partial \varphi}{\partial x} \right)^2 + \left(\frac{\partial \varphi}{\partial y} \right)^2 + \left(\frac{\partial \varphi}{\partial z} \right)^2 \right] dx dy dz - \int \frac{\partial \varphi}{\partial n} \varphi ds \quad (3.18)$$

A potential function $\varphi(x, y, z)$, which varies linearly inside each hexahedron element is defined as:

$$\varphi(x, y, z) = \sum_{i=1}^8 N_i(x, y, z) \cdot \varphi_i \quad (3.19)$$

where φ_i is the electrical potential for each node and N_i is the shape function for each node and for trilinear hexahedron elements in a global coordinate system. Substitution of Eq. (3.19) into Eq. (3.18) and then minimisation of $G(\varphi)$ returns the element stiffness matrix [48]:

$$K[e][i][j] = \int \int \int_{V^e} \left[\left(\frac{\partial N_i^e}{\partial x} \right) \left(\frac{\partial N_j^e}{\partial x} \right) + \left(\frac{\partial N_i^e}{\partial y} \right) \left(\frac{\partial N_j^e}{\partial y} \right) + \left(\frac{\partial N_i^e}{\partial z} \right) \left(\frac{\partial N_j^e}{\partial z} \right) \right] dV \quad (3.20)$$

where K is the element stiffness matrix and e is the element number. The solution of Eq. (3.20) requires very long CPU time. Therefore, in this study, a numerical solution is arrived at in a natural coordinate system as an isoparametric element in order to decrease the analysis time. This method has been used for solving two- and three-dimensional finite element problems with great success [93]. With using a natural (or intrinsic) coordinate system ξ, η, ζ that is defined by element geometry, the isoparametric element equations are formulated. In other words, ξ, η, ζ are attached to the solid element to describe the length of the element along the axial coordinate. For each element of a specific structure, there is a relationship between the natural coordinate system ξ, η, ζ and the global coordinate system x, y, z , which must be used in the element equation formulations [97]. The reason for choosing these particular limits is to simplify the Gaussian quadrature formula for the hexahedron elements.

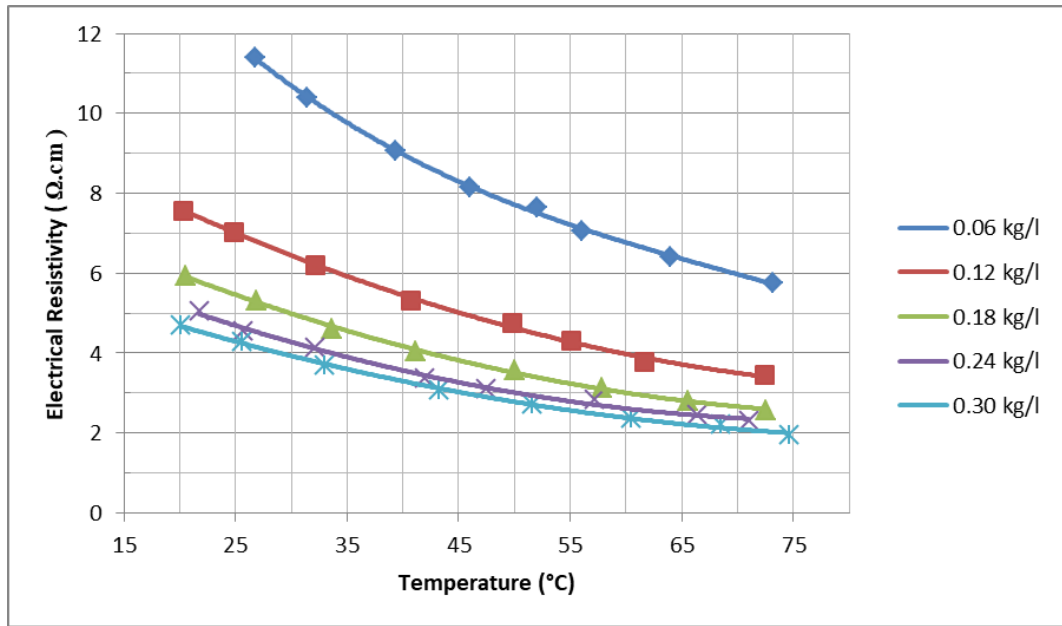


Figure 3.5 Effect of the temperature on the electrical resistivity of the *NaCl* electrolyte for different concentrations [27]

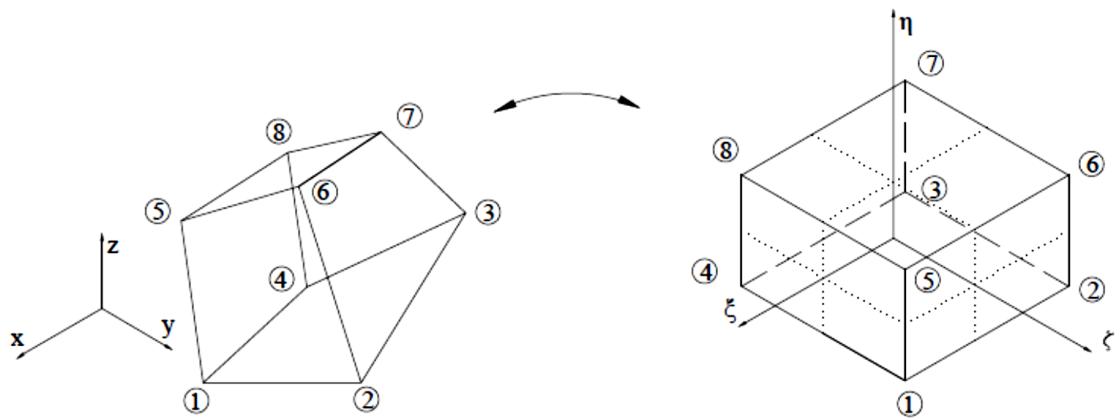


Figure 3.6 Hexahedron with eight nodes and the mapped cube.

The type of FEM is chosen as a hexahedron element having six faces and eight nodes. Figure 3.6 shows the mapped cube of a hexahedron element. In Figure 3.6, ξ goes from face 3267 to face 4158, ζ goes from face 4378 to face 1265 and η goes from face 1234 to face 5678. The intersection of the two medians is the centre of a face. Node coordinates in the natural coordinate system change between -1 and 1, as usual. According to these data, the shape functions of this element can be explained in Eq. 3.21.

$$N_i = \frac{1}{8}(1 + \xi \xi_i)(1 + \eta \eta_i)(1 + \zeta \zeta_i) \quad (3.21)$$

where ξ_i , η_i and ζ_i denote the coordinates of the i^{th} node in natural coordinates. The element stiffness matrix in Eq. 3.22 can be written as follows:

$$K[e] = \int_{-1}^1 \int_{-1}^1 \int_{-1}^1 B^e \cdot B^{eT} \cdot \det[J] \, dV \quad (3.22)$$

Where e is the element number and $\det[J]$ is the determinant of the Jacobian matrix, which describes the relation between the length of an element in the global coordinate system to the length of an element in the natural coordinate system. In general, $[J]$ is a function of ξ , η and ζ and depends on the numerical values of the nodal coordinates [98]. According to the polynomial completeness theory, a Jacobian matrix can be shown as follows:

$$J = \begin{bmatrix} \frac{\partial X_e}{\partial \xi} & \frac{\partial Y_e}{\partial \xi} & \frac{\partial Z_e}{\partial \xi} \\ \frac{\partial X_e}{\partial \eta} & \frac{\partial Y_e}{\partial \eta} & \frac{\partial Z_e}{\partial \eta} \\ \frac{\partial X_e}{\partial \zeta} & \frac{\partial Y_e}{\partial \zeta} & \frac{\partial Z_e}{\partial \zeta} \end{bmatrix} \quad (3.23)$$

where e is the element number and X_e, Y_e and Z_e are the transformation functions for mapping the hexahedron element from the local coordinate system to the natural coordinate system. B^e is the matrix that includes a derivative of shape functions; for one degree of freedom, it can be written as:

$$B^e = \begin{bmatrix} \frac{\partial N_1^e}{\partial x} & \dots & \dots & \dots & \frac{\partial N_8^e}{\partial x} \\ \frac{\partial N_1^e}{\partial y} & \dots & \ddots & \dots & \frac{\partial N_8^e}{\partial y} \\ \frac{\partial N_1^e}{\partial z} & \dots & \dots & \dots & \frac{\partial N_8^e}{\partial z} \end{bmatrix} \quad (3.24)$$

where $\frac{\partial N_1^e}{\partial x}$, $\frac{\partial N_1^e}{\partial y}$, and $\frac{\partial N_1^e}{\partial z}$ are the derivatives of shape functions. They can be obtained using the inverse of the Jacobian matrix for each element as follows:

$$\begin{bmatrix} \frac{\partial N_i^e}{\partial x} \\ \frac{\partial N_i^e}{\partial y} \\ \frac{\partial N_i^e}{\partial z} \end{bmatrix} = J^{-1} \begin{bmatrix} \frac{\partial N_i^e}{\partial \xi} \\ \frac{\partial N_i^e}{\partial \eta} \\ \frac{\partial N_i^e}{\partial \zeta} \end{bmatrix} \quad (3.25)$$

The global stiffness matrix can be obtained by assembling all element stiffness matrices. The correlation between the potential and global stiffness matrix is shown as follows:

$$\begin{bmatrix} k_{11} & k_{21} & 0 & \dots & 0 \\ k_{12} & k_{22} & \dots & \dots & \dots \\ 0 & \dots & \dots & \dots & \dots \\ \dots & \dots & \dots & k_{t-1,t-1} & k_{t-1,t} \\ 0 & \dots & \dots & k_{t,t-1} & k_{t,t} \end{bmatrix} \cdot \begin{bmatrix} \varphi_1 \\ \varphi_2 \\ \dots \\ \dots \\ \varphi_t \end{bmatrix} = \begin{bmatrix} C \\ 0 \\ \dots \\ \dots \\ 0 \end{bmatrix} \quad (3.26)$$

where t is the layer number, k is the symmetric stiffness matrix and φ_1 and φ_t are the electric potentials on anode and cathode surfaces respectively. $\varphi_2 - \varphi_{t-1}$ are the electric potentials at layers that are divided in the gap domain. C is the column vector and is shown as follows:

$$C = \begin{bmatrix} c_1 \\ c_2 \\ c_3 \\ \dots \\ c_m \end{bmatrix} \quad (3.27)$$

where m is the node number at the anode surface and c_m is the surface area integration of Eq. 3.15. It can be written as:

$$c_m = \frac{\partial \varphi}{\partial n} \cdot S \quad (3.28)$$

where “ S ” describes the surface area of a hexahedron element. For a freeform surface, it can be calculated as follows:

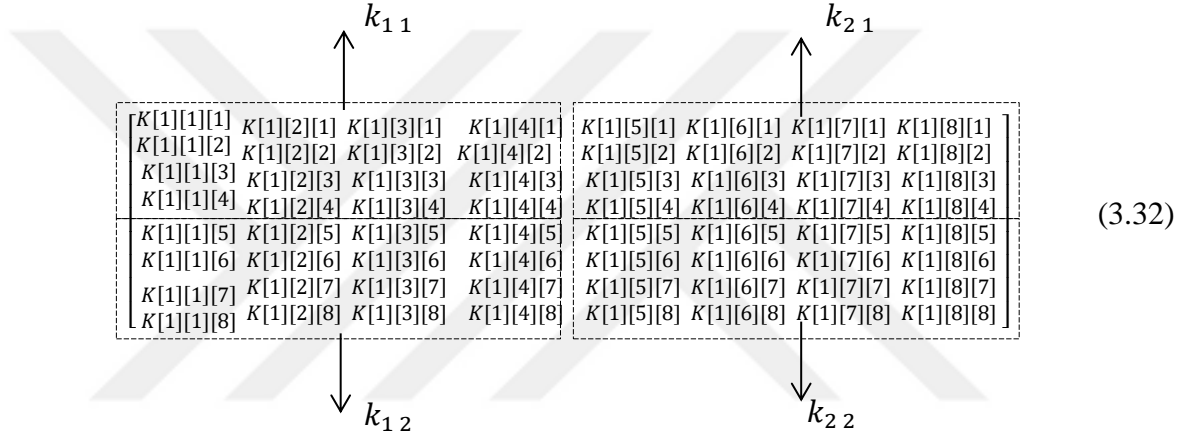
$$S = \int_{s_u} \int_{s_v} |S_u(u, v) \times S_v(u, v)| du dv \quad (3.29)$$

where s_u and s_v are the boundaries for an element along the u and v directions. According to the conditions that are discussed above, Eq. 3.26 can be solved as follows:

$$\varphi_2 = -k_{12}^{-1} \cdot (k_{11} \cdot \varphi_1 - C) \quad (3.30)$$

$$\varphi_{i+1} = -k_{i+1}^{-1} \cdot (k_{i-1} \cdot \varphi_{i-1} + k_{ii} \cdot \varphi_i) \quad 1 < i < t \quad (3.31)$$

where k_{ij} is the matrix component of the global stiffness matrix for each layer and i and j are the layer numbers. For one element and one layer, k_{11} , k_{21} , k_{12} and k_{22} are shown in Eq. 3.32. The potential distribution inside the gap domain can be obtained from Eqs. 3.30 and 3.31.



$$\begin{bmatrix} K[1][1][1] & K[1][2][1] & K[1][3][1] & K[1][4][1] & K[1][5][1] & K[1][6][1] & K[1][7][1] & K[1][8][1] \\ K[1][1][2] & K[1][2][2] & K[1][3][2] & K[1][4][2] & K[1][5][2] & K[1][6][2] & K[1][7][2] & K[1][8][2] \\ K[1][1][3] & K[1][2][3] & K[1][3][3] & K[1][4][3] & K[1][5][3] & K[1][6][3] & K[1][7][3] & K[1][8][3] \\ K[1][1][4] & K[1][2][4] & K[1][3][4] & K[1][4][4] & K[1][5][4] & K[1][6][4] & K[1][7][4] & K[1][8][4] \\ K[1][1][5] & K[1][2][5] & K[1][3][5] & K[1][4][5] & K[1][5][5] & K[1][6][5] & K[1][7][5] & K[1][8][5] \\ K[1][1][6] & K[1][2][6] & K[1][3][6] & K[1][4][6] & K[1][5][6] & K[1][6][6] & K[1][7][6] & K[1][8][6] \\ K[1][1][7] & K[1][2][7] & K[1][3][7] & K[1][4][7] & K[1][5][7] & K[1][6][7] & K[1][7][7] & K[1][8][7] \\ K[1][1][8] & K[1][2][8] & K[1][3][8] & K[1][4][8] & K[1][5][8] & K[1][6][8] & K[1][7][8] & K[1][8][8] \end{bmatrix} \quad (3.32)$$

As can be seen from Eq. 3.32, the stiffness matrix components are written as a 3D array because it is easy to understand, to search and sort the elements and to type the algorithm. The first dimension of K describes the element number, the second dimension is the column and the third dimension is the row of the stiffness matrix. Flow chart of cathode design and Mathematica codes are tabulated in Appendix A and Appendix B respectively.

3.5 Case Study

In this section, the developed mathematical model is implemented for a simple freeform surface to create a corresponding cathode surface. The anode surface shown in Figure 3.7 was modelled using the control points of the freeform surface. In order to obtain FEM results, the points on the surface were obtained using 3D surface modelling software Rhinoceros (provided by McNeel Europe in Barcelona). Mesh quality plays a significant role achieving accuracy and stability for the numerical computation. In this

study, the aspect ratio and skewness of the elements are chosen to check the mesh quality. Skewness can be defined as follows:

$$Max\left[\frac{\gamma_{max} - \gamma_e}{180 - \gamma_e}, \frac{\gamma_e - \gamma_{min}}{180 - \gamma_e}\right] \quad (3.33)$$

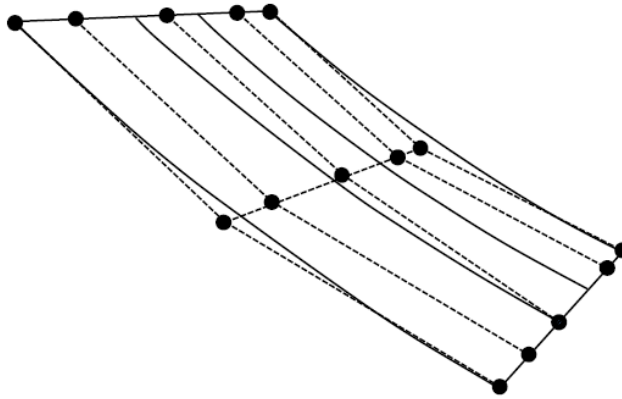


Figure 3.7 Sample freeform surface

where γ_{max} is the largest angle in the cell, γ_{min} is the smallest angle in the cell and γ_e is the angle for an equiangular cell (90° for a hexahedron element). Table 3.1 provides the cell quality and the corresponding range of skewness values. The range of skewness values for this work is $0.0108 < \gamma < 0.012$.

The other main factor that affects the mesh quality is the aspect ratio. An element's aspect ratio is the ratio of its maximum to its minimum width. To obtain good numerical results, the aspect ratio must be close to 1. The aspect ratio range of this study is $1.00013 \leq AR \leq 1.032$. Given these rules, the anode surface and the mesh points are shown in Figure 3.8.

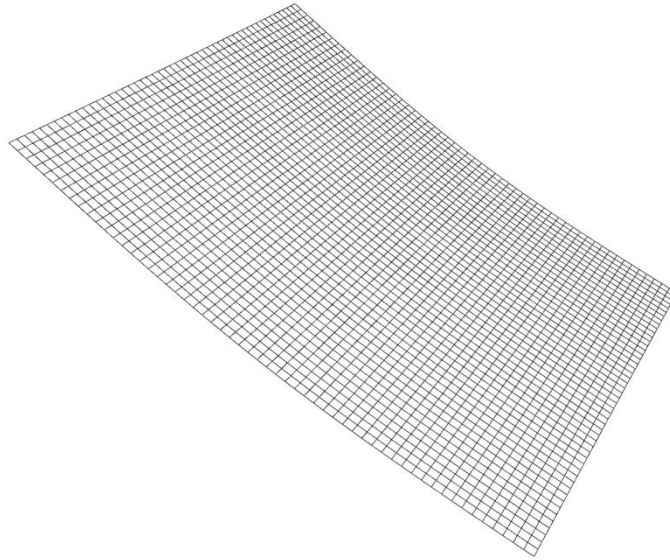


Figure 3.8 Free-form surface with mesh points

The anode surface mesh points that have good mesh quality are imported from 3D modelling software Rhinoceros to Mathematica. With the help of the mesh points, surface knot vectors along the u and v directions, B-spline basis functions, the NURBS surface model $S(u, v)$ are obtained and normal vectors of all points are calculated via $S(u, v)$.

Table 3.1 Skewness values for mesh quality

Value of Skewness	Excellent	Good	Acceptable	Poor	Sliver	Degenerate
Mesh Quality	0–0.25	0.25–0.50	0.50–0.80	0.80–0.95	0.95–0.99	0.99–1.00

In order to obtain the cathode geometry with the boundary conditions in Eqs. 3.14, 3.15 and 3.16, the mathematical model is obtained. The FEM parameters and ECM parameters are shown in Table 3.2 and Table 3.3. According to the boundary conditions of this model, the potential of the cathode surface must be 0. Due to this, the potential distribution must be obtained for all layers. In this study, fifty layers are used.

Table 3.2 ECM process parameters

Electrolyte Type	Electrical Conductivity (k) (mS/cm)	Electrochemical Machinability (k_v) ($\frac{mm^3}{100A.min}$)	Scalar Potential On Anode (U) (V)	Feed rate (V_f) (mm/min)	Equilibrium Gap (mm)
NaNO ₃	0.025	8	15	1	5

After obtaining the layer points that are discussed above, the transformational calculations (from a global coordinate system to a natural coordinate system) and assembly of the global stiffness matrix are carried out by the developed program. The program can be used for all surface types. For this example, the cathode surface that satisfies the boundary conditions is the 45th layer and the potential distribution is shown in Table 3.4.

Table 3.3 FEM parameters for the freeform surface

Number of Layer	Element Type	Number of Nodes	Number of Elements
50	Hexahedron	262500	157500

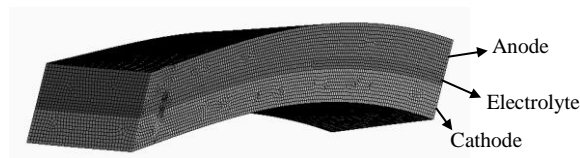


Figure 3.9 Finite element model of anode, cathode and electrolyte developed in ANSYS (Model 01)

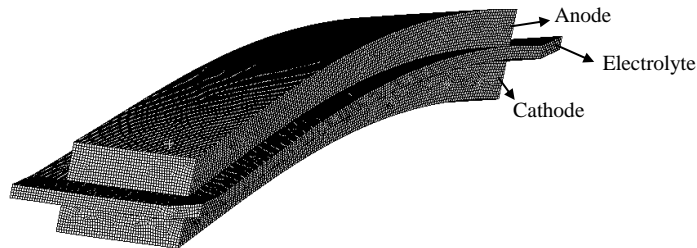


Figure 3.10 Finite element model of anode, cathode and extended electrolyte developed in ANSYS (Model 02)

Table 3.4 Potential distribution inside the gap domain

Layer Number	Point Number									
	1	2	3	4	5	6	7	8	9	10
1 st layer	0	0	0	0	0	0	0	0	0	0
2 nd layer	-0.299	-0.299	-0.299	-0.299	-0.299	-0.299	-0.299	-0.3	-0.3	-0.3
3 rd layer	-0.598	-0.598	-0.599	-0.599	-0.599	-0.599	-0.6	-0.6	-0.6	-0.6
4 th layer	-0.899	-0.899	-0.899	-0.9	-0.9	-0.9	-0.9	-0.9	-0.9	-0.9
5 th layer	-1.199	-1.199	-1.2	-1.2	-1.2	-1.2	-1.2	-1.2	13785	-1.2
....
45 th layer	-15.44	-15.24	-15.40	-15.38	-15.34	-15.25	-15.29	-15.04	-15.15	-14.87
46 th layer	-15.98	-15.76	-15.93	-15.91	-15.87	-15.76	-15.82	-15.52	-15.66	-15.34
47 th layer	-16.54	-16.29	-16.48	-16.46	-16.42	-16.29	-16.36	-16.03	-16.18	-15.82
48 th layer	-17.12	-16.85	-17.06	-17.04	-16.99	-16.84	-16.93	-16.55	-16.73	-16.32
49 th layer	-17.74	-17.44	-17.67	-17.64	-17.59	-17.42	-17.53	-17.10	-17.31	-16.85
50 th layer	-18.39	-18.06	-18.32	-18.28	-18.22	-18.03	-18.17	-17.68	-17.92	-17.40

In order to compare the results of this study with literature data, the model developed by Li and Diu [99] is improved by adding anode and cathode layers in ANSYS Workbench14.5, as shown in Figure 3.9. During the ECM process, the electrolyte flows between the anode and the cathode. Therefore, electrolyte geometry does not fit perfectly to the geometry of the anode and the cathode. To investigate the effect of geometric idealisation, a second finite element model is developed by extending the electrolyte, as shown in Figure 3.10.

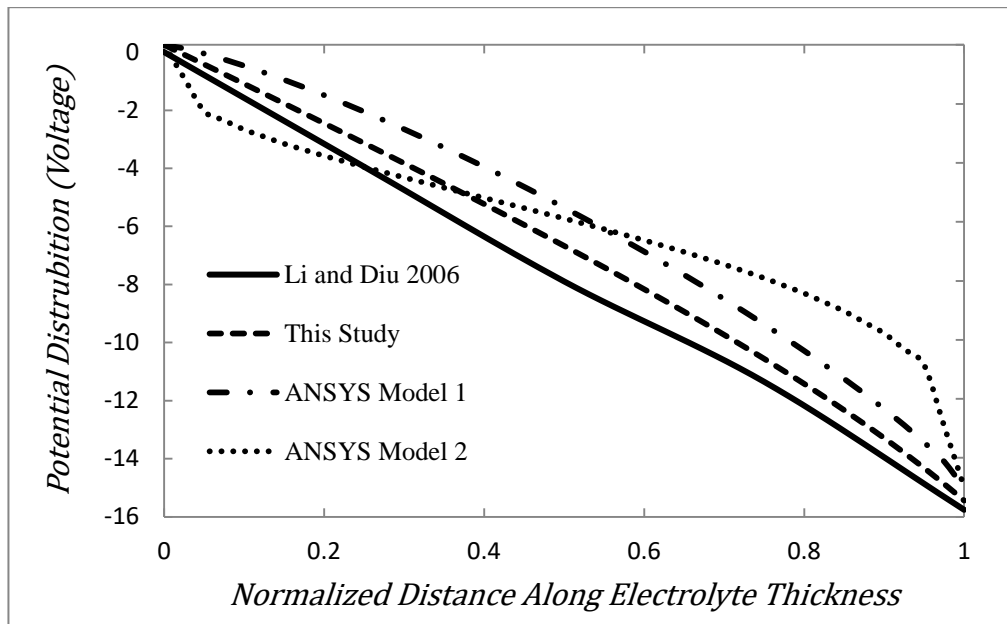


Figure 3.11 Potential distribution along the electrolyte thickness

The analysis type is set as Electric and more than 400,000 hexahedral solid elements are used in both models. The distribution of voltage potential along the electrolyte thickness in the normal direction is compared in Figure 3.11. It is shown that the linearity in potential distribution is changed when the finite element model is used with an extended electrolyte. Therefore, an extended model can provide a more realistic cathode design.

CHAPTER 4

ELECTROCHEMICAL MACHINE DESIGN AND CONSTRUCTION

4.1 Introduction

In this chapter, the development of a desktop size EC machine is presented for micro/macro manufacturing. The process experiments were conducted and discussed in order to verify the capabilities of the developed machine. With this EC machine, ECM parameters such as electrolyte flow rate, temperature, concentration, voltage, current, short circuit, feed rate and initial gap can be controlled. The experimental results were compared with the literature, which revealed that the voltage is the most effective ECM parameter.

4.2 Electrochemical Machine Setup

A multifunctional ECM machine was developed independently, as shown in Figure 4.1. This machine comprised three main units: machine base, power supply and electrolyte control units.

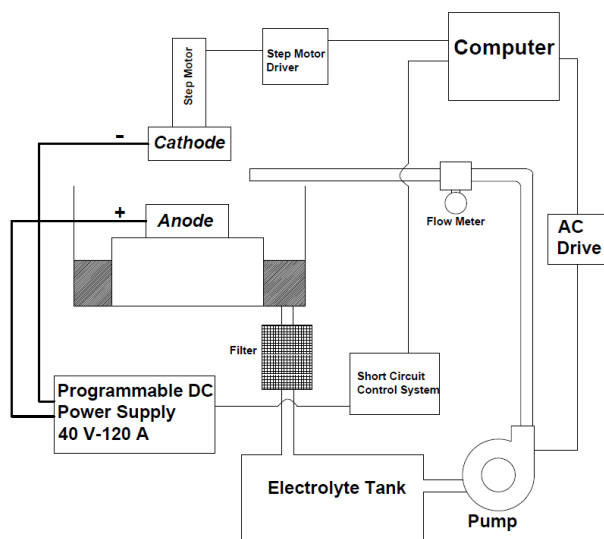


Figure 4.1 Schematic of electrochemical (EC) machine



Figure 4.2 Photograph of the electrochemical machine

4.2.1 EC Machine Base

The machine base of the ECM was provided by a manufacturer (Dogus Kalip, İstanbul). and they were constructed using aluminium sigma profiles in order to avoid corrosive effects of the electrolyte. A triple-axis electrode feed mechanism was used with G-codes in this multifunctional machine tool. The moving parts of the X, Y and Z axes were driven by stepper motors through precision ball-race feed screw with a resolution of 25 μm . The tool electrode or cathode was clamped onto the Z-axis by a Plexiglas plate. The ECM machine's base specifications are shown in Table 4.1.

Table 4.1 Specifications of the EC machine base

Working area (mm)	350	350	100
X-Y-Z movements (guideways)	Recirculating rolling guides		
Max. movement speed (m/min)	4		
Max. machining speed (m/min)	2		
Motor type	Stepper		
Motion transmission	16/5 ball screw		
Table	22.5 mm T-channel aluminium		
Structure	Aluminium		

Advantages such as precise positioning and good response to starting, stopping and reversing stepper motors were chosen for the ECM machine. As discussed below, the accuracy of a cathode's movement is a key factor in ECM. Due to advantages such as higher load capacity and high-accuracy square type, recirculating rolling guides were chosen [100]. The drive-by ball screw is the most widespread in the machine tool field for strokes not exceeding 4–5 m (a ball screw is a mechanical device which transforms the rotary movement into linear movement [100]). It is the preferred device largely due to the high mechanical reduction provided while maintaining high efficiency and stiffness, as well as sufficient accuracy for existing machine tools. In this study, linear drive was controlled by a ball screw.

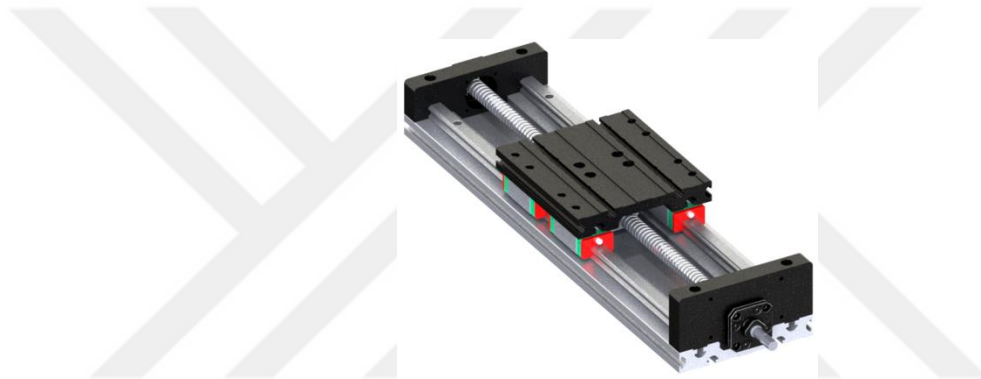


Figure 4.3 Linear motion system

Communication between the machine and the computer was achieved with a parallel port connection. This is a very simple way of transferring data and has been used for many things other than connecting printers. It can transfer files between PCs, attach copy protection dongles, connect peripherals such as scanners and zip drives, and of course, control the machine tools using it. The USB interface controls many of these functions, which conveniently leaves the parallel port free for the ECM control board.

Limit switches were used to prevent any linear axis from moving too far and causing damage to the structure of the machine. The machine can be operated without them, but the slightest mistake in setting up or programming can cause a good deal of expensive damage. Cylindrical photoelectric sensors were also used in this machine as limit switches.

Stepper motors have input pins or contacts that allow current from a supply source (in this case, a microcontroller) into the motor's coil windings. Pulsed waveforms in the

correct pattern can be used to create the electromagnetic fields needed to drive the motor. Depending on the design and characteristics of the stepper motor and the required motor performance, some waveforms work better than others. There are several options to choose from when selecting a waveform to drive a two-phase PM stepper motor, such as full-stepping or micro-stepping. These signals can be produced by a dedicated stepper driver. A schematic of the ECM machine axes' control mechanism is shown in Figure 4.4 and a picture of the electrical cabinet of the ECM machine is shown in Figure 4.5.

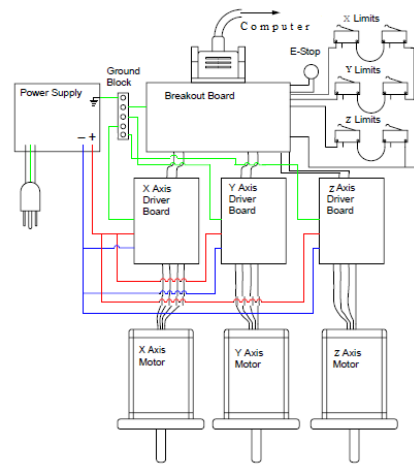


Figure 4.4 Schematic of the EC machine stepper motor control system

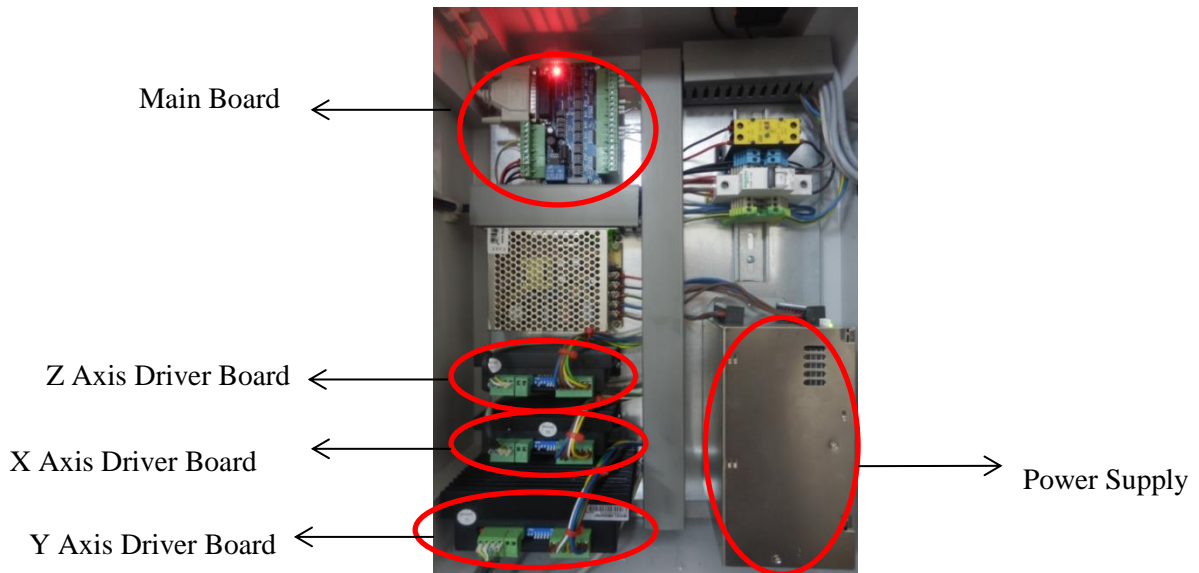


Figure 4.5 Electrical cabinet of the EC machine

A machining cell was designed to machine workpieces having different shapes. The machining cell was collapsible and made of Plexiglass as not to affect the corrosive electrolyte on the EC machine construction and to place the workpiece on the working

area. The machining cell had four holes: three electrolyte inlets delivering the fresh electrolyte to the working area and one electrolyte outlet taking the used electrolyte to the filtering station.



Figure 4.6 Machining cell

4.2.2 Direct Current (DC) Power Supply

One of the main units in the ECM was the DC power supply. The DC power supply had to be powerful enough to supply the necessary machining current to the working gap. According to the laws of electrolysis, ECM occurs at low voltage and high current values. In addition, control of the voltage and current with precision are important factors in ECM. The EC machine was equipped with a programmable DC power supply, the power capacity of which is 2400W, to achieve the requirements discussed above. The maximum range of the DC power supply was 40 V – 60 A for voltage and 20 V – 120 A for current. In addition, the DC power supply enabled reading the voltage and current outputs to avoid short circuits by control cards such as Programmable Logic Controller (PLC) or microprocessors. Table 4.2 provides the specifications of the DC power supply that was used for the EC machine.

Table 4.2 Specifications of the DC power supply

Output Voltage	0 – 40 V
-----------------------	----------

Output Current	0 – 120 A
Output Power	1200 – 2400 W
Voltage Measurement	
Range	8 – 40 V
Accuracy	% 0.05 + % 0.05 F.S.
Current Measurement	
Range	24 – 120 A
Accuracy	% 0.1 + % 0.1 F.S.

4.2.3 Electrolyte Control Unit

Electrolyte properties such as concentration, flow rate and temperature are also important for ECM. For this reason, the electrolyte pump has special importance. Due to certain advantages such as its smooth run and low cost, the electrolyte pump chosen was a tri-phase type. Its specifications are shown in Figure 4.7. As can be seen from Figure 4.7, the capacity of the pump or flow rate changed with the head and the power of the pump. The head of the pump cannot be changed due to the design of the ECM system therefore the power of the pump had to be controlled to change the capacity of the pump. In this system, a low-voltage AC drive was used to control the flow rate or the capacity of the pump.

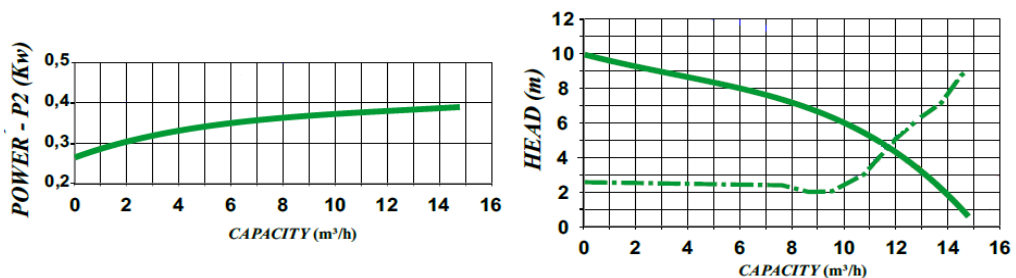


Figure 4.7 Specifications of the pump

An AC drive is a device used to control the speed of an electrical motor in an energy-efficient way. By using the AC drive, electrolyte flow rate can be adjusted from 0.1 to 14 m³/h. The AC drive was controlled by a device that was connected to a flow meter. Given the electrolyte pump power, the ACS310 type AC drive was chosen. Its specifications are provided in Table 4.3. To verify the flow rate of the electrolyte, a

turbine-type flow meter was mounted on the plumbing system; to meet the maximum flow rate capacity of the pump, a flow meter with a diameter of 32 mm was chosen.

Table 4.3 Specifications of the AC drive

Phase type	P_N (kW)	P_N (hp)	R_{max} (Ohm)
Three	0.55	0.75	390

4.3 Case Study: Electrochemical Drilling

The experimental observations and research studies were designed in such a way as to enable fruitful analysis for deriving the effective research findings, which can be useful for applied researchers and manufacturing industries in the field of hole drilling achieved through ECM. To analyse the control of the required performance characteristics of the ECM system's process parameters, the scheme was designed to properly utilise the developed EC machine. The tools, comprising brass of 3 mm diameter and workpiece specimens, were maskless copper plates that measured 40 mm×40 mm×5 mm. The tool and the workpiece are shown in Figure 4.8. A fresh aqueous solution of sodium nitrate ($NaNO_3$) was typically chosen as an electrolyte for experiments, along with a variable pulsed DC power supply.



Figure 4.8 Brass tool and the copper workpiece

The variation of MRR and the overcut were observed with the variation of predominant electrochemical process parameters. Machining voltage, feed rate and initial gap are considered to be more influential parameters in ECM. These parameters were considered for the experiments, to study their influences on machining criteria such as MRR and overcut.

Table 4.4 shows the ECM parameters used in the operation, where V_f is the feed rate of the tool (mm/min), Δb is the initial gap (mm) and V is the voltage (V).

Table 4.4 Experimental conditions

Experiment Condition	Δb (mm)	V_f (mm/min)	V (Voltage)
1	0.3	3	5
2	0.3	3	8
3	0.3	3	10
4	0.5	3	5
5	0.5	3	8
6	0.5	3	10
7	0.7	3	5
8	0.7	3	8
9	0.7	3	10
10	0.3	5	5
11	0.3	5	8
12	0.3	5	10
13	0.5	5	5
14	0.5	5	8
15	0.5	5	10
16	0.7	5	5
17	0.7	5	8
18	0.7	5	10

Eq. 4.1 was used to calculate the material removal rate (MRR), considering a workpiece density of $0.00896g/mm^3$:

$$MRR = \frac{m_{uw} - m_{mw}}{\rho_w \cdot t_m} \quad (4.1)$$

where m_{uw} is the workpiece mass before machining, m_{mw} is the workpiece mass after machining, ρ_w is the workpiece's specific mass and t_m is machining time.

Eq. 4.2 was used to obtain the overcut, where D_h is the hole diameter and D_c is the cathode diameter:

$$Overcut = \frac{D_h - D_c}{2} \quad (4.2)$$

The initial and final weights of the workpiece were taken by a precision electronic weighing machine. To enable discussion of the shortcut effects on MRR , shortcut time was added to machining time and the time was noted with help of stopwatch.

4.3.1 Effect of Voltage

Figure 4.9.a shows the effect of voltage on MRR for different initial gaps. The graph indicates that an increase in voltage causes the MRR to increase for different initial gaps. The obtained results are similar to those found in the literature [51, 53].

$$I = \frac{V}{R} \quad (4.3)$$

Eq. 4.3 shows Ohm's law where I is current, V is voltage, and R is the electrical resistance of the electrode. According to this law, for a constant resistance, current is directly proportional to voltage.

$$M = k_v \cdot I \cdot t \quad (4.4)$$

According to Faraday's first law, Eq. 4.4 shows the mass amount of material removed from an electrode, where M , the mass of the substance liberated at any electrode; k_v is the electrochemical machinability of the electrode; and t is time. As a consequence of Eq. 4.3 and 4.4, the amount of removed materials is directly proportional to the voltage.

However, experiments show that the least MRR has been obtained for a 0.5 mm initial gap distance for 5 and 8 V ($V_f = 5 \text{ mm/min}$). As discussed in Eq. 4.1, MRR is attributed to machined mass and machining time. As maintained in Figure 4.9.b, overcut values are the lowest for a 0.5 mm gap distance, but the differences are too low to affect MRR . Therefore, this variation of overcut can be attributed to machining time. In this work, it was found that the most effective way to increase machining time was with

short-circuiting of the anode and cathode. This is because MRR is less for a 0.3 mm gap distance than for a 0.7 mm gap distance for all voltage values. However, the difference between MRR for a 0.3 mm gap distance and a 0.5 mm gap distance is too high for 5 V. This can be attributed to a filtering system that is inefficiently removing the contamination in the electrolyte. This will be discussed further in Chapter 6. Therefore, an increase in contamination causes an increase in short-circuiting. For 8 V, the short-circuiting effect is lower due to fresh electrolytes being applied to machining area. However, for a 0.5 mm gap distance, MRR is the lowest because the machined mass is lower than the others. As can be seen from Figure 4.9.b, the lowest overcut is obtained for the 0.5 mm gap distance for 8 V. For 10 V, short-circuiting causes the lowest MRR for a 0.3 mm gap distance. The reason for this could be that the travel time between the anode and cathode is too short, which causes a current increase immediately. Additionally, the reason for a higher MRR for a 0.5 mm gap distance can be attributed to it having a lower travel time than a 0.7 mm gap distance.

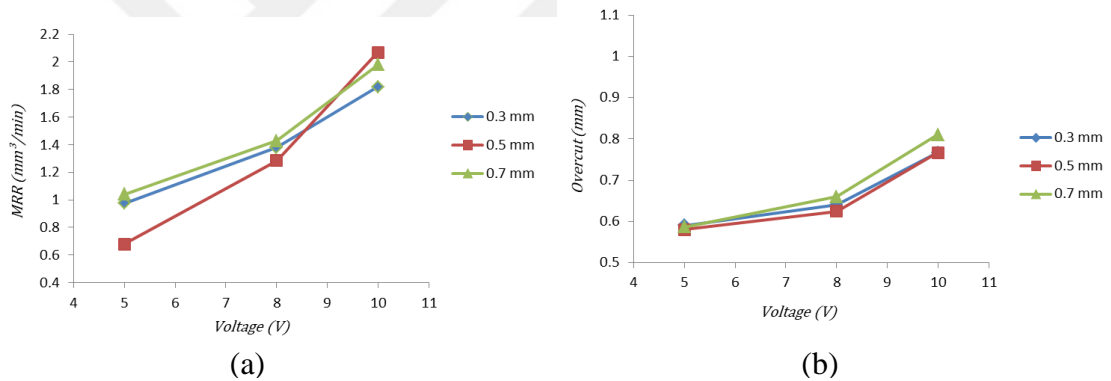


Figure 4.9 Effect of voltage on (a) MRR and (b) $Overcut$ for $V_f = 5 \text{ mm/min}$

As can be seen from Figure 4.9.b, an increase in voltage causes an increase in overcut. Due to the increase of machining voltage, the localisation effect of current flux flow decreases. With less localisation effect, the stray current flow actually increases in the machining zone, in turn affecting more material removal from the larger area of the workpiece; this causes an increase in overcut. Electrochemical reactions generate H_2 gas in the tool. At a higher voltage, H_2 gas bubbles break down; this results in the occurrence of micro-sparking. This sparking causes uncontrolled material removal from the workpiece, eventually resulting in a larger overcut. Therefore, the overcut increases more rapidly at higher voltage.

Figure 4.10.a and Figure 4.10.b show the effect of voltage on MRR and overcut for different initial gaps, for $V_f = 3 \text{ mm/min}$ respectively. As can be seen from Figure

4.10.a, an increase in voltage causes an increase in MRR that is discussed above; however, after 8 V, the increase in MRR is very low. As maintained in Figure 4.10.b, the overcut increases significantly after 8 V for all initial gaps. Therefore MRR is not associated with machined mass. This occurs because the machining time for 8 V and 10 V are approximately equal for all initial gaps. Because of the lower feed rate, the electrolyte flow in the machined hole acts as a turbulence flow. This can cause an increase in short-circuiting between the anode and cathode. Therefore, the machining time increases, which could result in a decrease in MRR after 8 V.

Overcut values for 0.7 mm gap distance is higher when compared to other initial gaps in Figure 4.9.b and Figure 4.10.b. This can be attributed the higher distance can cause bigger H_2 gas bubbles with increased voltage.

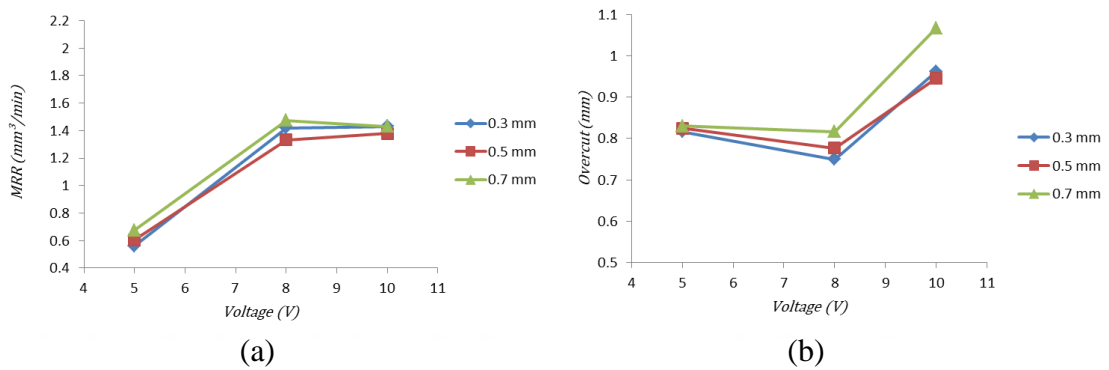


Figure 4.10 Effect of voltage on (a) MRR and (b) $Overcut$ for $V_f = 3 \text{ mm/min}$

4.3.2 Effect of Feed Rate

Figure 4.11 shows the effect of feed rate on MRR . As can be seen from Figure 4.11, MRR increases with feed rate. This result, which is qualitatively similar to the literature [98], indicates an increase in feed rate causes a decrease of the gap size between the anode and cathode, in turn causing a decrease of resistance between the anode and cathode; therefore, machining time is reduced and MRR is increased. For $V_f = 3 \text{ mm/min}$ and a 0.3 mm gap distance, the travel time is 6 s. However, this time decreased to 3.6 s for $V_f = 5 \text{ mm/min}$. The decrease in travel time resulted in too short of a time to remove material from the anode surface. Due to non-machined surfaces, the instances of short-circuiting increase with higher feed rates and lower gap distances. Therefore, MRR for a 0.3 mm gap distance is the lowest at $V_f = 5 \text{ mm/min}$. In this context, it was assumed that the short-circuit effect on MRR reduces after a 0.3 mm gap

distance. Additionally, the highest *MRR* has been obtained for a 0.5 mm gap distance, which can be attributed to less machined mass.

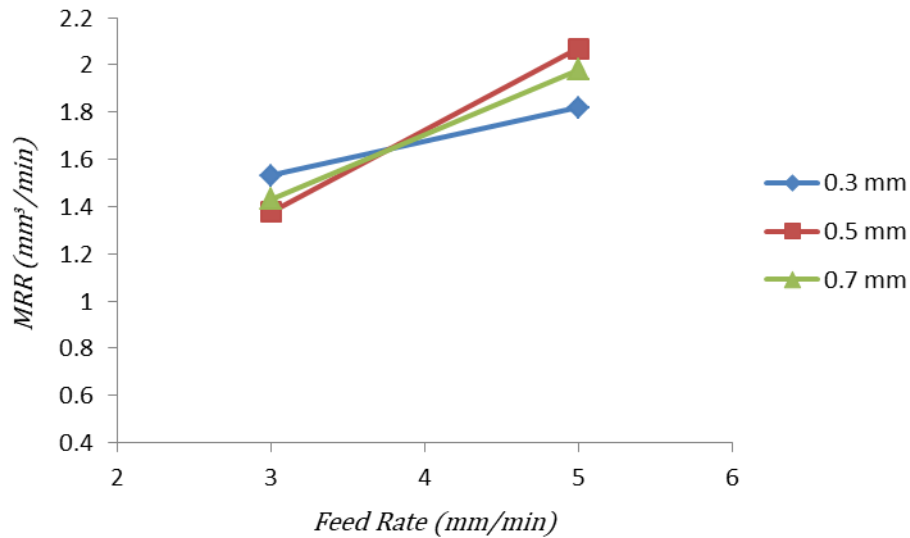


Figure 4.11 Effect of feed rate on *MRR* for 10 V

The relationship of overcut at different feed rates is shown in Figure 4.12. Figure 4.12 shows that an increase in tool feed rate reduces the overcut. With an increase in tool feed rate, the void fraction increases and the electrolyte conductivity decreases, resulting in a reduction in the overcut. The accumulation of gas bubbles on the side surface of the cathode and the precipitation of the metal ions removed from the workpiece on the side-wall of the hole (or anode) together reduce the passage of current in the radial direction; this, in turn, reduces side dissolution of the work material.

For lower feed rates, transferring electrolytes increases through the machining area; thus, electron transfer increases with electrolyte flow. Therefore, the overcut that is shown in Figure 4.12 is higher than the overcut at higher feed rates.

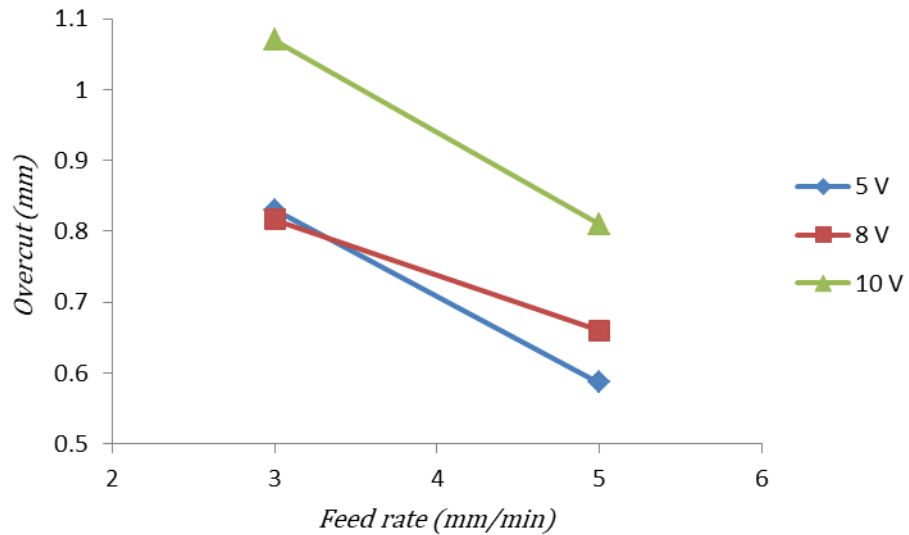


Figure 4.12 Effect of feed rate on *Overcut* for 0.5 mm initial gap

4.3.3 Effect of Initial Gap

The relationship of *MRR* to various initial gap distances is shown in Figure 4.13. Figure 4.13 shows that the effect of initial gap on *MRR* is very low. In addition, 8 V and 10 V *MRR* show similar variation for a 0.3 mm gap distance. *MRR* variation is too low for 0.5 and 0.7 mm gap distances. In this study, electrolyte transition was made outside the machining area. Changing the transition type to flushing inside the cathode can increase the effect of the initial gap on the *MRR* and overcut. Thus, for every gap distance, electrolytes can be transferred to the gap domain in different flow rates.

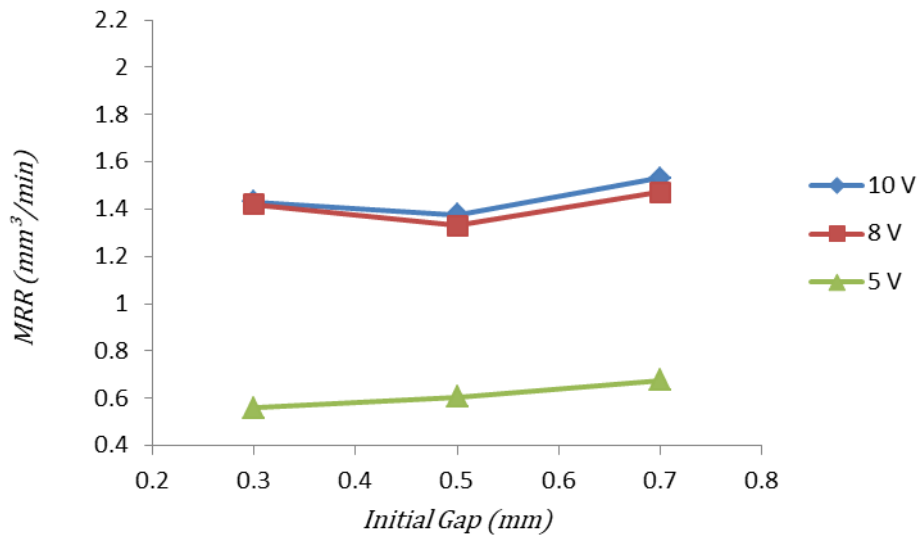


Figure 4.13 Effect of initial gap on *MRR* for $V_f = 3 \text{ mm/min}$

Figure 4.14.a shows that overcut does not change according to initial gap, for varying initial gaps. This is because the distance between the anode and the cathode is too long for the occurrence of the electric field. If the initial gap is reduced to less than 0.3 mm, it can be more effective for 5 V. Electric field is a vector quantity and decreases with the increasing distance. Electric field can be found by using Eq. 4.5.

$$E = \frac{V}{d} \quad (4.5)$$

where, E is the electric field of two electrodes, V is the potential difference of power supply and d is the distance of two electrodes.

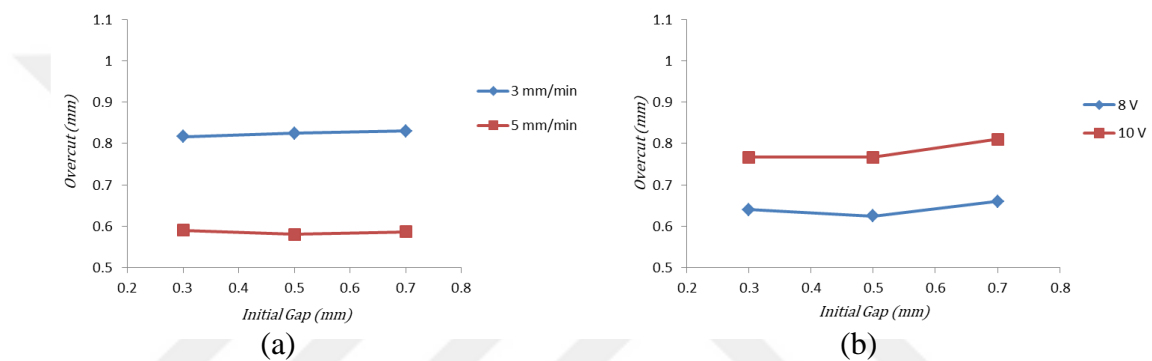


Figure 4.14 Effect of initial gap on *Overcut* for (a) 5 V and for (b) $V_f = 5$ mm/min

However, after 5 V, the influence of initial gap on overcut increases. As can be seen from Figure 4.14.b, a 5 mm/min feed rate changes with the overcut for 8 V and 10 V becomes similar; a 0.7 mm initial gap distance causes a rise in the overcut. This occurs because the time it takes to travel the initial gap distance of 0.7 mm is enough to dissolve the metal atoms.

The time required to travel the initial gap distances is also long enough to dissolve the metal atoms for lower feed rates. Figure 4.15 shows that initial gap has a significant role in the overcut and causes an increase in it.

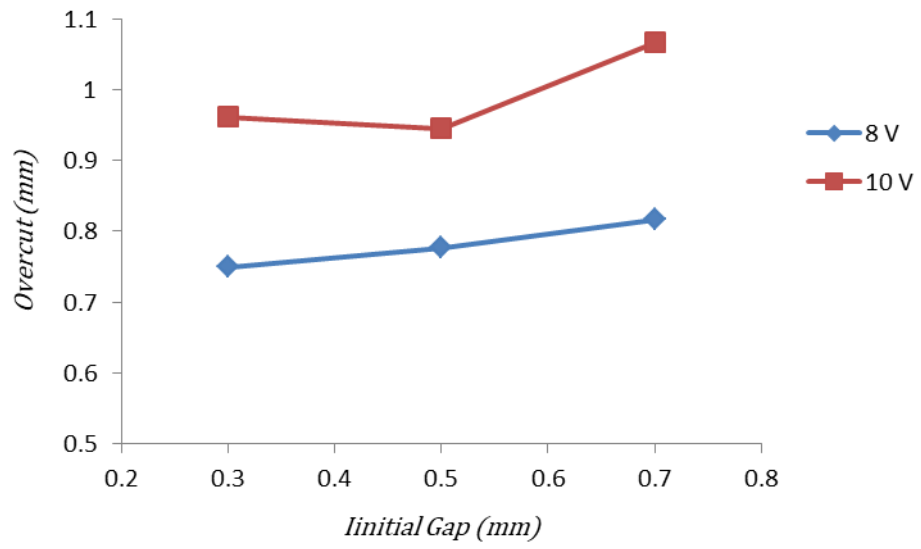


Figure 4.15 Effect of initial gap on *Overcut* for $V_f = 3$ mm/min

CHAPTER 5

EXPERIMENTAL STUDY

5.1 Introduction

This chapter describes the experimental procedure, mathematical modelling of the cathode surface, materials and methods, and quality control. Several experiments were conducted to verify the usability of the mathematical model for free-form surface machining in ECM, which is discussed in Chapter 3. Two process parameters were used for different initial gaps. These parameters are feed rate and electrolyte conductivity, which are important factors in modelling cathode surface design. Use of these parameters enables discussing the applicability of this mathematical model to free-form surface applications.

5.2 Experimental Procedure

In Section 3.2.2, due to the equation 3.15, the following factors had the greatest effect on cathode surface design: feed rate (V_f), electrochemical machinability of anode material (k_v), electrical conductivity of the electrolyte (k_c) and the angle between the movement direction of the cathode and normal to the anode control point (θ). θ and k_v are the characteristic properties of anode material and surface geometry. However, V_f and k_c are the dynamic ECM parameters that can be changed; these are discussed in detail in Chapter 2. V_f can be set by using G-coding, which is explained in Chapter 4. k_c can be adjusted, so that the salt quantity in the electrolyte composition can be increased or decreased. Because of this, different cathode designs and initial gaps are obtained for two variables by using the mathematical model. Experimental conditions are shown in Table 5.1.

Table 5.1 Experimental Conditions

Experimental Condition	Electrolyte	Feed Rate V_f (mm/min)	Initial Gap
	Conductivity k_c (S/mm)		Distance Δb (mm)
1	0.005	1	3.2
2	0.005	3	2.3
3	0.005	5	1.0
4	0.007	1	3.6
5	0.007	3	2.5
6	0.007	5	2.0
7	0.01	1	3.8
8	0.01	3	2.8
9	0.01	5	2.4

As can be seen from Table 5.1, nine different cathode surfaces have been designed and nine different initial gap distances have been obtained via the designed mathematical model. The design of cathode surfaces given these ECM parameters will be discussed in Section 5.3.

Another important parameter voltage (U) that is discussed in Section 3.4 (in Eq. 3.16) was kept constant and $U = 15 V$ for this study.

5.3 Mathematical Modelling of the Cathode Surface

The experimental observations and research studies were designed to carry out useful analysis and derive valuable findings that can be used in machining of freeform surfaces by ECM. Figure 5.1 shows a jet engine compressor blade and its suction and pressure surfaces. Each of these surfaces is an example of a freeform surface. To describe the anode surface, NURBS modelling (discussed in Section 3) is applied using Eq. 3.1.

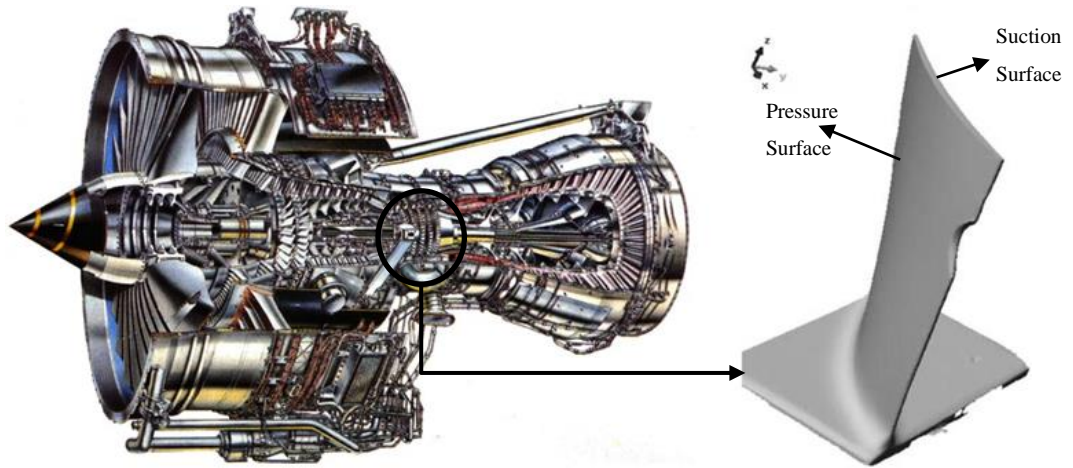


Figure 5.1 Jet engine and compressor blade with suction and pressure surfaces [102]

As can be seen in Figure 5.2.a, some control points are on the surface and others are not. Distances between control points in the u and v directions are not similar to each other. This situation causes high deviation in designing the cathode surface due to the high aspect ratio values (the effect of aspect ratio is discussed in Section 3.5). Therefore, points have been selected as control points on the surface; to achieve good aspect ratio values, the $u - v$ distances are maintained at admissible values. These control points and the CAD model are shown in Figure 5.2.b.

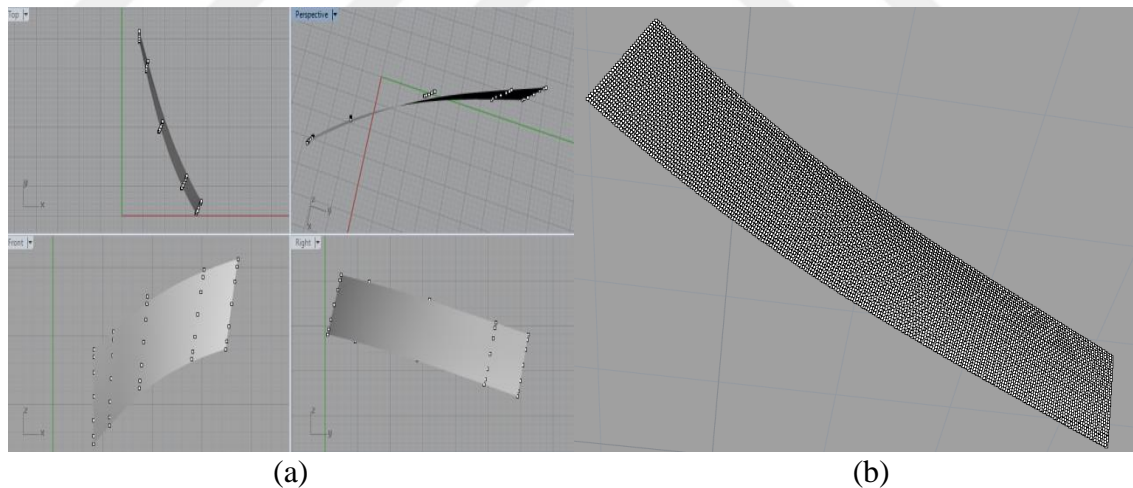


Figure 5.2 Modelled freeform surface via control points (a) on space and (b) on surface

As can be seen from Figure 5.2.(b) the number of control points in the u and v directions can be divided as required. The θ and α angles were calculated using Eqs. 3.11 and 3.12, for points that are shown in Table 5.2.

Table 5.2 Calculated θ and α angles for some points on a freeform surface

Point Number	θ	α
1	39.8032	-59.3392
25	39.3707	-59.394
155	37.4151	-58.8093
220	36.3736	-58.634
320	35.0875	-57.9868
450	32.9803	-57.7697
600	30.5638	-57.7622

A trial gap distance was chosen to determine the potential distribution within the gap domain. For all experiments, the trial gap distance was taken as 5 mm. Every gap was divided into 10 layers and an anode. The trial tool shape with layers is shown in Figure 5.3.

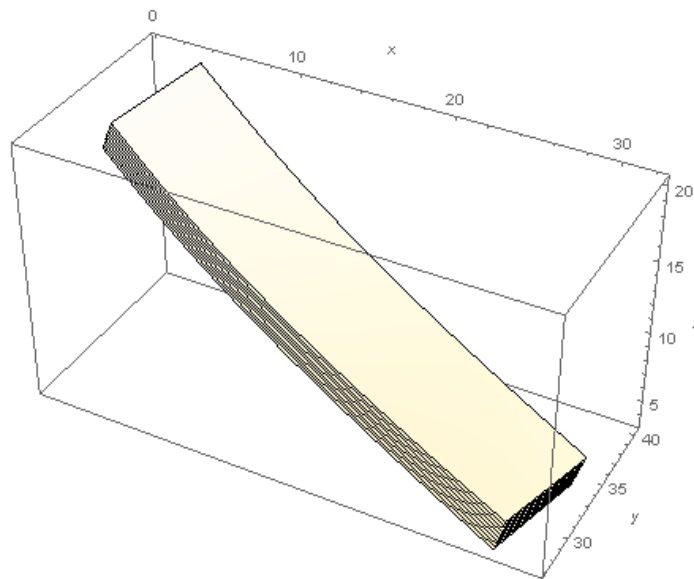


Figure 5.3 Anode and trial cathode surface with layers

After obtaining the layer points, the transformational calculations (from global coordinate system to natural coordinate system) and assembly of the global stiffness matrix were carried out by the developed program. The FEM parameters that were used for cathode design are shown in Table 5.3.

Table 5.3 FEM parameters for cathode design

Layer Number	Element Type	Number of Nodes	Number of Elements
50	Hexahedron	262500	157500

5.4 Materials and Methods

5.4.1 Electrolytes

The effects of electrolyte properties are discussed in Chapter 2. In this study, a fresh aqueous solution of *NaCl* was typically chosen as the electrolyte for the experiments. Electrolyte solution was prepared by adding different amount of *NaCl* with distilled water in the electrolyte tank. Electrolyte concentration has been calculated by using Eq. 5.1. Electrolyte properties are shown in Table 5.4.

$$\text{Electrolyte Conc. (\%)} = \frac{m_s}{m_{el.}} \cdot 100 \quad (5.1)$$

where m_s is the mass of salt and $m_{el.}$ is the mass of electrolyte and can be calculated with using Eq. 5.2.

$$m_{el.} = m_s + m_{dw} \quad (5.2)$$

where m_{dw} is the mass of distilled water that is used prepare the electrolyte.

Table 5.4 Electrolyte properties

Electrolyte Type	Temperature (°C)	Flow Rate (lt/ min)	Electrolyte Tank Capacity (lt)	Electrolyte Concentration (% <i>NaCl</i>)	Electrical Conductivity (mS/cm)
<i>NaCl</i>	~25	8	80	4.24	50
				4.54	70
				8.48	100

As can be seen from Table 5.4 the temperature of electrolyte before using in experiments was kept constant at room temperature.

5.4.2 Anode and Cathode Material

Due to advantages such as low cost, easy machinability with conventional machining processes and market availability, 1040 carbon steel was chosen as the anode material. Drawing and a photographic view of the anode are shown in Figure 5.4.a and Figure 5.4.b respectively.

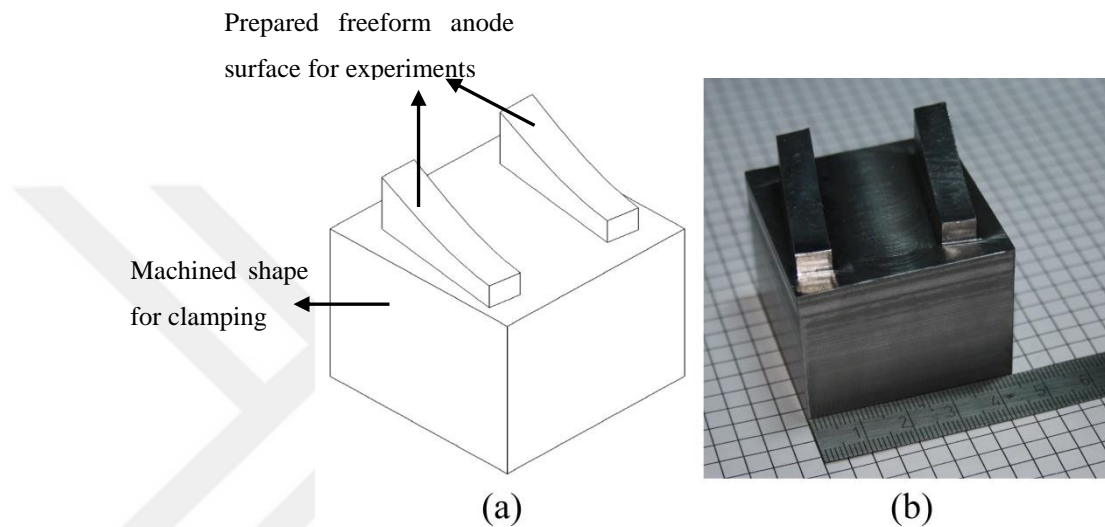


Figure 5.4 Drawing (a) and photographic view (b) of the anode

In order to investigate the effect of cathode material on ECM of freeform surfaces, three different types of metals were used in experiments. The cathode materials, chemical properties and certain mechanical properties are shown in Table 5.5.

Electrochemical machinability of the workpiece is calculated with using Eq. 2.6 and Eq. 2.7 and $k_v = 6.22 \text{ mm}^3/(\text{min. A})$ for all experiments.

Table 5.5 Chemical and mechanical properties of cathode materials

Material	Element										Tensile Strength (MPa)	Electrical Conduc. (S/mm)
	Fe	Pb	Cu	Zn	C	Si	Mn	Cr	Ni	S		
Stainless Steel	57.0	-	-	-	0.25	1.5	2.0	24.0	22.0	0.03	500-700	1,280
Copper	-	-	99.98	-	-	-	-	-	0.02	-	200-250	32,258
Brass	0.05	0.05	86	13.9	-	-	-	-	-	-	338-469	15,625

As can be seen from Table 5.5, the most conductive and easy-to-machine materials are copper, brass and stainless steel, respectively. The reasons for choosing brass and copper as cathode materials are easy machinability by conventional machining and good electrical conductivity. The reason for choosing stainless steel, which is more difficult to process than others, is that the corrosion resistance against salt water is high. Drawing and photographic view of the cathode is shown in Figure 5.5.a and Figure 5.5.b, respectively.

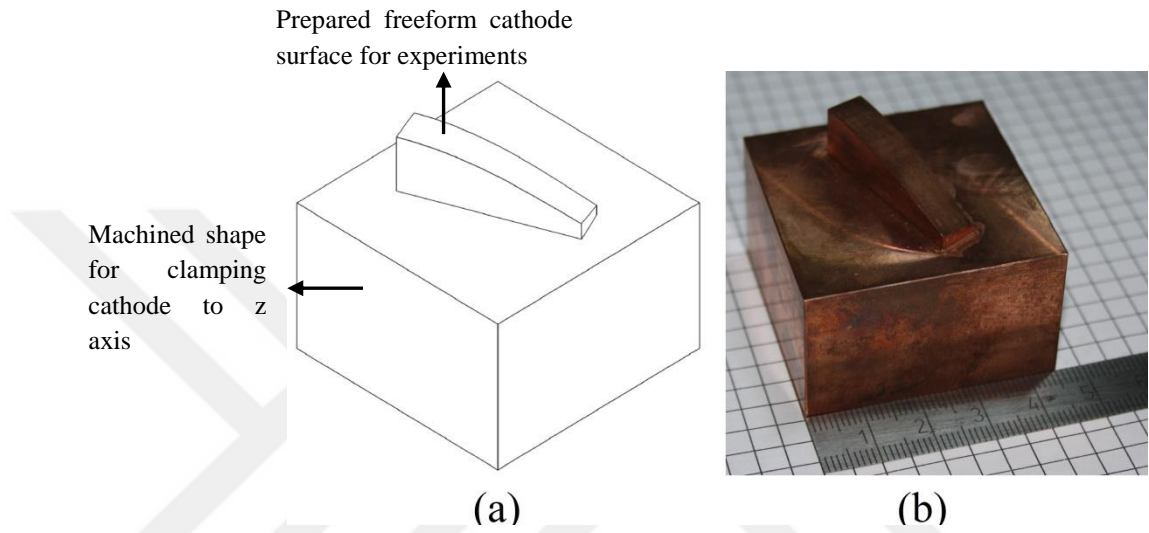


Figure 5.5 Drawing (a) and photographic view (b) of the cathode

The machining time for copper, brass and stainless steel are 15–20, 20–25 and 60–80 min, respectively. The anode and cathode are machined with a Hyundai 560/5A CNC machine. Quality control reports of the machined surfaces are shown in Figure 5.6. This report is obtained with comparing STL and CAD models of anode and cathode surfaces. STL file is created with using point cloud that are obtained by using 3D scanner.

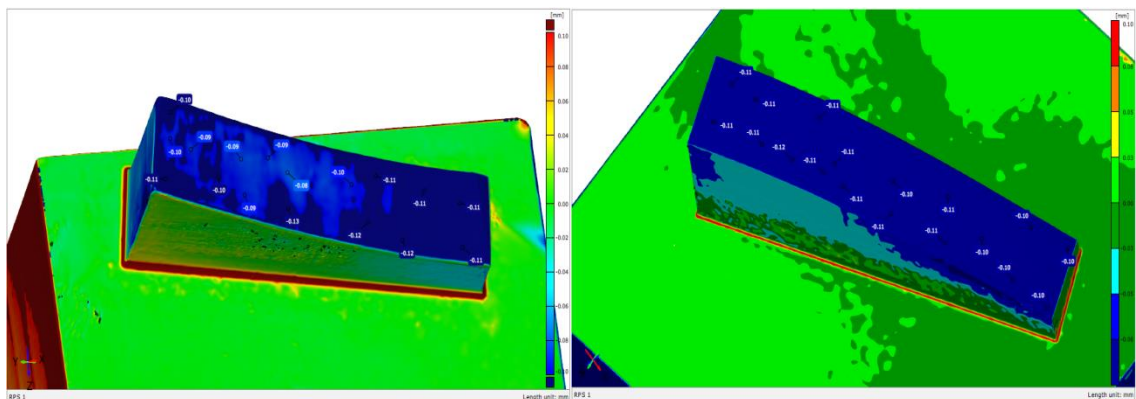


Figure 5.6 Surface measurement reports of prepared anode and cathode surfaces

5.5 Equipment and Instrumentation

The main equipment used in the experimental study is explained in this section, and measuring instruments are described.

5.5.1 EC Machine

The designed EC machine and main units (electrolyte control, DC power supply and machine base) are discussed in Chapter 4.

5.5.2 Electrical Conductivity Measurements

Electrical conductivity of the electrolyte is an important parameter in cathode design; it is discussed in Section 5.1. For every experiment, conductivity values must be controlled. Specifications of the conductivity meter are shown in Table 5.6. The Extech® EX530 true RMS multimeter is used in order to verify the current and voltage output of the DC power supply. A photographic view of the conductivity meter and multimeter is shown in Figure 5.7.a and Figure 5.7.b, respectively.

Table 5.6 Specifications of conductivity meter

Range (mS/cm)	Resolution Accuracy (mS/cm)	Calibration
0 – 199.9	0.01	5 points

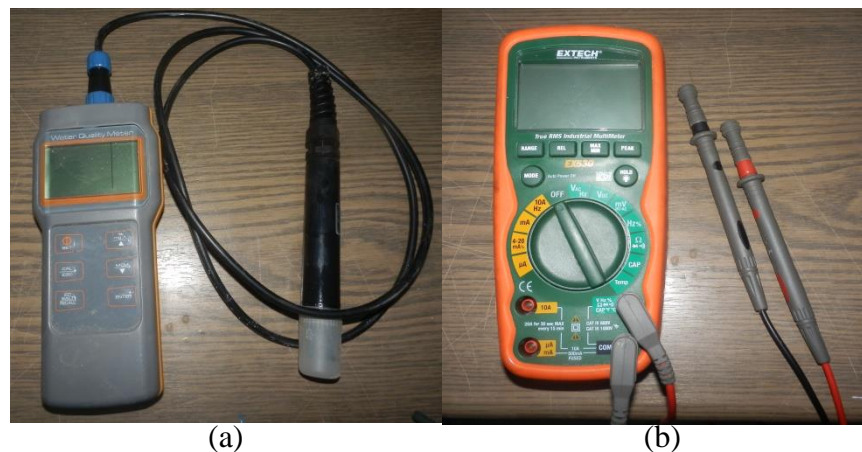


Figure 5.7 Photographic view of (a) conductivity meter and (b) multimeter

5.5.3 Material Removal Rate Measurements

Material removal is another significant output parameter in the ECM process. It is calculated as the difference between the initial and final weights of the specimen. The

Radwag PS 2100 balance, having 0.1 mg accuracy, is used in these experiments as shown in Figure 5.8.



Figure 5.8 Photographic view of Radwag balance

5.5.4 Surface Measurements

It is difficult to measure freeform surfaces with traditional measurement methods. Therefore, to measure and compare the electrochemical machined anode surfaces with the CAD model, a 3D scanner was used. With a 3D scanning operation, a real object is transferred into digital form. The scanned data comprises so-called point clouds; this means each scanned point has a position in space in terms of a coordinate system. The machined surfaces were scanned with ATOS Triple Scanner. A photographic view of this scanner is shown in Figure 5.9.

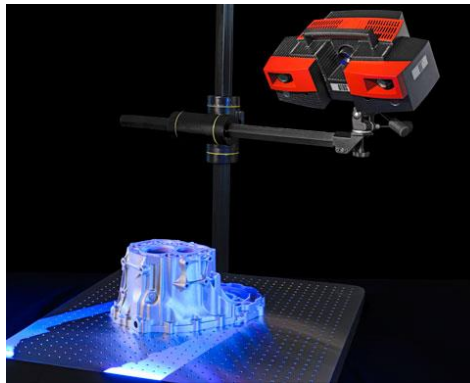


Figure 5.9 Photographic view of 3D scanner

CHAPTER 6

VERIFICATION OF ELECTROCHEMICAL MACHINED (ECMed) FREE-FORM SURFACES

6.1 Introduction

This chapter investigates the drawbacks to ECM that affect machining of freeform surfaces. These drawbacks are categorised into three main groups: short-circuiting, cavitation and oxide-layer formation.

6.2 Drawbacks of Free-Form Surface Machining

Each of the drawbacks on anode and cathode and the proposed control systems are explained below. First, it is inefficient to use voltage as feedback to prevent short circuiting; therefore, both current and voltage were chosen for feedback. Second, electrolyte flow between anode and cathode was modelled via ANSYS for every apparatus that is discussed in Section 6.4. Last, the effect of contamination on oxide layer formation is discussed and the filtering system was changed.

6.2.1 Effect of Short Circuiting

Short circuiting is a drawback in ECM that can damage the anode and cathode surfaces. A short circuit is an electrical circuit that allows a current to travel along an unintended pathway with no or very low electrical impedance. This means that when the voltage approaches zero, the current tries to reach infinity or the limit values chosen by the operator. A short circuit example that occurred during ECM is shown in Figure 6.1.

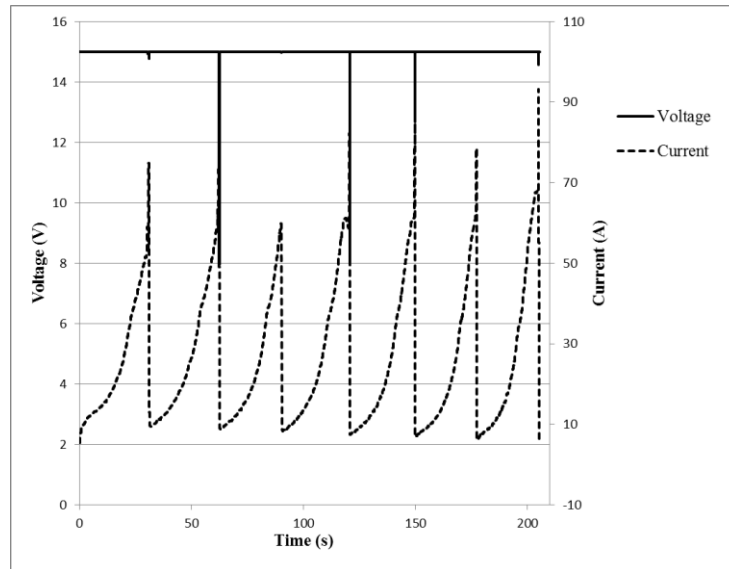


Figure 6.1 Short circuit occurrence

In order to avoid a short circuit, a closed-loop control system was developed. In this system, first voltage and then current and voltage together were used as dynamic feedback to observe the efficiency of this control mechanism on short-circuit control. By programming the DC power supply, voltage and current can be read as an analogue or digital signal. A micro-controller board was used to check these values and provide communication between the DC power supply and the motion control system of the ECM process.

The EC machine motion system was provided by step motors and controlled by Mach3 (Newfangled Solutions, USA) software, which provided control step or servomotor motion by processing G-codes. A schematic view of the short-circuit control system is shown in Figure 6.2.

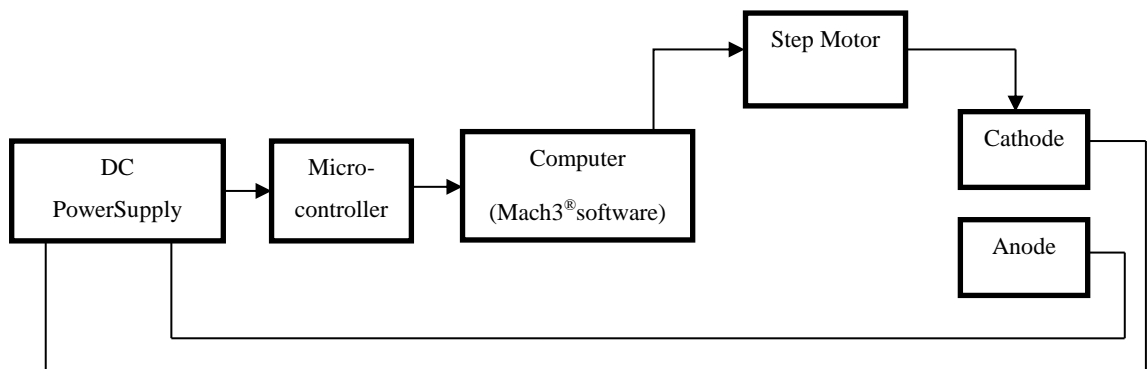


Figure 6.2 Short-circuit control system

According to the schematic of the short-circuit control system, the control board reads and checks the analogue output values from the DC power supply and sends the results to the Mach3 software. If the voltage and/or current values exceed the limits, the Mach3 stops the motion, rewinds, and re-starts the system.

6.2.2 Effects of Cavitation

According to fluid-dynamic multiphase flow, turbulent and transient flow between an anode and a cathode causes cavitation. Different types of cavitation are described in the literature, but the most frequently encountered type for ECM is transient cavitation [103]. According to this cavitation type, cavitation bubbles grow extensively and then undergo energetic collapse, which usually occurs in less than one microsecond [104].

Due to the complex geometry of the gap between the anode and the cathode, it was difficult to obtain a steady flow; therefore, special apparatus was designed for the experiments, as shown in Figure 6.3. Apparatuses 1 and 2 were designed according to the geometry of the cathode and the anode, respectively, and electrolyte transfer was from one side. Apparatus 3 was designed according to the geometry of both the anode and the cathode, the electrolyte inlet was from two sides, and the outlet was created according to the gap geometry between the two pieces of apparatus. Apparatus 4 was designed according to the cathode surface and can be described as a freeform surface. The electrolyte inlet was made from one side and the electrolyte flow rate was increased by increasing the hole number. The pieces of apparatus were made by a 3D printer with a dimensional accuracy of 0.012 mm for the x- and y-axes and 0.004 mm for the z-axis. The pieces of apparatus were made of a plastic, non-conductive material.

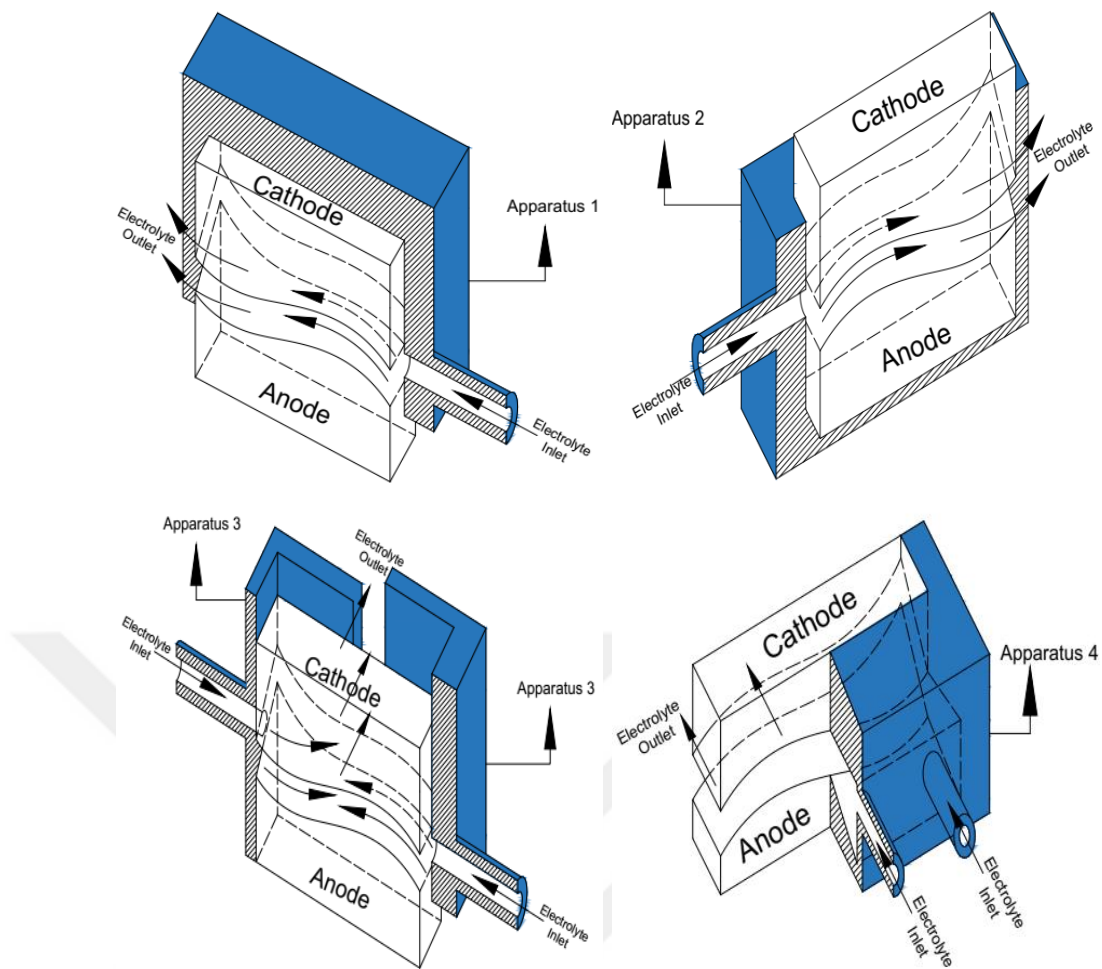


Figure 6.3 Schematic of apparatus for electrolyte transfer

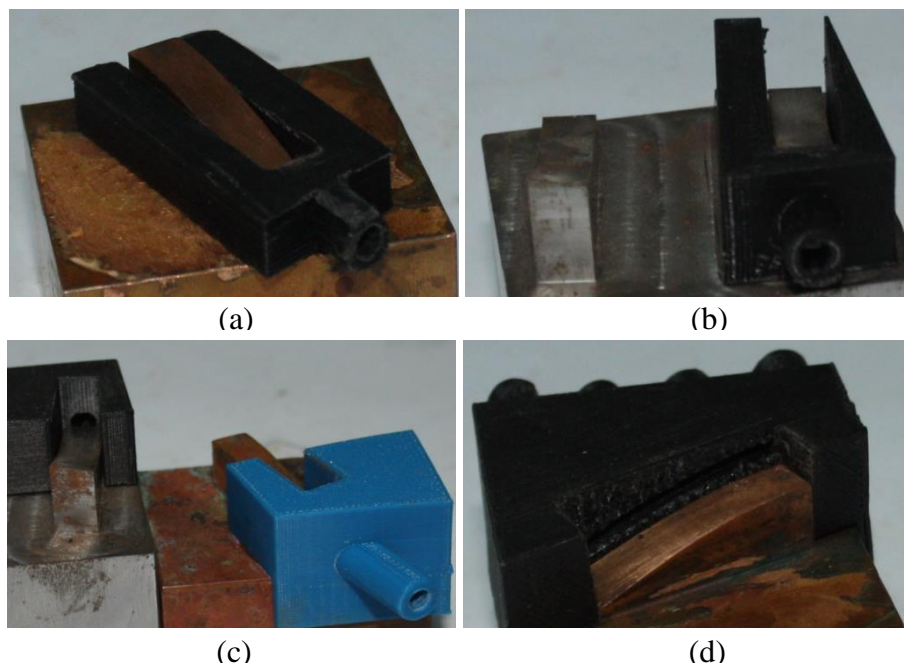


Figure 6.4 Photographic view of (a) apparatus 1, (b) apparatus 2, (c) apparatus 3 and (d) apparatus 4

6.2.3 Effect of Oxide Layer

The chemical composition of 1040 carbon steel means it has low corrosion resistance; its chemical composition is shown in Table 6.1.

Table 6.1 Chemical composition of 1040 carbon steel

Element	Fe	Mn	C	S	P
Content (%)	98.6-99	0.6-0.9	0.37-0.44	≤ 0.05	≤ 0.04

Because 1040 carbon steel is mainly iron (Fe), the formation of an oxide layer varies according to the ion types of the Fe . The anodic dissolution of Fe in neutral $NaCl$ solutions can be written as [105]:



assuming an active or transpassive process. This reaction is normally used to calculate efficiencies, but it has been observed that this is not the only product in nitrate solutions [92]. If the surface is covered by an oxide film (e.g., Fe_2O_3), a passive dissolution according to:



is probable. The situation becomes more complex as oxygen evolution proceeds concurrently [92]:



Here, Fe^{2+} ions can be oxidised in the electrolyte. Altogether, three main products are possible: Fe^{2+} , Fe^{3+} and oxygen.

The most frequently encountered iron oxide layer-types are Fe_2O_3 and Fe_3O_4 for ECM of iron and iron-based alloys. An Fe_2O_3 oxide layer containing only Fe^{2+} ions is called ferric oxide, and is dark red. However, an Fe_3O_4 layer containing both Fe^{2+} and Fe^{3+} ions is called ferrous-ferric oxide and is coloured black.

6.2.4 Short Circuit Control

The short-circuit control system was designed by controlling the voltage values. The DC power supply read the voltage between the anode and the cathode and sent the data as analogue signals to the micro-controller board. The control board checked the data. If the voltage dropped, it sent a signal to the Mach3 software to stop the cathode movement and the operation restarted from the beginning.

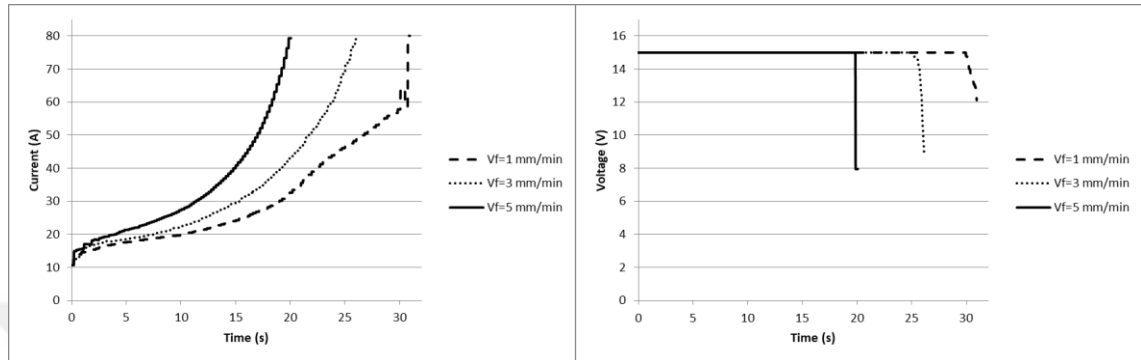


Figure 6.5 Variation of voltage (a) and current (b) for different feed rates

Figure 6.5.a and Figure 6.5.b show the variation in current and voltage for different feed rates, respectively. Time 0 indicates the beginning of the operation. At constant feed rates, the tool (cathode) travelled different distances over the same amount of time. Therefore, a high feed rate lead to a small gap distance between the anode and the cathode. According to first law of electrolysis, the current value is inversely proportional to the distance between two electrodes; Figure 6.5.a verifies this law. As can be seen in Figure 6.5.b, a voltage decrease becomes suddenly shorter than 25 ms for 5 mm/min, 1 s for 3 mm/min and 2 s for 1 mm/min feed rates. As discussed above, a short-circuit occurs with low electrical impedance. A decrease in the distance between the anode and the cathode causes low electrolyte flow. Moreover, waste products that occur via machining are carried away by the electrolyte. A high feed rate would lead to generation of waste bulk via a poorly-made electrolyte transition. This may cause the voltage to decrease faster at higher feed rates. At higher cathode feed rates, the time was too short to read and process the data; this caused short-circuiting between the anode and the cathode. This showed that only the voltage control was successful for lower feed rates. Additional experiments showed that cathode material is effective in controlling short-circuiting. This can be attributed to the electrical conductivity and chemical composition of the material. As shown in Table 5.5, copper is the most conductive material. In addition, copper has the highest purity in comparison with the

other materials. A resulting damaged cathode surface due to short-circuiting is shown in Figure 6.6.

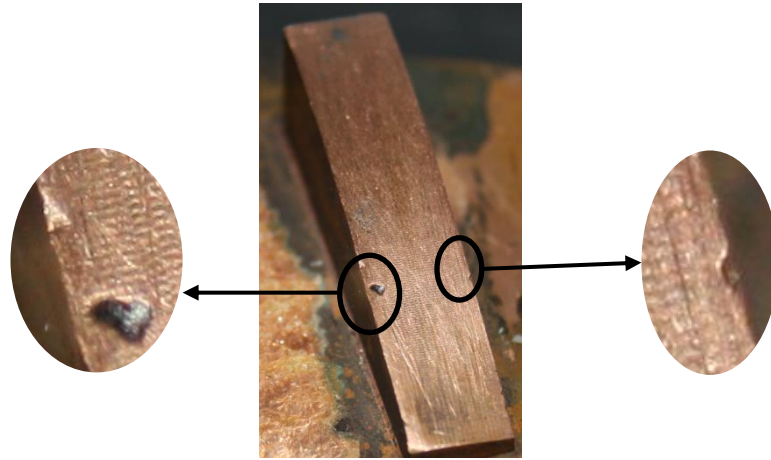


Figure 6.6 Damaged cathode surface due to short-circuiting

The current change that is shown in Figure 6.5.a can be described as a polynomic function of time. The descriptions discussed above demonstrate that short-circuiting is related to voltage and current. With this assumption, the system control parameter changed from voltage, to voltage and current together. A flow chart of the short-circuit control system is shown in Figure 6.7. In this study, current was limited to 70 A, as defined by experimental observations. The system checked the current values; if the current exceeded the limit, the cathode feed was stopped by the control system and restarted from the initial cathode position.

6.2.5 Cavitation Control

In multiphase flow regions to characterise how close to formation of cavitation by means of the cavitation number, Q , defined by Eq. 6.4.

$$Q = 2 \cdot \frac{P_{\infty} - P_V}{\rho_{el} \cdot V_{\infty}^2} \quad (6.4)$$

where P_{∞} and P_V are the reference and vapour pressure of the electrolyte, ρ_{el} is the density of the electrolyte and V_{∞} is the velocity of the electrolyte. In a given flow, as Q is reduced, cavitation will first occur at some given value of Q . This is called the incipient cavitation number and is denoted by Q_i . Any further reduction in Q below Q_i would cause an increase in the number and size of the vapour bubbles [103]. As can be seen from Eq. 6.4, effective variables for defining cavitation number are reference pressure and velocity of the electrolyte in the flow region.

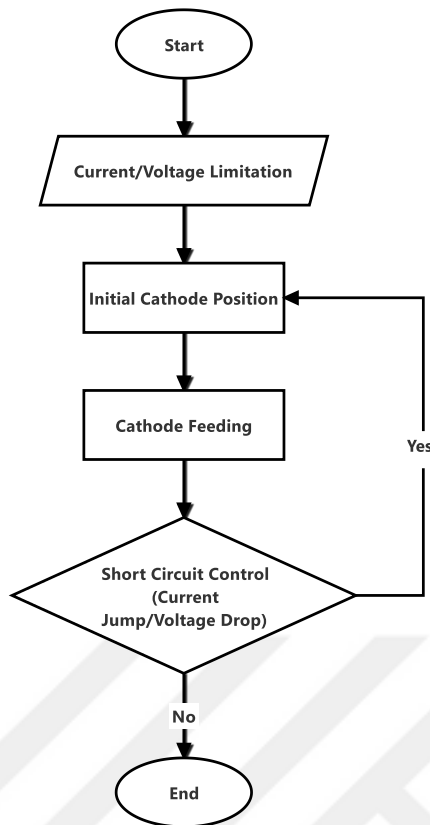


Figure 6.7 Flow chart of the short-circuit control system

As discussed in Section 6.2.2, four different apparatus designs were used to detect the cavitation effect of ECM. For apparatuses 1 and 2, the electrochemical machined surfaces are shown in Figure 6.8.a and Figure 6.8.b. As can be seen from the photograph, cavitation occurred on the surfaces that were farthest from the electrolyte inlet. To describe these results, electrolyte flow between the anode and the cathode was simulated using the ANSYS software. The calculations were carried out on a PC (Core i5, 2.8GHz, 8GB RAM). The mesh densities on the anode and cathode surfaces were increased five-fold compared to other regions, in order to observe the variations of the electrolyte flow on these surfaces. Figure 6.9 shows a mesh convergence study for the average velocity of the outlet for all pieces of apparatus. Three different mesh sizes, ranging from 1 mm to 0.1 mm, were applied to demonstrate that the number of elements had no effect on the solution.

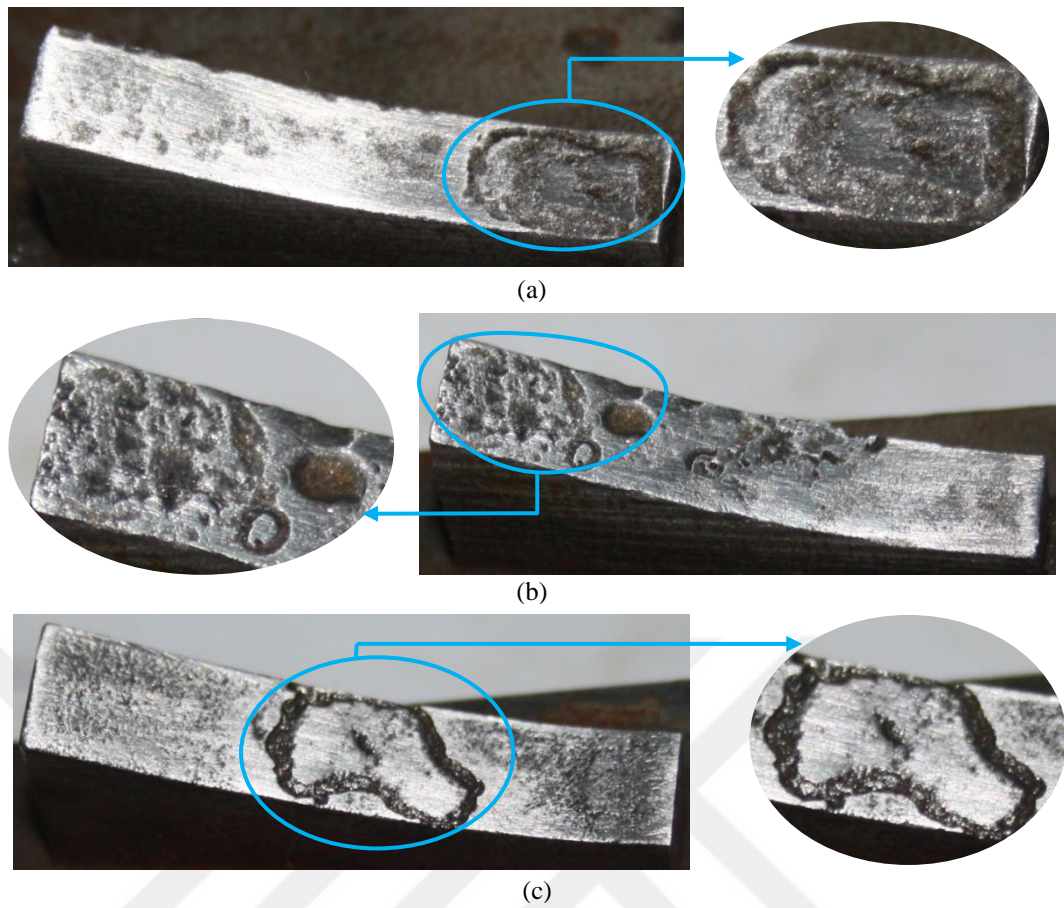


Figure 6.8 Electrochemical machined surfaces of apparatus 1 (a), apparatus 2 (b) and apparatus 3 (c)

The simulation parameters were chosen according to fluid dynamic principles, which are discussed above and shown in Table 6.2.

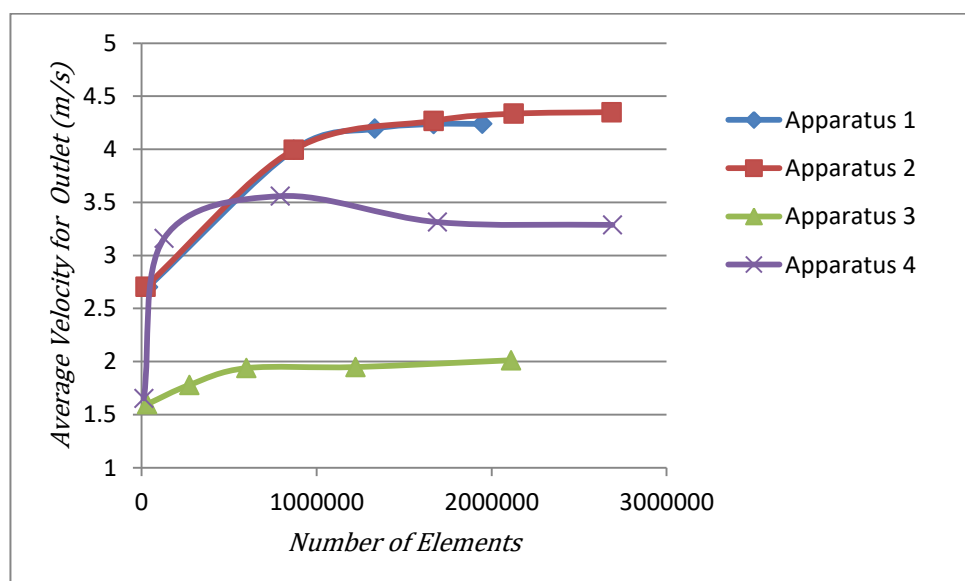


Figure 6.9 Average velocity vs. number of elements for all pieces of apparatus

Electrolyte velocity distribution between the anode and the cathode for apparatus 1 is shown in Figure 6.10. Similar results were obtained for apparatus 2. The electrolyte velocity values on the anode and cathode surfaces that were near the electrolyte outlet were almost 0; it may be that the inlet velocity was too low to pass the fluid area. This situation can be avoided with increased electrolyte inlet velocity; however, this causes turbulent flow, which verifies Banks and Campton [103].

Table 6.2 Parameters for ANSYS simulation

Flow Type	Mesh Type	Mesh Size (mm)	Inlet Velocity (m/sec.)	Time	Solver Type
Laminar	Triangular	0.1	5.53	Steady	Pressure- based

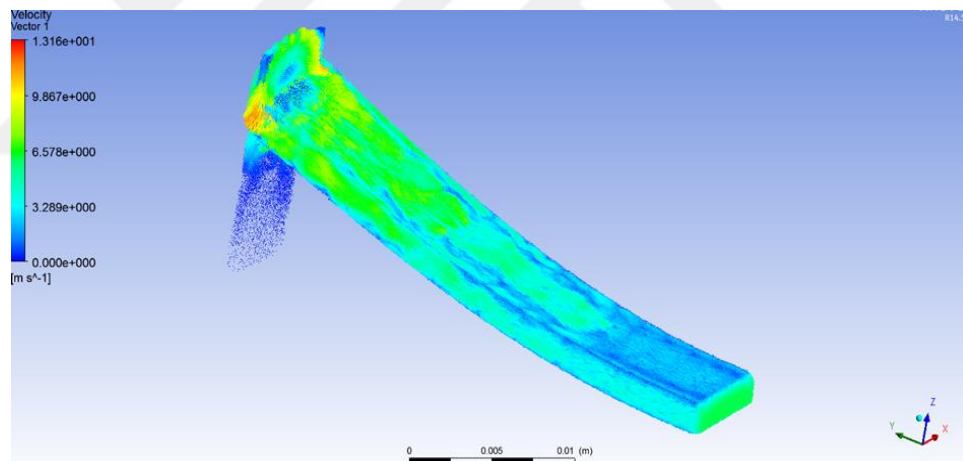


Figure 6.10 Velocity distribution via ANSYS simulation for apparatus 1

For apparatus 3, there was no cavitation formation on the sides of the anode surface; however, cavitation formation was observed in the middle of the anode. The machined anode surface of apparatus 3 is shown in Figure 6.8.c.

This could be explained by turbulent flow in the region of the electrolyte outlet. The simulation results also confirmed this assumption, as shown in Figure 6.11. In the middle of the fluid area, an incompressible fluid formed as the electrolyte tried to flow out the shortest way. Furthermore, the electrolyte could not be transmitted through the centre of the fluid area, which caused cavitation to occur. Moreover, cavitation bubbles

may have occurred below the vapour pressure via turbulent eddies, which is an important variable shown in Eq. 6.4.

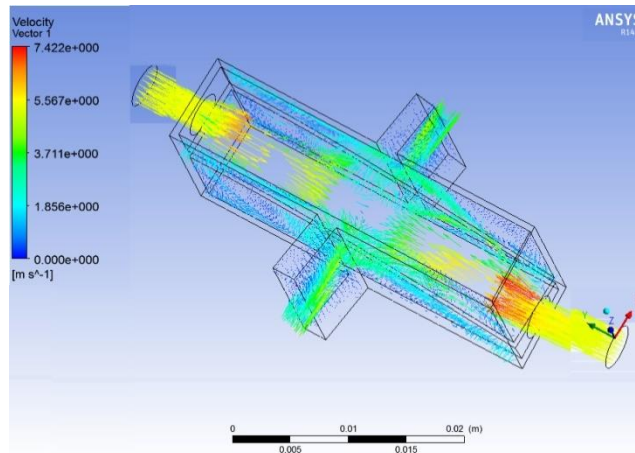


Figure 6.11 Velocity distribution via ANSYS simulation for apparatus 3

As described above, electrolyte flow rate could be increased for apparatus 4, and the flow distance was the shortest compared to the other pieces of apparatus. In addition, the electrolyte inlet was on one side with a high flow rate; by means of this, turbulent flow was minimised. In addition, the simulation results showed that the velocity distribution in the fluid area was better distributed than the other apparatus results and electrolyte transition was more homogenous in the gap domain. Simulation results for apparatus 4 are shown in Figure 6.12.

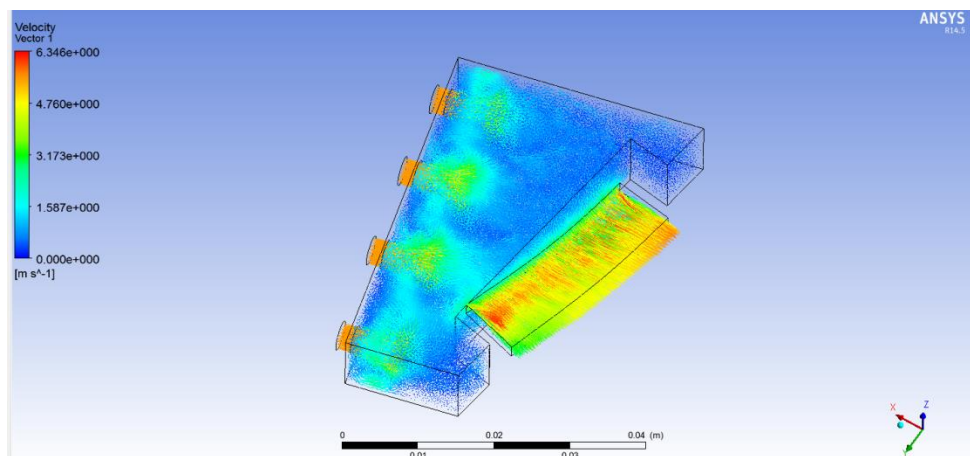


Figure 6.12 Velocity distribution for apparatus 4

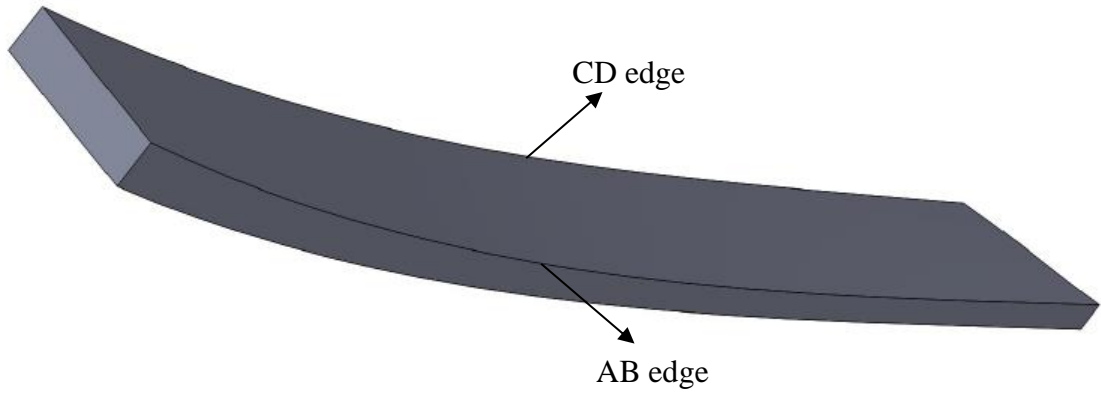


Figure 6.13 Edges of gap domain: CD is the input edge, AB is the output edge

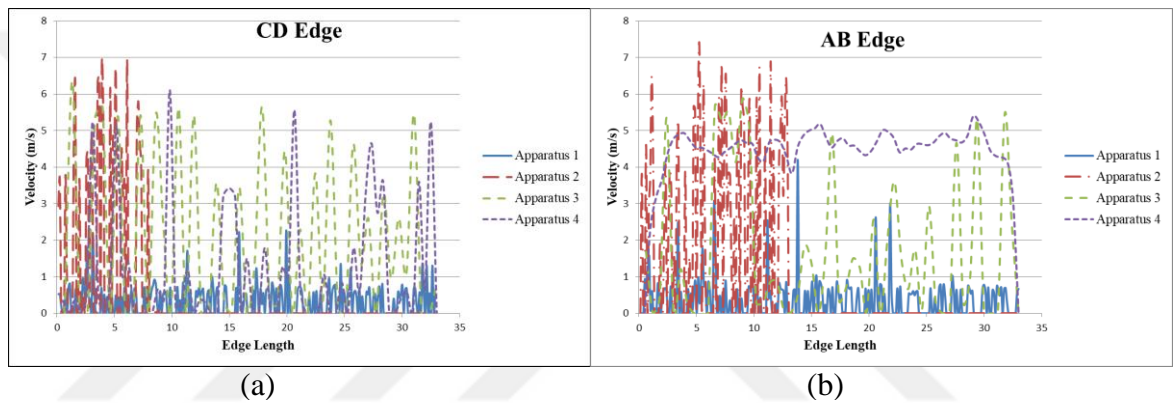


Figure 6.14 Variation of velocity along (a) CD edge and (b) AB edge

Figure 6.14.a and Figure 6.14.b show the variation of velocity along the edges of the gap domain. CD is the input edge and AB is the output edge, as shown in Figure 6.13. As can be seen from Figure 6.13.a, electrolyte transition occurred at low velocities for apparatus 1. For apparatus 2, velocity decreased to 0 after 6 mm edge length and did not change up to the end of edge CD. This means all flow occurred at an edge with a length of 6 mm. However, the electrolyte flowed by fluctuating along the entire input edge for apparatuses 3 and 4. Similar results were obtained for the AB edge, which is shown in Figure 6.14.b for apparatuses 1, 2 and 3. For apparatus 4, however, velocity distribution was better than all others along the AB edge. The average velocity at the outlet edge of the gap domain was 3.4 m/s; when comparing the velocity decrease for all pieces of apparatus, it decreased even more for apparatus 4. Therefore, using this, material was removed from the workpiece more adequately due to well-made electron transition.

6.2.6 Oxide Layer Control

To investigate oxide layer formation, optimum conditions were used as discussed above. For filtering contamination from the electrolyte, activated carbon and Whatman[®] filter papers were used. The experiments showed that for high current values, a black oxide layer formed. Since it was Fe_3O_4 , it indicated that the filtering system was not suitable for the ECM process. Furthermore, the oxide layer that formed on the workpiece verified Lohrengel et al. [92]. The electrochemical machined surface where the oxide layer occurred is shown in Figure 6.15.a.

Datta and Landolt [106] investigated the influence of flow rate and current density on surface brightening of iron and nickel using ECM. In their study, the electrolyte transfer system was a discontinuous type that used an electrolyte transferred to a waste water line. In the current study, the electrolyte transfer system was therefore changed from a continuous to a discontinuous type. In this way, contamination of the electrolyte was removed from the machining area and oxide layer generation was avoided. The electrochemical machined surface, after changing the electrolyte transfer system, is shown in Figure 6.15.b.

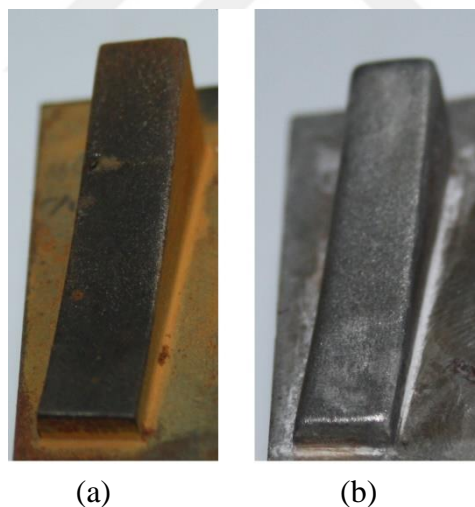


Figure 6.15 Electrochemical machined surface with oxide layer (a) and without oxide layer (b)

6.3 Cathode Design Considerations

Verification of the ECMed freeform surfaces was made by comparing the mesh and exact CAD model of the anode surface. The mesh model has been created via the control points that were obtained by using a 3D scanner. In order to investigate the effect of parameters on freeform surface machining and validity of mathematical model

Dimensional error (DE) values have been investigated. DE describes the distance between the control points on ECMed surface and exact CAD model in the z direction. A schematic of DE measurement is shown in Figure 6.16.

In Figure 6.16 continuous line and circles describes the anode surface CAD model of the anode surface and control points respectively. A dashed line with plus signs describes the ECMed anode surface with control points. Additionally red and blue coloured curves describes the edges that $v = 0$ and $v = 1$ respectively.

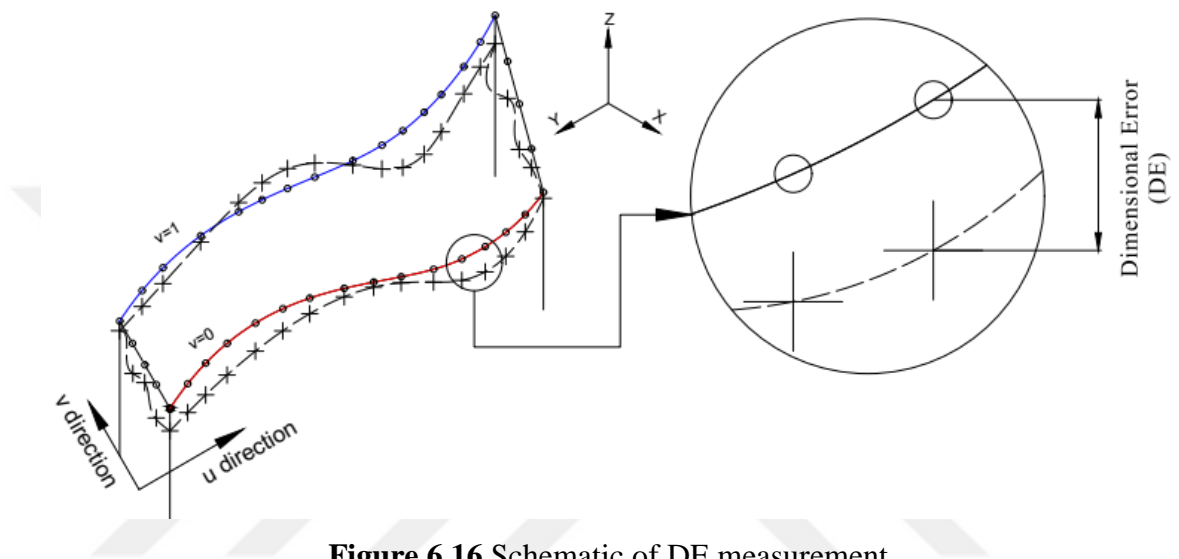


Figure 6.16 Schematic of DE measurement

Freeform surfaces have complex geometries to describe in $x - y$ dimensions. Because of this, workpiece geometry is transferred from the $x - y - z$ dimension to the $u - v$ dimension. DE was investigated in the u and v directions. The u and v directions of the workpiece surface are shown in Figure 6.17.

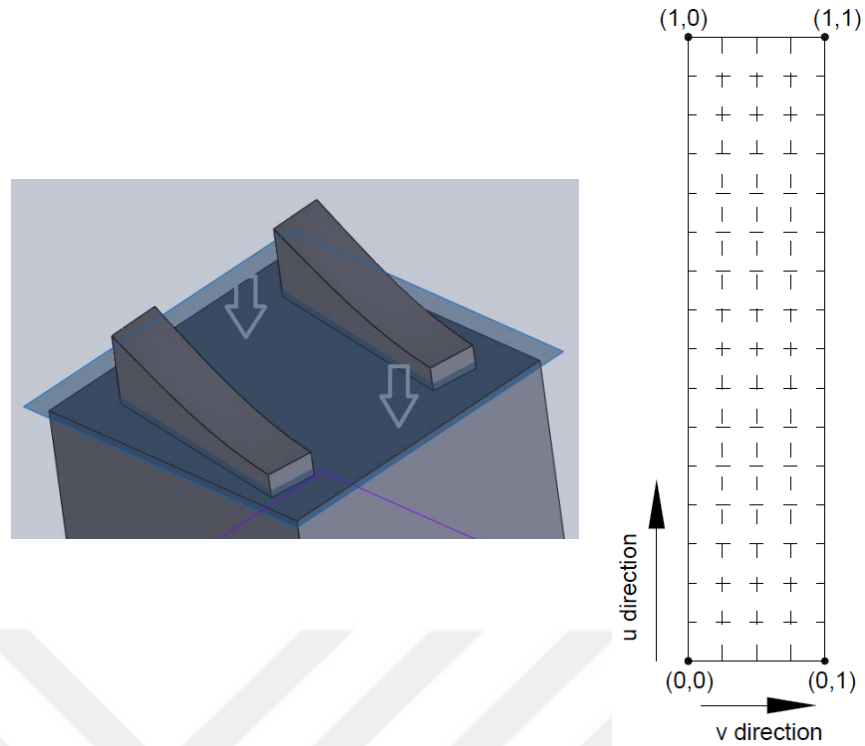


Figure 6.17 The u and v directions of the workpiece surface

The minimum and maximum DE for experimental conditions is shown in Table 6.3. As can be seen from Table 6.3, the DE changed simultaneously for all experimental conditions, especially for minimum DE (over machining). Therefore, DE was investigated in detail.

Table 6.3 Minimum and maximum DE for experimental conditions

	Experimental Condition								
	1	2	3	4	5	6	7	8	9
Min. DE (mm)	-0.453	-0.497	-0.436	-0.3	-0.169	-0.446	-0.489	-0.294	-0.326
Max. DE (mm)	0.207	0.432	0.409	0.375	0.254	0.238	-0.035	0.264	0.144

In this study, machining depth distance of the cathode (in the z dimension) was 2 mm. Machining Error Rates (MER) are used to discuss the validity of the mathematical model. MER (%) can be calculated with using Eq. 6.5 and the MER values for experimental conditions are shown in Table 6.4.

$$MER = \frac{d_m - DE}{d_m} \cdot 100 \quad (6.5)$$

where MER is the machining error rate, d_m is the machining depth, DE is the dimensional error. In Table 6.4 minus signed MER describes the over machining on anode surface.

Table 6.4 MER values for experimental conditions

	Experimental Condition								
	1	2	3	4	5	6	7	8	9
Min. MER (%)	-22.65	-24.85	-21.8	-15	-8.45	-22.3	-24.45	-14.7	-16.3
Max. MER (%)	10.35	21.6	20.45	18.75	12.7	11.9	-1.75	13.2	7.2

6.3.1 Effect of the Electrolyte

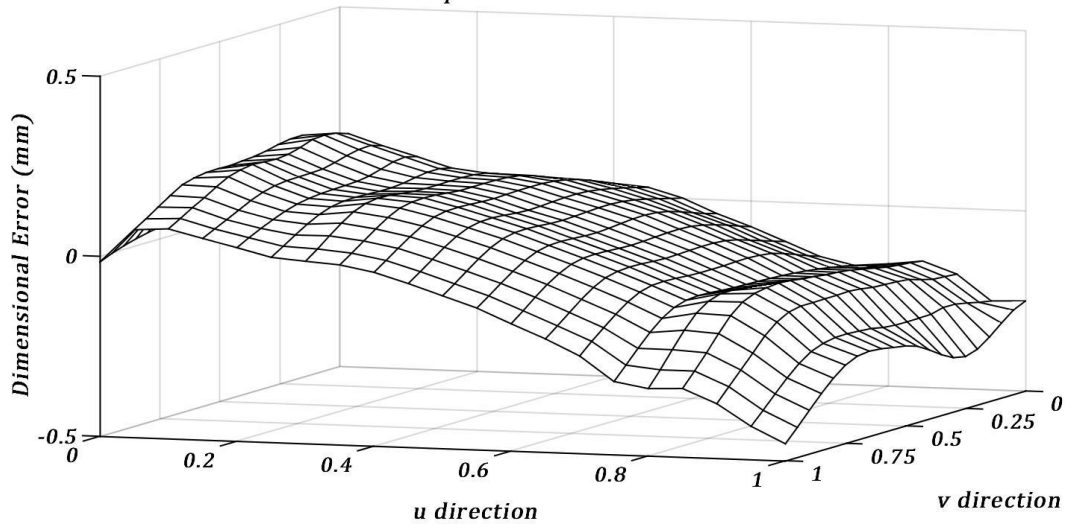
Figure 6.18 shows the variation of DE with the u and v directions. As can be seen from Figure 6.18, variation of DE occurred similarly at $v = 0.25$, $v = 0.5$ and $v = 0.75$. But at $v = 0$ and $v = 1$, variation of DE occurred differently. When the conditions described in Figure 6.17 were investigated, $v = 0$ and $v = 1$ were the right and left edges of the workpiece. But over machining (minus signed DE), some of them occurred at $v = 1$, (Experimental Conditions 1, 2, 3, 6, 8 and 9) and some of them at $v = 0$, (Experimental Conditions 4, 5 and 7). This was because electrolyte transition occurred from the left edge for Experimental Conditions 4, 5 and 7 and the right edges for Experimental Conditions 1, 2, 3, 6, 8 and 9. Due to design of the workpiece, the electrolyte cannot be transferred from the left or right edge for all experimental conditions. As described above, a $NaCl$ type electrolyte was used for the experiments. In water, $NaCl$ dissolves completely, forming Na^+ and Cl^- ions; therefore, it is classified as a strong electrolyte. Due to electrolyte's chemical properties, Cl^- anions cause chemical reaction occurrence with Fe^{2+} or Fe^{3+} cations to create $FeCl_2$ or $FeCl_3$. Additionally, the bulk at the gap inlet can cause a turbulence flow that can change the ion transfer to undesired levels. Furthermore, with feeding, cathode chemical reactions can occur on the lateral face of the anode. Therefore, machining occurred

before the electrolyte transferred to the gap between the anode and the cathode. A schematic of this phenomenon is shown in Figure 6.19. But DE behaved in a similar fashion for $v = 0.25$, $v = 0.5$ and $v = 0.75$. This can be attributed to the fact that, in the middle of the gap domain, the electrolyte transitioned well; therefore, electrolytes' properties (such as temperature, pressure, and velocity) could be kept at similar values.

As can be seen from Figure 6.19, the electrolyte showed a flushing effect where it left the machining gap. Because of the poorly distributed electrolyte, the DE showed differences at this edge for experiments. Variation of DE with u direction for all experimental conditions is tabulated in Appendix C.

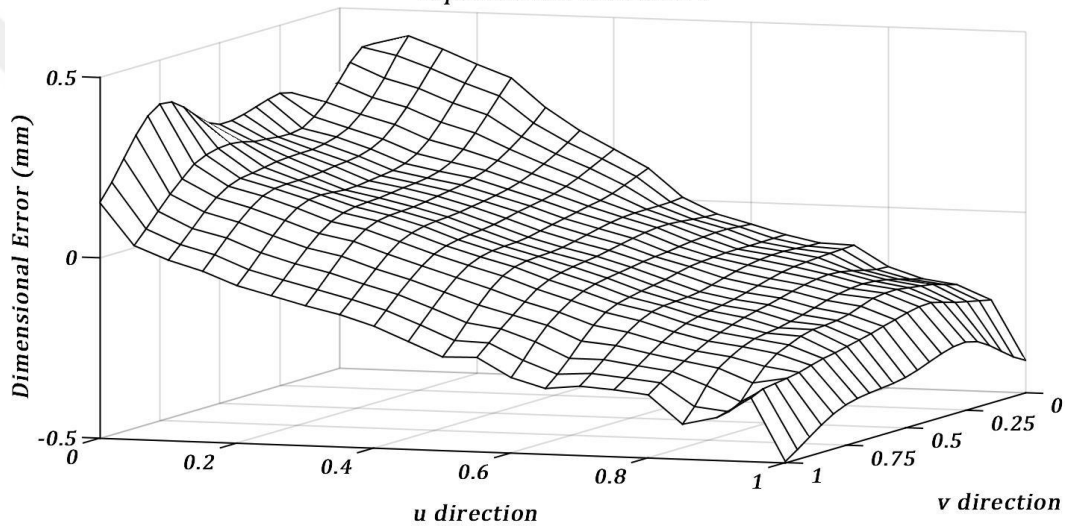


Experimental Condition 1



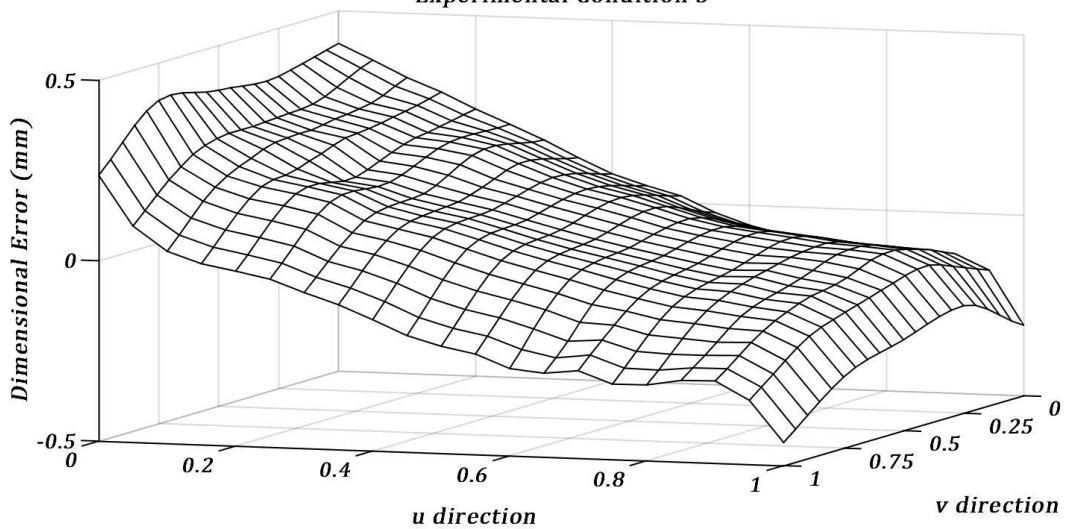
(a)

Experimental Condition 2

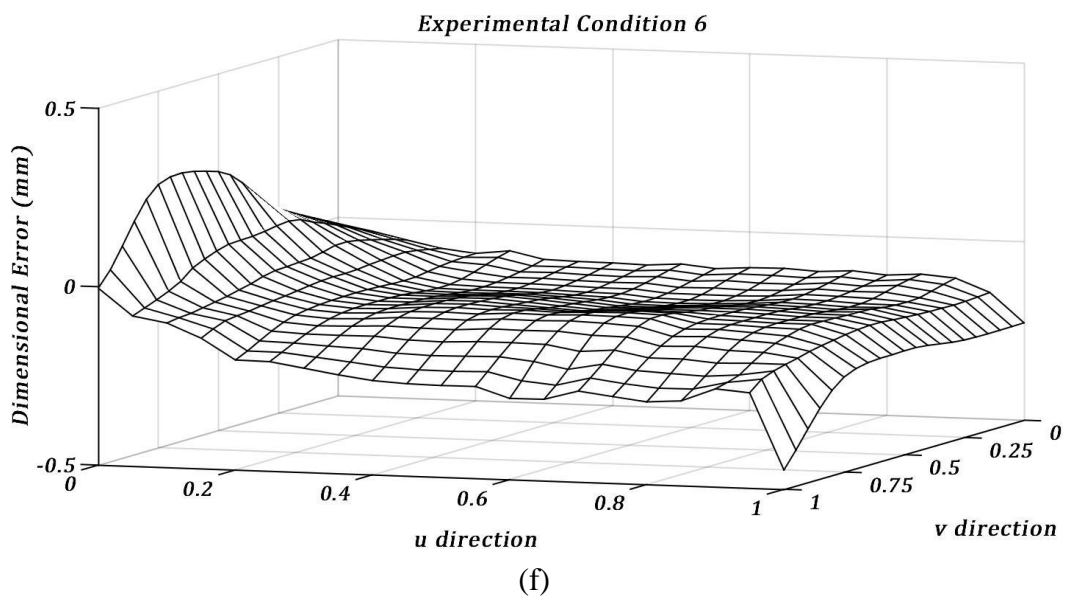
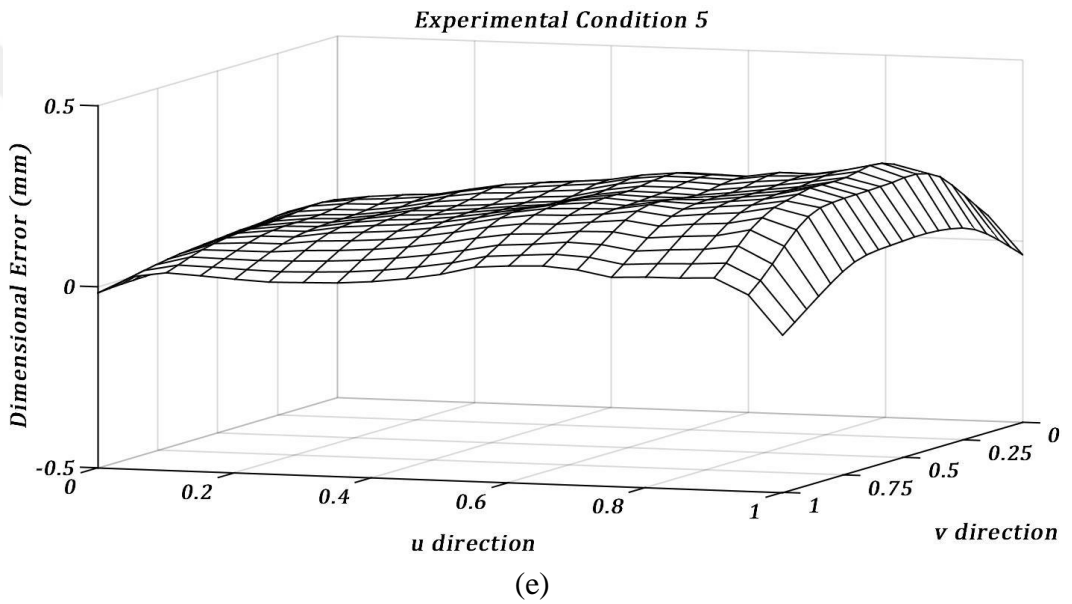
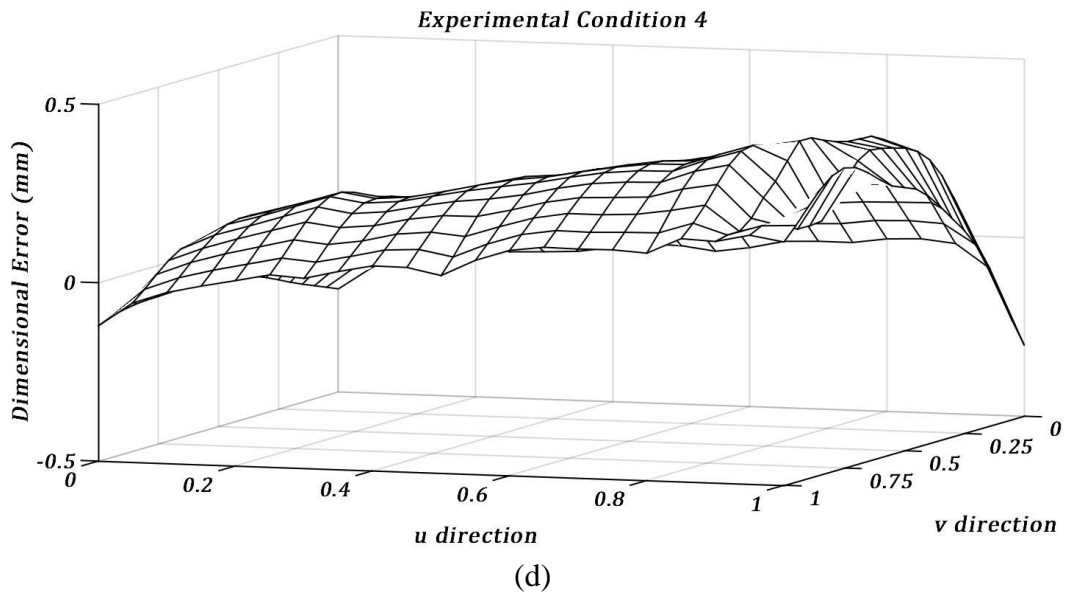


(b)

Experimental Condition 3



(c)



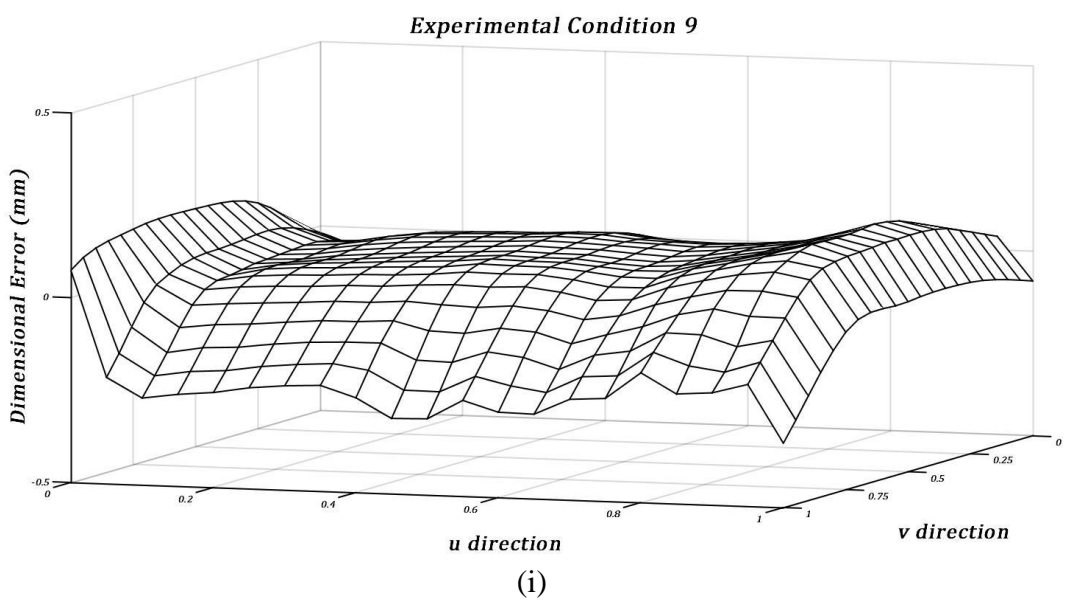
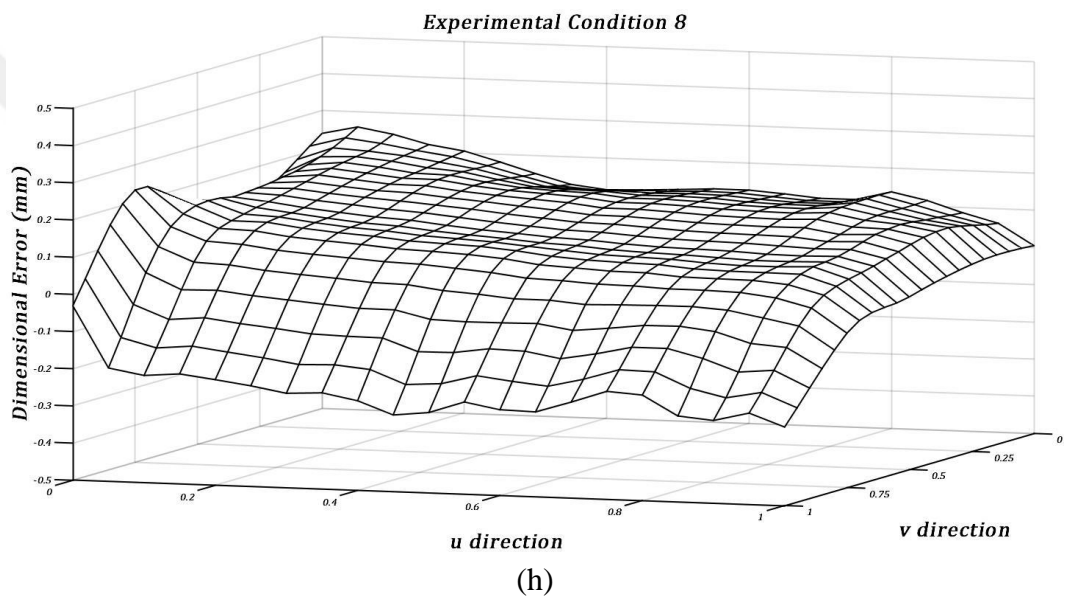
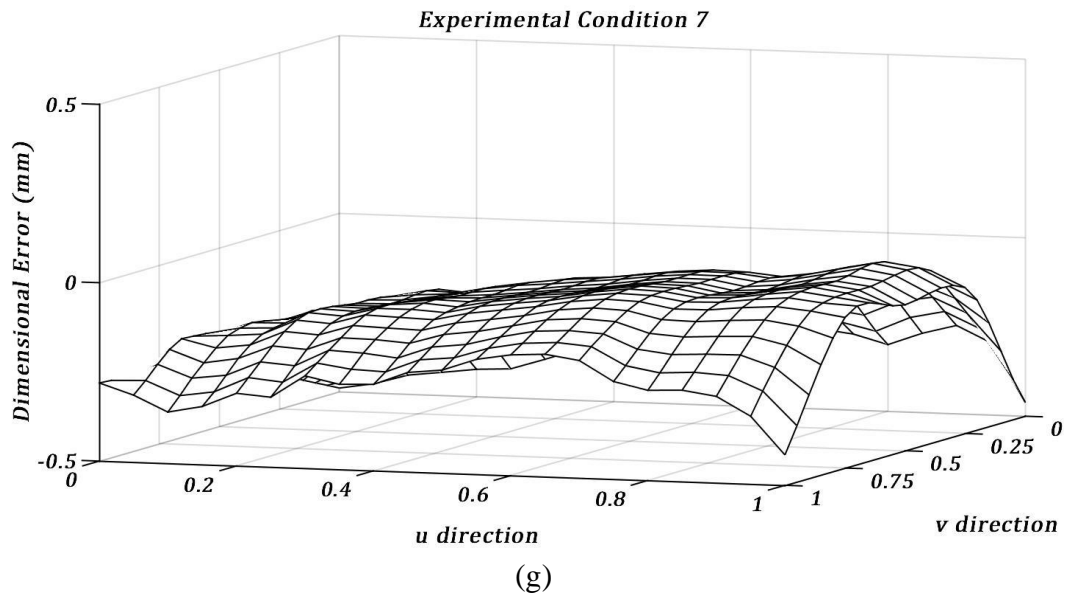


Figure 6.18 Variation of DE with the u and v directions for experimental conditions

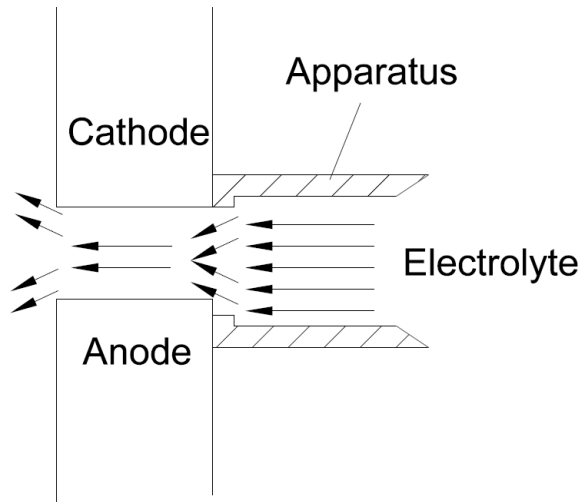
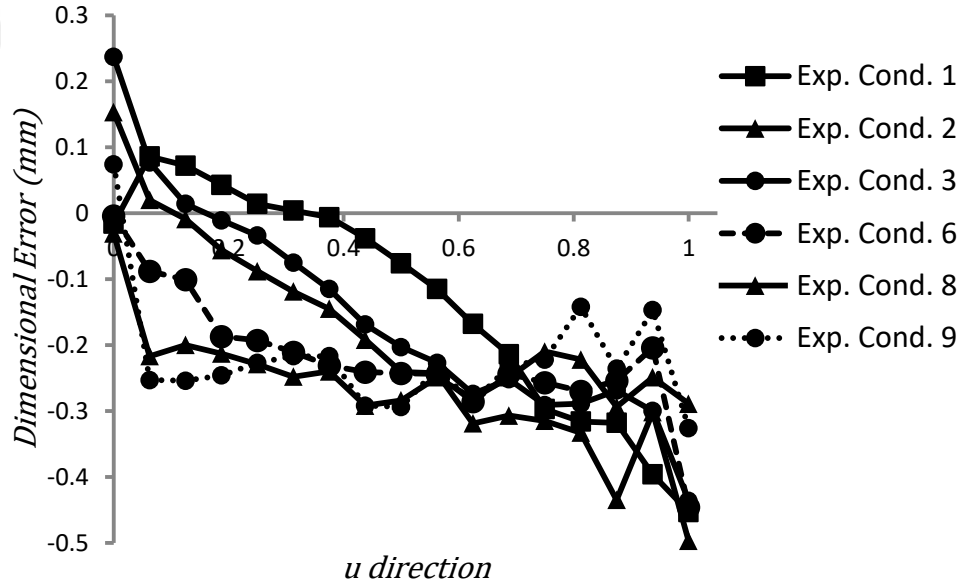


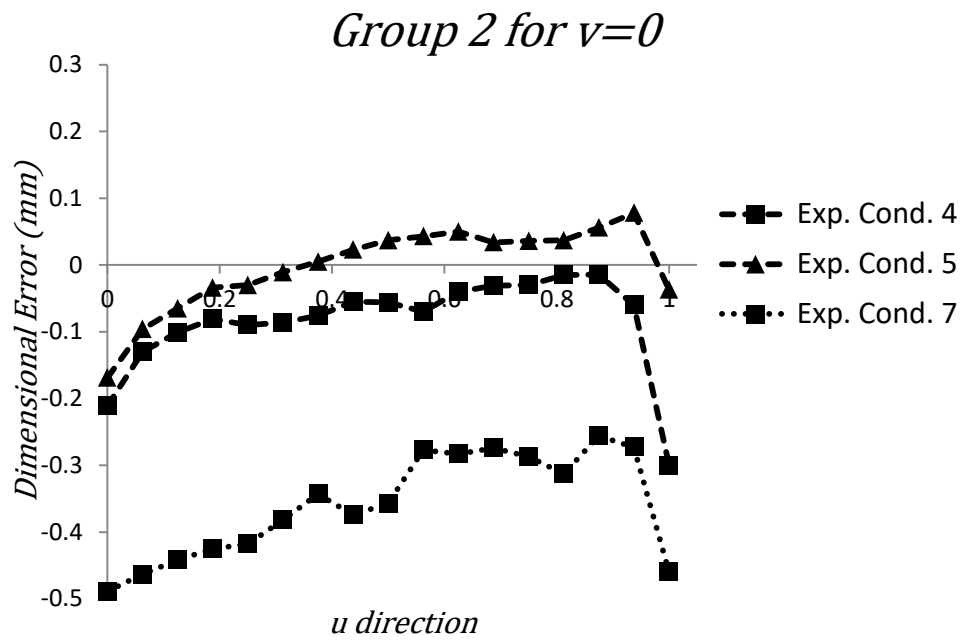
Figure 6.19 Schematic of the over-machining phenomenon during electrolyte transition

To discuss the effect of parameters (feed rate and electrical conductivity) on the over-machined side, experimental conditions were investigated in two main groups. Experimental Conditions 1, 2, 3, 6, 8 and 9, for which electrolyte transition occurred from the left side of the workpiece, comprise Group 1, and Experimental Conditions 4, 5 and 7 comprise Group 2.

Group 1 for $v=1$



(a)



(b)

Figure 6.20 Variation of DE with the u direction for (a) Group 1 for $v = 1$ and (b) Group 2 for $v = 0$

Figure 6.20 shows the influence of DE with the u direction (a) for Group 1 at $v = 1$ and (b) for Group 2 at $v = 0$. As discussed in Eq. 4.4, the removed material is proportional with the applied current, time, and electrochemical machinability of the workpiece. In this study, voltage was kept constant. Therefore, the current was directly proportional to the electrical conductivity of the electrolytes; consequently, an increase in electrical conductivity was caused in minus DE, which is shown in Figure 6.20.a and Figure 6.20.b. Additionally, the most that DE has been observed continuously is in Figure 6.20.b for Experimental Condition 7. This can be attributed to not only electrolyte conductivity but also to the time that the cathode was exposed to highly conductive electrolytes. When Table 5.1 is investigated, it will be seen that the electrical conductivity of the electrolytes in Experimental Condition 7 was higher than Experimental Conditions 4 and 5. Moreover, the initial gap that was calculated via the mathematical model was longer than that of Experimental Conditions 4 and 5. Therefore, the edge was exposed to the electrolytes for a longer period of time, which caused over-machining at this edge. The DE decrease is shown in Figure 6.20.a, and the DE increase is shown in Figure 6.20.b. The reason of the different DE variation shown in Figure 6.18.a and 6.18.b is the geometry of the workpiece, such that one electrolyte

moved upward while one moved downward. A schematic of electrolyte transition via the right and left edges is shown in Figure 6.21.

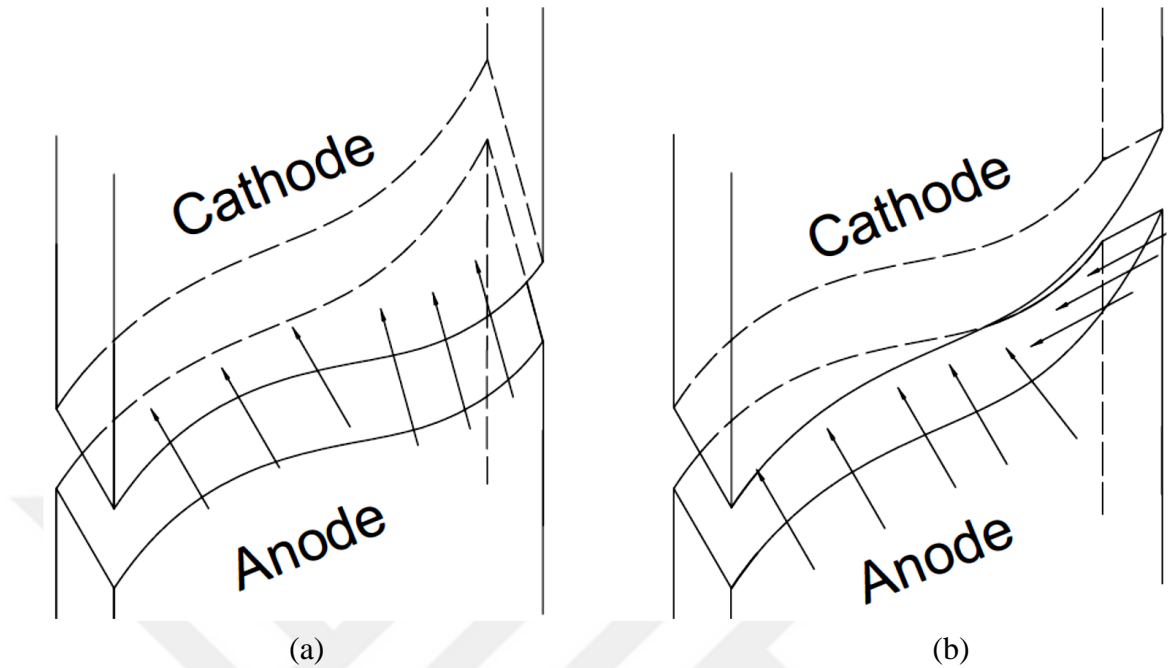
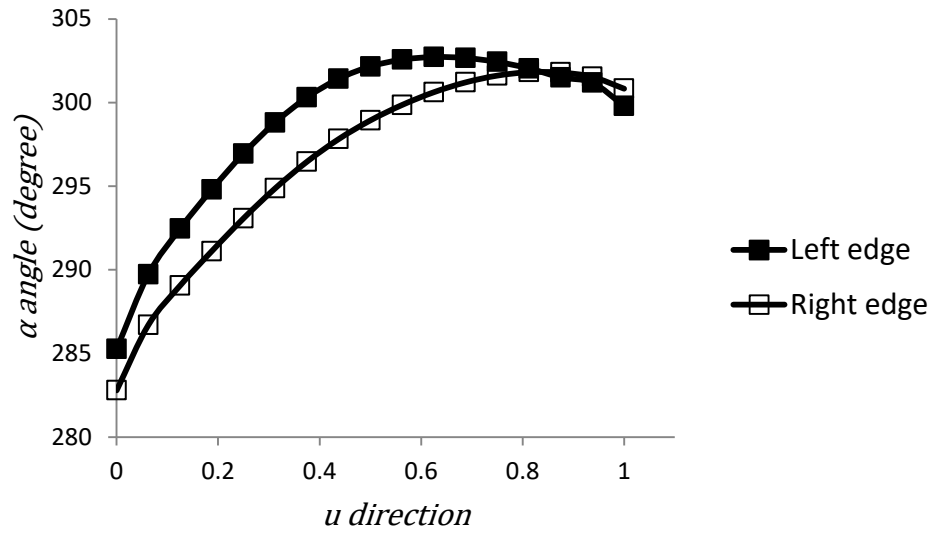


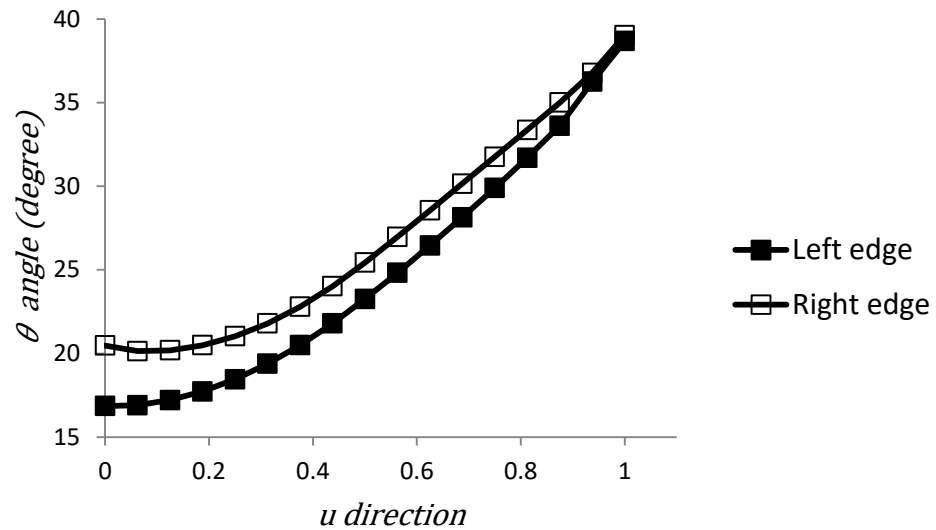
Figure 6.21 Schematic of electrolyte transition via (a) left and (b) right edges

As can be seen in Figure 6.20.a and Figure 6.20.b, DE variation shows a decrease and increase, respectively, from $u = 0$ to $u = 0.685$. Figure 6.22.a and Figure 6.22.b show the variation of α and θ angles with u direction for the left and right edges of the anode, respectively. α and θ angles are described in Section 3.3 and can be calculated by using Eq. 3.11 and Eq. 3.12. As can be seen from Figure 6.22.a, the α angle difference between the left and right edges increases from $u = 0$ to $u = 0.625$. After $u = 0.625$, the difference is shown in a decrease and, after $u = 0.75$, values of α and θ angles becomes similar. Additionally, the difference in θ angles between the two edges in Figure 6.22.b shows a decrease after $u = 0.625$.

The curve geometry of the left and right edges causes differences in α and θ angles. Higher θ angles describe the change of curve changes through z direction; thus, the right edge of the anode is higher than the left edge. In this study, electrolytes transferred to the machining gap with a constant pressure; therefore, a change in the curve can decrease the electrolyte flow rate. Furthermore, electrolyte accumulation can occur at the left edge, which can cause the DE variation that is seen in Figure 6.20.a.



(a)



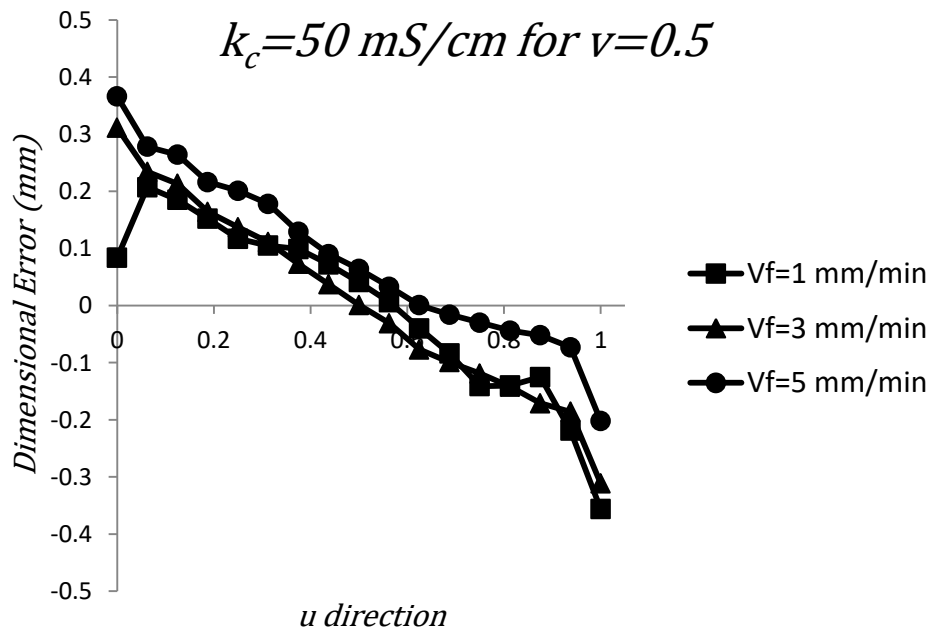
(b)

Figure 6.22 Variation of (a) α and (b) θ angles with u direction for left and right edges

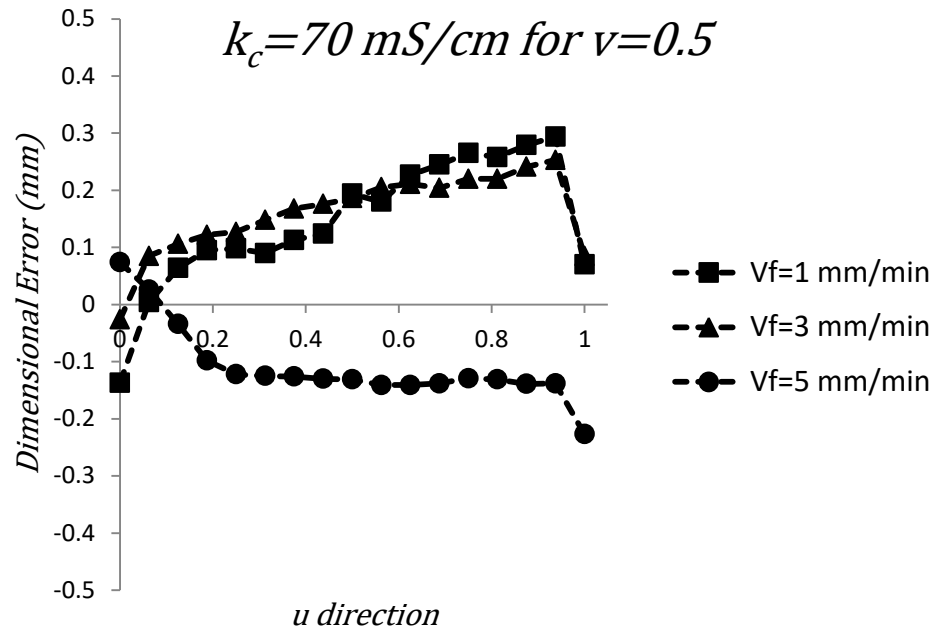
6.3.2 Effect of Feed Rate

The different sides of the electrolyte transfer and the effects of $NaCl$ electrolyte compression occurred in the middle of ($v = 0.5$) the workpiece for all experimental conditions. Figure 6.23.a, b, and c show the variation of DE with u direction for feed rates of $k_c = 50 \text{ mS/cm}$, $k_c = 70 \text{ mS/cm}$, and $k_c = 100 \text{ mS/cm}$, respectively. As can be seen from Figure 6.23.a, the variation of DE changes within $0.207/-0.356 \text{ mm}$, $0.311/-0.311 \text{ mm}$, and $0.366/-0.202 \text{ mm}$ for 1, 3 and 5 mm/min feed rates. All feed rates show similar DE variations along u direction. This can be attributed to the high resistance between the anode and the cathode, which has an effect on electron transfer.

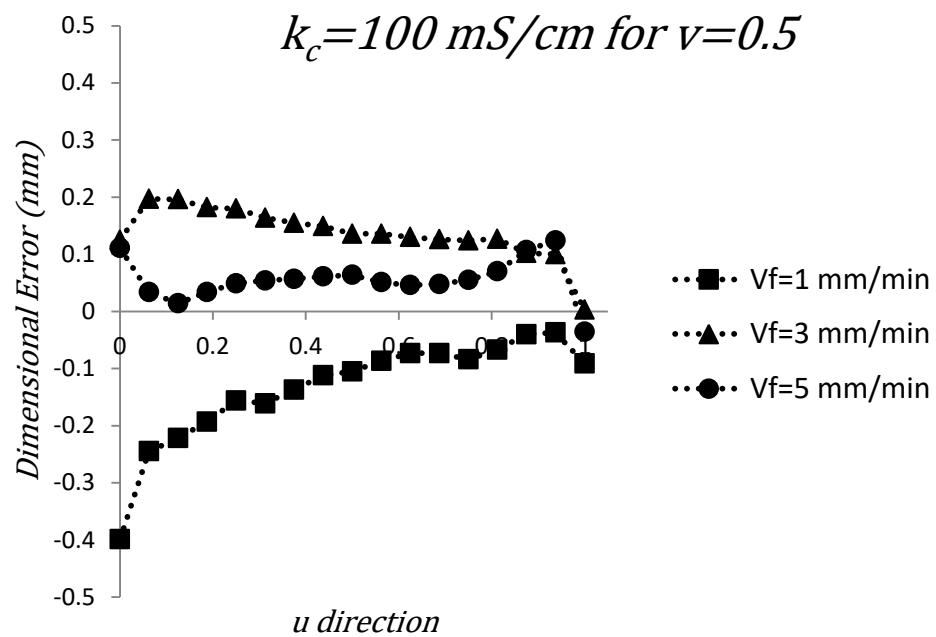
The change of θ is shown in Figure 6.22.b, where electrolyte accumulation after $u = 0.625$ can cause turbulent flow. Therefore, more electron transfer causes over-machining, despite lowest electrical conductivity being used for this experiment. In Figure 6.23.b, as discussed in Section 6.3.1, DE decreases via the right side electrolyte transfer for $V_f = 1 \text{ mm/min}$ and $V_f = 3 \text{ mm/min}$ within $u = 0$ and $u = 0.625$. However, over-machining has been observed for $V_f = 5 \text{ mm/min}$. This can be attributed to the time required to remove the materials from the anode being too short for higher feed rates. Therefore, the short-circuit control mechanism that is discussed in Section 6.2.4 increases the downward-upward movement of the cathode. The anode surface is over-machined due to the increase in the amount of electrolytes with longer machining times. As shown in Figure 6.23.c, with increases in the feed rate and electrical conductivity, less accurate and more accurate DEs have been observed for $V_f = 1 \text{ mm/min}$ and $V_f = 5 \text{ mm/min}$ respectively. As discussed in Section 6.3.1, the most over-machined surfaces have been obtained in Experimental Condition 7 ($V_f = 1 \text{ mm/min}$) via the highest electrical conductivity and initial gap distance. Additionally, the experiments showed that the effect of the electrolyte transfer side on DE is inversely proportional to electrical conductivity.



(a)



(b)



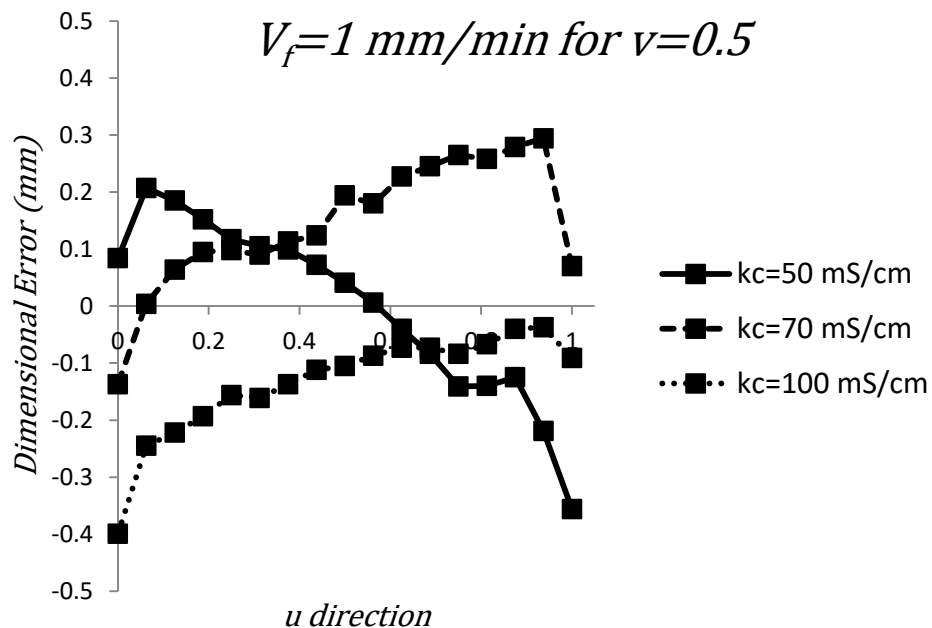
(c)

Figure 6.23 Variation of DE with the u direction for different feed rates (for $v = 0.5$)

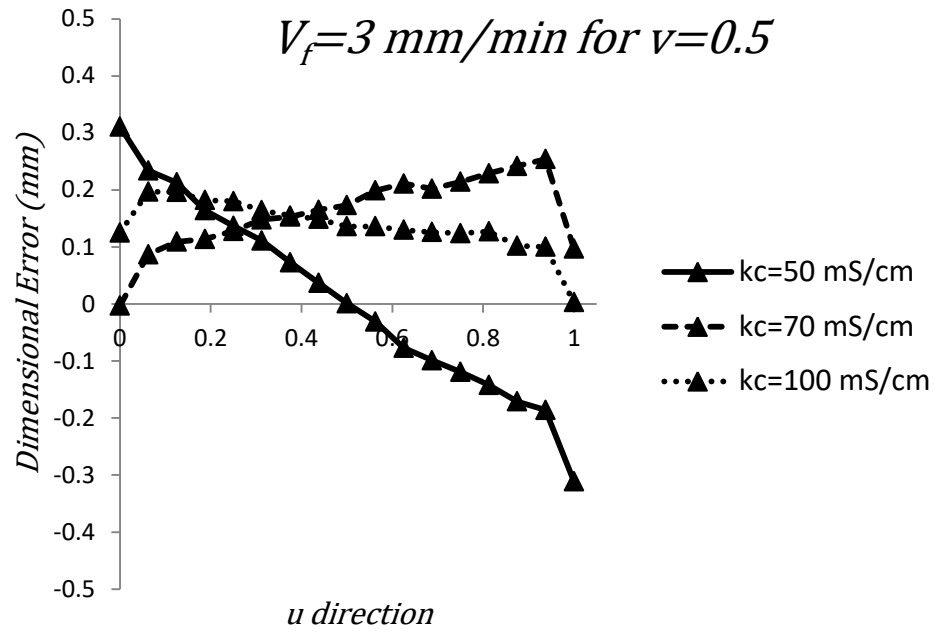
6.3.3 Effect of Electrical Conductivity

Figure 6.24 shows the effect of electrical conductivity on DE for constant feed rates. As can be seen in Figure 6.24.a, due to the geometric shape of the anode (electrolyte transfer side) for $k_c = 50 \text{ mS/cm}$, the DE variation shows differences compared to others. In general, however, it can be seen that DE changes from the non-machined side (positive-signed DE) to the over-machined side (negative-signed DE); this occurs due to

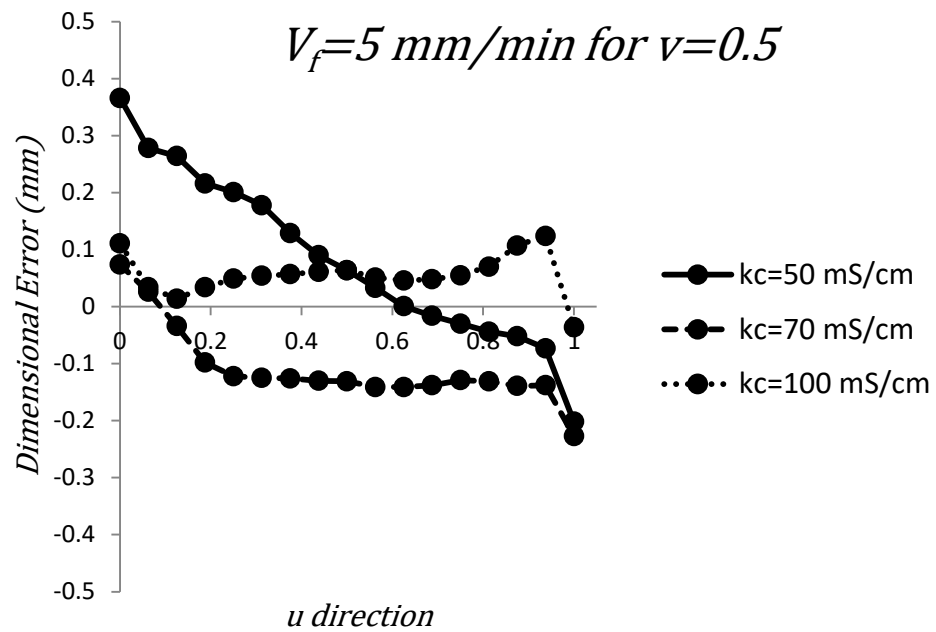
the increase of electrical conductivity in the electrolytes. The differences between the DE for $k_c = 70 \text{ mS/cm}$ and $k_c = 100 \text{ mS/cm}$ can be seen more clearly for $V_f = 1 \text{ mm/min}$, which was the lowest feed rate that was used in the experiments. Figure 6.24.b illustrates the variation of DE along u directions for different electrical conductivities for $V_f = 3 \text{ mm/min}$. As mentioned in Figure 6.24.b, a decrease in DE along u directions occurred for $k_c = 50 \text{ mS/cm}$ and $k_c = 100 \text{ mS/cm}$ due to electrolyte transfer being made from the same side; however, the slope of the DE decrease is lower for the highest conductivity. Additionally, DE differences decrease with the increase of feed rate for $k_c = 70 \text{ mS/cm}$ and $k_c = 100 \text{ mS/cm}$. Variations of DE with u directions for $V_f = 5 \text{ mm/min}$ are shown in Figure 6.24.c. As can be seen in Figure 6.24.c, the highest slope of DE occurred at $k_c = 50 \text{ mS/cm}$, which is the lowest electrical conductivity. An increase in the feed rate can cause the increase of short-circuiting for lower electrical conductivities. Additionally, at higher feed rates, min. DEs have been observed. This can be attributed to high compression speed of anode and cathode via higher feed rates flushing effect can be minimised. Therefore electrolyte flow can be assumed as a solid model that is discussed in Section 3.4.



(a)



(b)



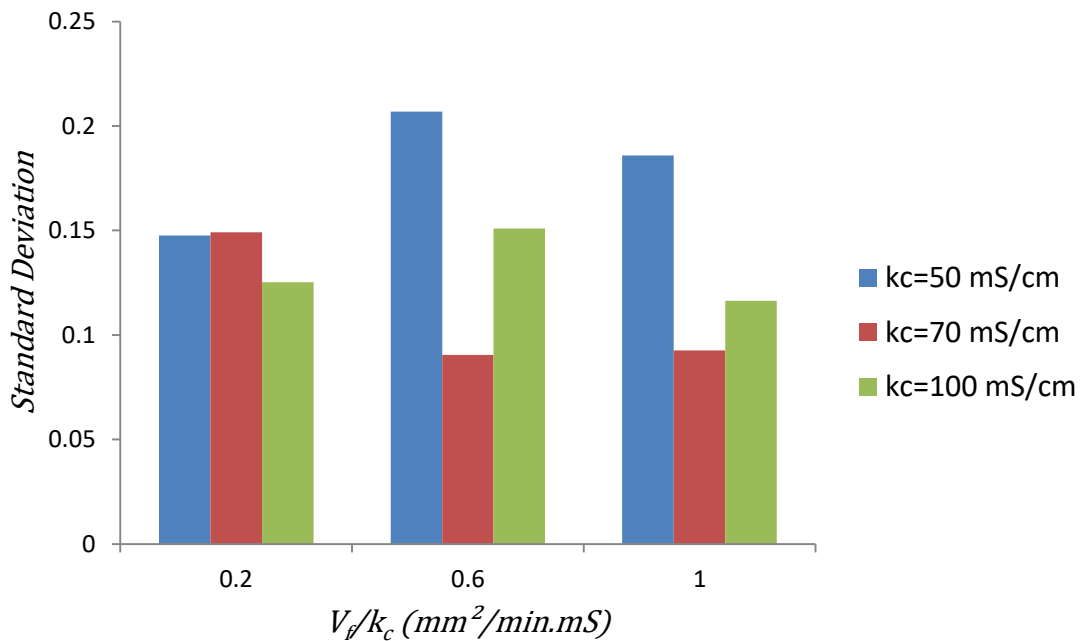
(c)

Figure 6.24 Variation of DE with the u direction for differing electrical conductivity (for $v = 0.5$)

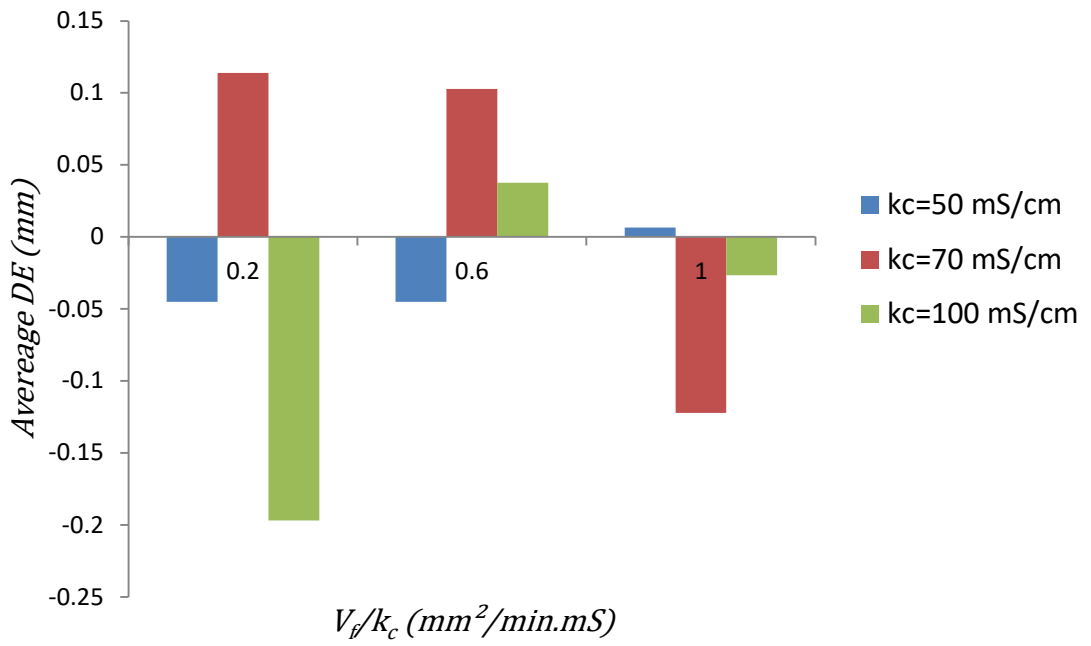
6.3.4 Effect of V_f/k_c

As discussed in Section 3.4, Eq. 3.15 varies with, electrical conductivity of the electrolyte, feed rate, $\cos \theta$ and electrochemical machinability of the workpiece. In order to verify the validity of this mathematical model average DE has been calculated for every Experimental Condition. Therefore $\cos \theta$ admissible as constant additionally;

electrochemical machinability is a specific property of the anode material that is constant for all experimental conditions. Therefore validity of the mathematical model has been evaluated by using V_f/k_c values. Figure 6.25.a and Figure 6.25.b shows the variation of V_f/k_c with average DE and standard deviation respectively. As can be seen from Figure 6.25.a average DE decreases with increase of V_f/k_c value but as a result of irregular machining, in Figure 6.25.b standard deviation increases with V_f/k_c . As a result of that this mathematical model is not suitable for low electrical conductivities. In this study average DE carried in the range of -0.122 to 0.114 for $k_c = 70 \text{ mS/cm}$. Average DE is not change significantly before $V_f/k_c = 0.43$, but after $V_f/k_c = 0.43$ over-machining has been observed. When Figure 6.25.b is investigated 0.15 V_f/k_c values standard deviation decreases significantly. Therefore in the range of $0.45 - 0.7$ V_f/k_c values lower DE and lower standard variation can be obtained. For $k_c = 100 \text{ mS/cm}$ before $V_f/k_c = 0.3$ over machining have been obtained but with the increase of V_f/k_c average DE decreases significantly. Moreover, standard deviation is not change significantly for all V_f/k_c values. As a result of that with higher electrical conductivities machining can be made at similar amount for all control points. Furthermore for higher electrical conductivities and V_f/k_c values implementation of the mathematical model can be improved.



(a)



(b)

Figure 6.25 Variation of V_f/k_c with (a) average DE and (b) standard deviation for various values of electrical conductivity

CHAPTER 7

CONCLUSIONS AND FUTURE WORKS

7.1 Conclusions

In this thesis, a mathematical model was developed for ECM free-form surfaces and an EC machine was designed and constructed in order to perform the verification experiments. To discuss the usability of the EC machine, several experiments were conducted in the developed ECM set-up. In order to verify the mathematical model, nine different cathode surfaces were designed according to various experimental conditions. Additionally, some ECM free-form surface drawbacks were explored and solutions were presented.

The contributions of this thesis to the related literature can be summarised as follows, with the related results and conclusions:

- A developed desktop-size EC machine having micro/macro machining capabilities was presented. With the developed EC machine, electrolyte properties (flow rate, temperature and concentration), feed rate and voltage could be controlled. The experiments on hole drilling were conducted for verification of the EC machine's capabilities and the experiment results were compared with the literature. According to the experiments, the following results for ECM parameters were obtained:
 - Voltage played a significant role in *MRR* and overcut; these occurred in direct proportion to each other.
 - With a lower feed rate and higher voltages, short circuits can be minimised.
 - An increase in feed rate resulted in lower overcut and higher *MRR*.
 - For lower voltages, the initial gap was not an important factor. However, for higher voltages, the initial gap became more important due to the occurrence of an electrical field.

- A mathematical model was developed to design a cathode surface for electrochemical machining of free-form surfaces. The main aim of this work is to obtain an accurate cathode surface that satisfies the Laplace equation, to account for certain boundary conditions that arise when using FEM in ECM. Thus, a computer program was developed for easy and practical usage in solving the encountered equations. A case study was conducted for a free-form surface, and the cathode surface coordinates were obtained. Two different ANSYS Workbench models were used, considering the anode and cathode surfaces. This work was also verified by comparing the results with the literature (considering the linearity situation) and ANSYS Workbench. It was shown that a cathode surface can easily be obtained using zero or near-zero potential points that were obtained from the results of the developed program. The developed theoretical model proposes robust FEM solutions and a best-fit cathode surface; it will lead to machining the correct form of freeform surfaces.
- ECM process solutions for common ECM drawbacks for machining free-form surfaces have been presented. These drawbacks were short-circuiting, cavitation and oxide layer generation.
 - To control short-circuiting, a micro-controller board was used. Using voltage control as dynamic feedback was not a good solution to control short-circuiting for higher feed rates. This can be attributed to poorly distributed electrolyte transition and waste bulk generation through unimplemented machined metal atoms. Therefore, voltage and current were used as dynamic feedback to control short-circuiting. In this control system, current was limited to a constant value that was dedicated via preliminary works.
 - For cavitation, four different pieces of apparatus were designed, tested and simulated using ANSYS software. One of the important parameters that defines cavitation, electrolyte velocity was investigated using simulated results. Simulations showed that velocity distribution for apparatus 4 was better than the others. Apparatus 4, which provided the fluid dynamic conditions, avoided cavitation formation.
 - From the experimental results, a contaminant in the electrolyte caused a black oxide layer to form on the anode (workpiece) surface. Because of this, the electrolyte transfer system was changed from a continuous type

to a discontinuous type. This meant that the electrolyte used for machining was removed from the ECM system. As a result of changing the electrolyte transfer system, the formation of an oxide layer on the workpiece surface was prevented.

- In order to verify the mathematical model, nine different experimental conditions were designed. Feed rate and electrical conductivity were the variables used in experimental conditions. Anode surface measurements were taken using a 3D scanner. Machining accuracy showed differences for all experiments. Therefore, anode surface coordinates converted from $x - y - z$ to the u and v directions.
 - Experiments showed that over-machining (minus signed machining accuracy) occurred at the electrolyte inlet edge. $NaCl$ is a non-sludge electrolyte type that caused over-machining. Furthermore, the initial gap played a part in over-machining. This phenomenon can be prevented by changing the electrolyte type, to a type such as $NaNO_3$.
 - In the middle of gap domain DE behaved similar variation due to be kept at similar values of electrolyte properties when compared the electrolyte inlet and outlet edges of the anode surface.
 - To discuss the effect of parameters (feed rate and electrical conductivity) on the over-machined side, experimental conditions were investigated in two main groups. Due to change of anode geometry DE variation showed a decrease and increase for right and left edges of the anode respectively.
 - Experiments showed that over-machining associated with not only feed rate and electrolyte conductivity but also machining time, electrolyte amount and short-circuiting between the anode and cathode.
 - Additionally, for $V_f = 5 \text{ mm/min}$ and $k_c = 100 \text{ mS/cm}$, the mathematical model gave best results. According to the mathematical model, the electrolyte between the anode and the cathode was accepted as a shape; due to this, at higher feed rates this could be obtained.
- Feed rate (V_f), electrochemical machinability of anode material (k_v), electrical conductivity of the electrolyte (k_c) and the angle between the movement direction of the cathode and normal to the anode control point (θ) are the most

effective parameters for cathode design that is discussed in Chapter 3. k_v and θ values are the constant values that associated with workpiece material and anode geometry. Therefore V_f/k_c criteria are used to dedicate the validity of this mathematical model.

- It is found from the experimental works that with increase of electrolyte conductivity accuracy of the mathematical model increases.
- For lower electrical conductivity of the electrolyte better average DE have been observed but standard deviation increases with the increase of V_f/k_c .
- This mathematical model allows higher dimensional accuracies for particular value of V_f/k_c for $k_c = 70 \text{ mS/cm}$ and increase of electrolyte conductivity and V_f/k_c best dimensional accuracies have been observed.

7.2 Future Works

The following is recommended for future studies in this area:

- In this study, via the complexity of the freeform surface geometry surface roughness can not be measured with using conventional surface measurement devices. In literature some related works to measure the surface properties of freeform surfaces can be found [107, 108]. In that sense, effect of ECM parameters on surface roughness for freeform surfaces can be studied and the results can be compared to the other machining processes such as EDM, milling.
- Application of the mathematical model for hard-to-machine materials, such as Ti-6Al-4V and Inconel 718 must be verified.
- Residual stress measurements will be done in future works.
- In this study, electrical conductivity of the electrolyte was used for a numerical solution to the mathematical model. The effect of the electrolyte type ($NaNO_3$, $NaNO_3 + HCl$, etc.) on the accuracy of the mathematical model, given the same electrical conductivity, must be investigated.
- The effect of machining depth and voltage on the mathematical model must be investigated.
- The experimental results showed that the electrolyte filtering unit directly affects formation of an oxide layer on the anode surface. Therefore, the filtering system must be investigated and developed in detail.

- Experiments were conducted using the same electrolyte flow rate in this study. The effects of changing flow rate (lower or higher) on the accuracy of the mathematical model should be investigated.
- In the literature, high machining accuracy has been obtained on drilling operations by applying short voltage pulses. The mathematical model that is presented in this study can be adapted to voltage pulse operations for ECM freeform surfaces.
- Short-circuit control was developed by limiting the current. This was obtained by trial and error. A mathematical model can be developed to predict the current variation with time, so that unexpected current variations can be avoided automatically for different ECM parameters.
- EMM of freeform surfaces must be investigated.
- Adaptation of ECM with robotic machining can be investigated.
- A hybrid machining process (ECM + additive manufacturing) can be designed and developed for freeform surface machining applications.

REFERENCES

- [1] Mallick, U. (2009). Estimation of MRR Using U-Shape Electrode in Electrochemical Machining. M.Sc thesis, National Institute of Technology Rourkela.
- [2] McGeough, J. A. (1988), *Advanced Methods of Machining*, Chapman and Hall: Springer.
- [3] Kozak, J. (2004), *Electrochemical machining*.
- [4] Klocke, F., Klink, A., Veselovac, D., Aspinwall, D. K., Soo, S. L., Schmidt, M., Schilp, J., Levy, G., Kruth, J.P., (2014). Turbomachinery component manufacture by application of electrochemical, electro-physical and photonic processes, *CIRP Annals - Manufacturing Technology*, **63**, 703–726.
- [5] Klocke, F., Welling, D., Dieckmann, J., Veselovac, D., Perez, R., (2012). Developments in Wire-EDM for the Manufacturing of Fir Tree Slots in Turbine Discs Made of Inconel 718, *Key Engineering Materials*, **504**, 1177–1182.
- [6] Rajurkar, K.P., Levy, G., Malshe, A., Sundaram, M.M., McGeough, A., Hu, X., Resnick, R., De Silva, A., (2006). Micro and Nano Machining by Electro-Physical and Chemical Processes, *CIRP Annals – Manufacturing Technology*, **55**, 643–666.
- [7] F. Klocke, F., M. Zeis, M., Klink, A., Veselovac, D. (2013). Technological and economical comparison of roughing strategies via milling, sinking-EDM, wire-EDM and ECM for titanium- and nickel-based blanks, *CIRP Journal of Manufacturing Science and Technology*, **6**, 198-203.
- [8] Rajurkar K. P., Zhu D., McGeough J.A., Kozak J., Silva De A., (1999) New Developments in Electro-Chemical Machining, *CIRP Annals - Manufacturing Technology*, **48**, (2), 567-579.
- [9] Tonshoff H. K., Egger R., and Klocke F., (1996), Environmental and Safety Aspects of Electrophysical and Electrochemical Processes, *CIRP Annals - Manufacturing Technology*, **45** (2), 1-15.
- [10] Datta M. and Romankiw L. T., (1989), Application of Chemical and Electrochemical Micromachining in the Electronics Industry, *Journal of the Electrochemical Society*, **136**, (6), 285c-292c.
- [11] Amalnik M. S. and McGeough J. A., (1996), Intelligent Concurrent Manufacturability Evaluation of Design for Electrochemical Machining, *Journal of Materials Processing Technology*, **61**, 130-139.
- [12] Goggins G. J., (1987), Electrolytic Machining and Sizing of Firing Chambers, *SME Technical Paper*, MR87-147.
- [13] Masuzawa T., Kuo C.L. M. and Fujino I.I.S., (1994), A Combined Electrical Machining Process for Micronozzle Fabrication, *Annals of the CIRP*, **43**, 189-192
- [14] Maehata H. and Kamada H., (1985), Studies on the Electrolytic-Abrasive Mirror Finishing (II), *Bulletin of the Japan Society of Precision Engineering*, **19**, 131-132.

- [15] Masuzawa T., and Kimura M., (1991), Electrochemical Surface Finishing of Tungsten Carbide Alloy, *Annals of the CIRP*, **40**, 199-202.
- [16] Masuzawa T., and Takawashi T., (1998), Recent Trends in EDM/ECM Technologies in Japan, *Proceedings of the ISEM-12*: 1-15.
- [17] Tam S. C., Loh N. H. and Miyazawa S., (1989), ECM-Abrasive Polishing of Metals, *Int. J. Prod. Res.*, **27**, 1757-1768.
- [18] Koppern ECM, (1998), Electrochemical Machining.
- [19] Teleflex Incorporated Group, (1998), Leading the Way with Service Material and Technology.
- [20] Anon, (1986). Rolls-Royce Automates Jet Engine Compressor Blade Line, *Machine and Tool Blue Book*, **81**, (2), 62-65.
- [21] AEG-ELOTHERM, (1998), ECM Technology.
- [22] Goyer, A. and Moehring, S., (1988), Electrochemical Machining, Little Known, But Very Useful, *Modern Machine Shop*, **4**, 63-69.
- [23] Raycom & Amchem, (1998), Electrochemical Machining.
- [24] Risko D. G., (1990), Electrochemical Machining Innovations Solution for Higher Productivity, *SME Advanced Manufacturing Technology III*, MR90-244.
- [25] Mahdavinejad R., Hatami M., (2008), On the Application of Electrochemical Machining for Inner Surface Polishing of Gun Barrel Chamber, *Journal of Materials Processing Technology*, **202**, 307-315.
- [26] Youssef H. A., El-Hofy H. (2008), Machining Technology Machine Tools and Operations, CRC Press.
- [27] Lievestro L. T. (1989), ASM Metal Handbook, Electrochemical Machining.
- [28] Lawrence P., (1981), Computer Aided Design for ECM Electrodes, *Int. J. Mach. Tool Des. Res.*, **21**, 379-385.
- [29] Nilson R. H. and Tsuei Y. G., (1976), Free Boundary Problem for the Laplace Equation to ECM Tool Design, *ASME J. of Appl. Mech.*, **98**, 54-58.
- [30] Tipton, H., (1968), The Determination of Tool Shape for ECM, *Mach. and Prod. Eng.*, **14**, 325-328.
- [31] Tsuei Y. G. and Nilson H., (1977), Effects of Variable Electrolyte Conductivity on Side Gap Geometry in ECM, *Mach. Tool Des. & Research*, **17**, 169- 176.
- [32] Das S., and Mitra A. K., (1992), Use of Boundary Element Method for the Determination of Tool Shape in Electrochemical Machining, *Int. J. for Numerical Methods in Engineering*, **35**, 1045-1054.
- [33] Hardisty H., Mileham A. R. and Shirvarni H., (1993), A Finite Element Simulation of the Electrochemical Machining Process, *Annals of the CIRP*, **421**, 201-204.
- [34] Jain V. K., and Rajurkar K. P., (1991), An Integrated Approach for Tool Design in ECM, *Precision Engineering*, **13**, (2), 111-124.
- [35] Narayanan H., Hinduja, S., Noble F., (1986), Design of Tools for ECM by the Boundary Element, *Proc. Instn. Mech. Engrs.*, **200**, (C3), 195-205.

- [36] Nied H. A. and Lamphere M. S., (1995), Electrochemical Airfoil Machining Process Model, *Presented at the International Gas Turbine & Aeroengine Congress and Exposition Houston, Texas, June 5-8*.
- [37] Nied H. and Lamphere M. S., (1995), Electrochemical Machining Simulation Using the Boundary Element Method, *Proceedings of the ISEM-11*, 473-490.
- [38] Reddy M. S., Jain V. K., and Lal G. K., (1988), Tool Design for ECM: Correction Factor Method, *ASME J. of Eng. for Industry*, **10**, 111-118.
- [39] Zhou Y. and Derby J. J., (1995), The Cathode Design Problem in Electrochemical Machining, *Chemical Engineering Science*, **50**, 2679-2689.
- [40] Zhu D. and Yu C. Y., (1992), Investigation on the Design of Tool Shape in Electrochemical Machining, *ASME PED*, **58**, 181-190.
- [41] Hocheng H., Sun Y.H., Lin S.C., Kao P.S. (2003), A material removal analysis of electrochemical machining using flat-end cathode, *Journal of Materials Processing Technology*, **140**, 264-268.
- [42] Zhiyong L. and Hua J., (2010), The Effects of Normal Gap Distribution on Cathode Design of Aero-engine blades in Electrochemical Machining, *Advanced Materials Research*, **97**, 3583-3586.
- [43] Kozak J., Budzynski A. F., Domanowski P., (1998), Computer simulation electrochemical shaping (ECM-CNC) using a universal tool electrode, *Journal of Materials Processing Technology*, **76**, 161-164.
- [44] Purcar M., Bortels L., Bossche B. V., DeconinckJ., (2004), 3D electrochemical machining computer simulations, *Journal of Materials Processing Technology*, **149**, 472-478.
- [45] Bortels L., Purcar M., Bossche B. V., DeconinckJ., (2004), A user-friendly simulation software tool for 3D ECM, *Journal of Materials Processing Technology*, **149**, 486-492.
- [46] Pattavanitch J., Hinduja S., Atkinson J., (2010), Modelling of the electrochemical machining process by the boundary element method, *CIRP Annals - Manufacturing Technology*, **59**, 243-246.
- [47] Zhiyong L., Hua J., (2009), Machining Accuracy Prediction of Aero-engine Blade in Electrochemical Machining Based on BP Neural Network, *Proceedings of the 2009 International Workshop on Information Security and Application*, China, November 21 - 22.
- [48] Sun C., Zhu D., Li Z., Wang L., (2006), Application of FEM to tool design for electrochemical machining freeform surface, *Finite Elements in Analysis and Design*, **43**, 168 - 172.
- [49] Zhiyong L., Zongwei N., (2007), Convergence Analysis of the Numerical Solution for Cathode Design of Aero-engine Blades in Electrochemical Machining, *Chinese Journal of Aeronautics*, **20**, 570-576.
- [50] Wang M.H., Zhu D., (2009), Simulation of fabrication for gas turbine blade turbulated cooling hole in ECM based on FEM, *Journal of Materials Processing Technology*, **209**, 1747-1751.

- [51] Bhattacharyya, B. and Munda, J., (2003), Experimental investigation into electrochemical micromachining (EMM) process, *Journal of Materials Processing Technology*, **140**, 287-291.
- [52] Li, Z. and Yuan, G., (2008). Experimental Investigation of Micro-holes in Electrochemical Machining Using Pulse Current, *Proceedings of the 3rd IEEE Int. Conf. on Nano/Micro Engineered and Molecular Systems*, China, 151-154.
- [53] Vanderauwera, W., Vanloffelt, M., Perez, R., Lauwersa B., (2013), Investigation on the performance of macro electrochemical milling, *The Seventeenth CIRP Conference on Electro Physical and Chemical Machining (ISEM)*, 356-361.
- [54] Thanigaivelan, R., Arunachalam, R., M., Karthikeyan, B., Loganathan, P., (2013), Electrochemical micromachining of stainless steel with acidified sodium nitrate electrolyte, *The Seventeenth CIRP Conference on Electro Physical and Chemical Machining (ISEM)*, 352-356.
- [55] Malapati, M. and Bhattacharyya B. (2011), Investigation into Electrochemical Micromachining Process during Micro-Channel Generation, *Materials and Manufacturing Processes*, **26**, 1019-1027.
- [56] Neto, J., Silva, E., Silva, M. (2006), Intervening variables in electrochemical machining, *Journal of Materials Processing Technology*, **179**, 92-96.
- [57] Mukherjee, S., K., Kumar, S., Srivastava, P., K., (2005), Effect of Over Voltage on Material Removal Rate During Electrochemical Machining, *Tamkang Journal of Science and Engineering*, **8**, 23-28.
- [58] Costa, H. L. and Hutchings, I. M. (2009). Development of a maskless electrochemical texturing method, *Journal of materials processing technology*, **209**, 3869–3878.
- [59] Tehrani, A., F. and Atkinson, J. (2000). Overcut in pulsed electrochemical grinding, *Journal of Engineering Manufacture*, **24**, 259-269.
- [60] Hourng, L.W., and Chang, C.S. (1993). Numerical simulation of electrochemical drilling, *Journal of Applied Electrochemistry*, **23**, 316–321.
- [61] Thorpe, J.F. and Zerkle, R. D., (1971). *Fundamentals of Electrochemical Machining*, Princeton: NJ.
- [62] Senthilkumar, C., Ganesan G. and Karthikeyan R. (2009). Study of electrochemical machining characteristics of Al/SiC_p composites, *International Journal of Advanced Manufacturing Technology*, **43**, 256-263.
- [63] Krishnaiahchetty, OV., Radhakrishnan, V. (1981). A study on the influence of grain size in electrochemical machining. *Intertanational Journal of Machine Tool Design and Research*, **21**, 57–69.
- [64] Bhattacharyya, B., Munda, J. and Malapati, M. (2004). Advancement in Electrochemical Micro- Machining, *International Journal of Machine Tools & Manufacture*, **44**, 1577- 1589.
- [65] Sun, J. J., Taylor, E. J., Gebhart, L. E., Renz, R. P. and Zhou, C. D. (1999). Final Finishing of a Metal Surface by an Electrochemical Machining (Ecm) Process, *AESF Annual Technical Conference*, incinnati, OH, USA, 189-199.
- [66] Sun, C.H., Zhu, D. and Li, Z.Y. (2004). Prediction of the Workpiece Accuracy During the Electrochemical Machining Based on Bp Neural Network, *Huanan Ligong*

Daxue Xuebao/Journal of South China University of Technology (Natural Science), **32**, 24-27.

[67] Onel, S. (2014). Investigation and Application of Automatic Controlled Electrochemical Machining (ECM), *Journal of the Faculty of Engineering and Architecture of Gazi University*, **29**, 1-8.

[68] Mahdavinejad, R. A., and Hatami, M.R. (2008). Ecm Rifling Tool Design and Manufacturing, *Iranian Journal of Science & Technology, Transaction B, Engineering*, **32**, 341-352.

[69] Mahdavinejad, R. A., and Hatami, M.R. (2008). On the application of electrochemical machining for inner surface polishing of gun barrel chamber, *Journal of Materials Processing Technology*, **202**, 307–315.

[70] Kim, B.H., Na, C.W., Lee, Y.S., Choi, D. K., Chu, C. N. (2005). Micro Electrochemical Machining of 3D Micro Structure Using Dilute Sulfuric Acid, *CIRP Annals*, **1**, 191-194.

[71] Bilgi, S. D., Jain, V.K., Shekhar, R. and Mehrotra, S. (2004). Electrochemical Deep Hole Drilling In Super Alloy For Turbine Application, *Journal of Materials Processing Technology*, **149**, 445–452.

[72] Tang, L. and Guo, Y. F. (2013). Experimental Study of Special Purpose Stainless Steel on Electrochemical Machining of Electrolyte Composition, *Materials and Manufacturing Processes*, **28**, 457-462.

[73] Raja, K., Ravikumar, R. (2016). A Review on Electrochemical Machining Processes, *International Journal of Applied Engineering Research*, **11**, 2354-2355.

[74] Hourng, L.W., and Chang, C.S. (1994). Numerical simulation of two-dimensional fluid flow in electrochemical drilling, *Journal of Applied Electrochemistry*, **24**, 1170–1175.

[75] El-Dardiry, M.A., Asfoor, M.A., Osman, H.M. (1984). Experimental investigation into the performance of electrochemical machining processes. Part-I. Parameters affecting productivity characteristics, *Proceedings of the Fifth International Conference on Production Engineering*, Tokyo, 375–381.

[76] Rao, S.V.R., Mishra, P.K., (1984). Hole drilling by electrojet, *Proceedings of the Fifth International Conference on Production Engineering*, Tokyo, 455–458.

[77] El-Dardiry, M.A., Asfoor, M.A., Osman, H.M. (1984). Experimental investigation into the performance of electrochemical machining processes. Part-II. Parameters affecting the surface quality, *Proceedings of the Fifth International Conference on Production Engineering*, Tokyo, 382–388.

[78] Sastry, D.S., (1999). Electro-stream drilling of high-speed steel, *M. Tech Thesis*, Indian Institute of Technology, Kanpur.

[79] Singh, R. (1981). Investigation on electrochemical drilling with rotating electrode, *ME Dissertation*, University of Roorkee, India.

[80] Bhattacharyya, B., Malapati, M., Munda J. (2005). Experimental study on electrochemical micromachining, *Journal of Materials Processing Technology*, **169**, 485–492.

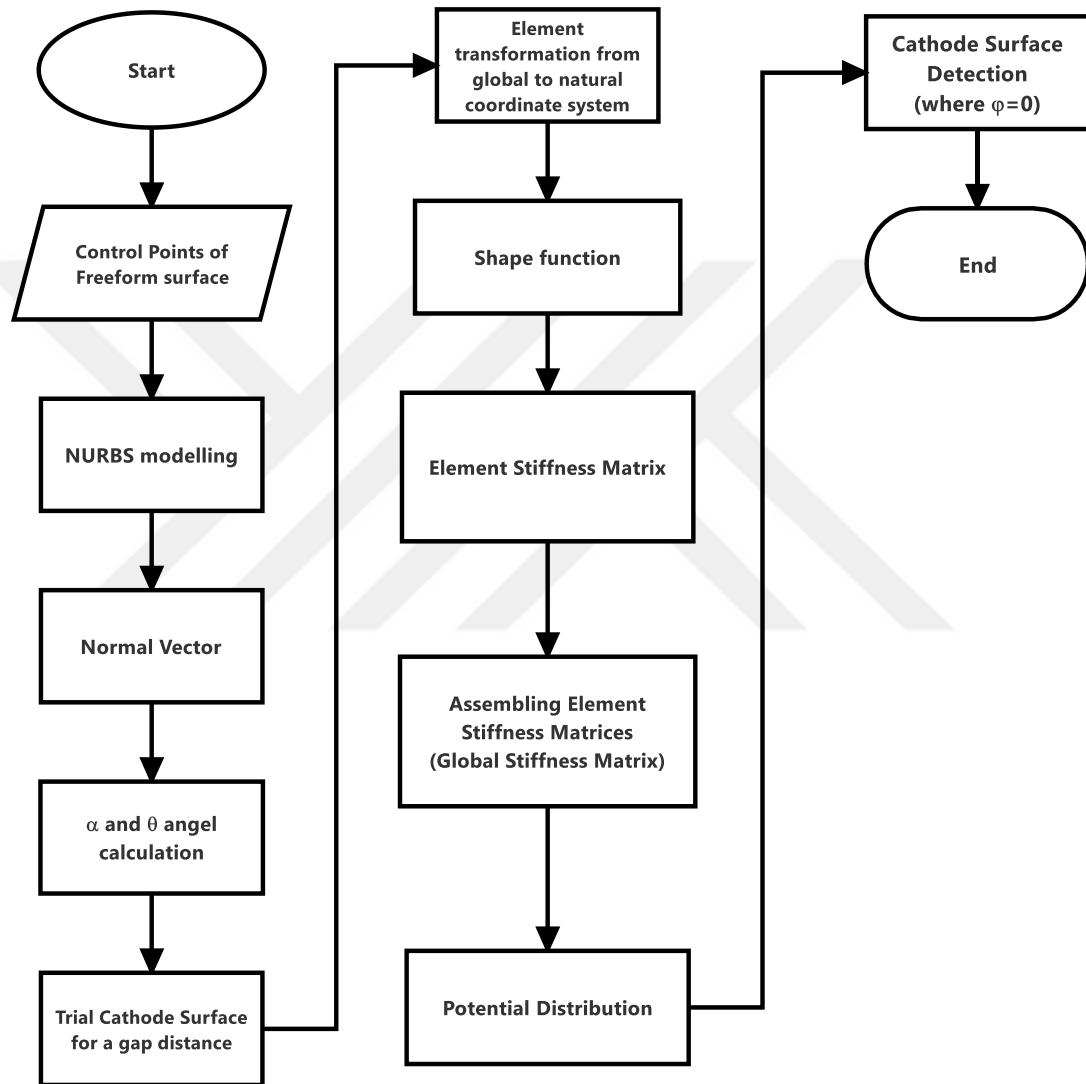
- [81] Golnabi, H., Matloob, M. R., Bahar, M., Sharifian M. (2009). Investigation of electrical conductivity of different water liquids and electrolyte solutions, *Iranian Physical Journal*, **3**, 24-28.
- [82] Mithu, M. A. H., Fantoni, G., Ciampi, J., Santochi, M. (2012). On how tool geometry, applied frequency and machining parameters influence electrochemical microdrilling, *CIRP Journal of Manufacturing Science and Technology*, **5**, 202-213.
- [83] Fan, Z. W.; Hourng, L.W. (2009). The analysis and investigation on the microelectrode fabrication by electrochemical machining. *International Journal of Machine Tools & Manufacture*, **49**, 659-666.
- [84] Labib, A. W., Keasberry, V. J., Atkinson, J., Fros, H. W. (2011). Towards next generation electrochemical machining controllers: A fuzzy logic control approach to ECM. *Expert Systems with Applications*, **38**, 7486–7493.
- [85] Ghoshal, B., Bhattacharyya, B. (2013). Influence of vibration on micro-tool fabrication by electrochemical machining, *International Journal of Machine Tools & Manufacture*, **64**, 49–59.
- [86] Bannard, J. (1977). Electrochemical machining, *Journal of Applied Electrochemistry*, **7**, 1–29.
- [87] Kozak, J. (1976). Mathematical models for computer simulation of electrochemical machining process., *Journal of Material Processing Technology*, **76** , 170–175.
- [88] Sato, T. (1970). *Electrochemical Machining and Chemical Machining*. Asakura Publishing, Japan.
- [89] Koyano, T., Kunieda, M. (2013). Micro electrochemical machining using electrostatic induction feeding method. *CIRP Annals - Manufacturing Technology*, **62**, 175–178.
- [90] Davydov, A. D., Volgin, V. M., Lyubimov, V. V. (2004). Electrochemical machining of metals: Fundamentals of electrochemical shaping, *Russian Journal of Electrochemistry*, **40**, 1230–1265.
- [91] Mao, K.W. (1971). ECM study in a closed cell system, *Journal of The Electrochemical Society*, **118**, 1870–1876.
- [92] Lohrengel, M. M., Klüppel, I., Rosenkranz, C., Bettermann, H., Schultze, J. W. (2003). Microscopic investigations of electrochemical machining of Fe in NaNO₃, *Electrochimica Acta*, **48**, 3203-3211.
- [93] Rogers, D. F. (2001). *An Introduction to NURBS with Historical Perspective*. 1st Edition. Morgan Academic Press: Kaufmann Publishers.
- [94] Piegl, L. A., Tiller, W. (1997). *The NURBS book*. 2nd Edition. Springer Press: Germany.
- [95] Domanowski, P. and Kozak, J. (2001). Inverse problems of shaping by electrochemical generating machining. *Journal of Materials Processing Technology*, **109**, 347–353.
- [96] Rao, S. S. (2011). *The Finite Element Method in Engineering*. Elsevier:Butterworth Heinemann Publicatios.
- [97] Gu, G. G. and Gennert, M. A. (1991). Boundary Element Methods for Solving Poisson Equations in Computer Vision Problems, *IEEE Computer Society Conference*, Maui, HI.

- [98] Logan, D. L. (2007) A First Course in the Finite Element Method. 4th edition, Nelson Press, Canada.
- [99] Li, Z. and Diu, Z. (2006). Numerical Solution for Cathode Design of Aero-engine Blades in Electrochemical Machining, *International Conference on Mechatronics and Automation*, China.
- [100] López de Lacalle, L.N. and Lamikiz, A., (2009), Machine Tools for High Performance Machining, Verlag London: Springer Press.
- [101] Klocke, F., Zeis, M., Klink, A., Veselovac, D. (2013). Experimental research on the electrochemical machining of modern titanium- and nickel-based alloys for aero engine components, *Procedia CIRP*, **6**, 369-373.
- [102] Yilmaz, O. (2006). Repair of complex geometry components and free-form surfaces. PhD Thesis, University of Nottingham.
- [103] Banks, C. and Compton, R. G. (2003). Voltammetric exploration and applications of ultrasonic cavitation, *ChemPhysChem*, **4**, 169–178.
- [104] Suslick, K.S., Didenko, Y., Fang, M. M., Hyeon, T., Kolbeck, K. J., McNamara, W. B., Mdlalen, M. M., Wong, M. (1999). Acoustic cavitation and its chemical consequences, *Philosophical Transactions of the Royal Society A*, **357**, 335–35.
- [105] Lohrengel, M. M. (2006). Pulsed Electrochemical Machining of Iron in NaNO_3 : Fundamentals and New Aspects, *Materials and Manufacturing Processes*, **20**, 1-8.
- [106] Datta, M. and Landolt, D. (1979). On the role of mass transport in high rate dissolution of iron and nickel in ECM electrolytes-I: chloride solutions, *Electrochimica Acta*, **25**, 1255-1262.
- [107] Cheung, C. F., Kong, L. B. and Ren, M. J. (2010). Measurement and characterization of ultra-precision freeform surfaces using an intrinsic surface feature-based method, *Measurement Science and Technology*, **21**, 109-115.
- [108] Thammarat, S., (2017). 3D Freeform Surface Measurement on Coordinate Measuring Machine Using Photometric Stereo Method. PhD Thesis, Brunel University.

APPENDIX



Appendix A: Flow Chart of Developed Computer Program



Appendix B: Developed Mathematica Program

```

umax = 9; vmax = 2; Δb = 5; layer = 10;
Do[Dizin[i + 1] = Array[V[i], umax + 1, 0], {i, 0, vmax}]
PTS = Array[Dizin, vmax + 1, 1];
hazır = BSplineFunction[PTS];
vektörler = hazır[Knots];
dereceler = hazır[Degree];
degree1 = dereceler[[2]];
degree2 = dereceler[[1]];
knot = vektörler[[2]];
knots = vektörler[[1]];
nodenum = (umax + 1) * (vmax + 1);
elnum = umax * vmax;
Do[wij = 1, {i, 0, umax}, {j, 0, vmax}]
  Do[Ni,4 = PiecewiseExpand[BSplineBasis[{degree1, knot}, i, u], 0 ≤ u
    ≤ 1], {i, 0, umax}]
  Do[Ki,4 = PiecewiseExpand[BSplineBasis[{degree2, knots}, i, v], 0 ≤ v
    ≤ 1], {i, 0, vmax}]
Suv =  $\left( \sum_{i=0}^{vmax} \sum_{j=0}^{umax} K_{i,4} N_{j,4} w_{j,i} V[i][j] \right) / \left( \sum_{i=0}^{vmax} \sum_{j=0}^{umax} K_{i,4} N_{j,4} w_{j,i} \right)$ ;
thick = Δb / (layer - 1); Su = D[Suv, u]; Sv = D[Suv, v];
unit = Norm[Cross[Su, Sv]];
Do[u[i] = i / umax, {i, 0, umax}]
Do[v[i] = (i - 1) / vmax, {i, 0, vmax + 1}]
u[umax/2] = 0.49999;
ncalc = ((Cross[Su, Sv] / unit));

```


$$\text{Do}[n[(v_{\max} + 1) * i] + j]$$

$$= (\text{nCalc} /. \{u \rightarrow u[i], v \rightarrow v[j]\}), \{j, 1, (v_{\max} + 1)\}, \{i, 0, u_{\max}\}]$$

$$\text{Do}[\theta[i] = \text{ArcCos}[-n[i][[3]]], \{i, 1, \text{nodenum}\}]$$

$$\text{Do}[\alpha[i] = \text{ArcTan}[n[i][[1]]/n[i][[2]]], \{i, 1, \text{nodenum}\}]$$

$$\text{Do}[x[(v_{\max} + 1)i + j] = V[j - 1][i][[1]], \{j, 1, (v_{\max} + 1)\}, \{i, 0, u_{\max}\}]$$

$$\text{Do}[y[(v_{\max} + 1)i + j] = V[j - 1][i][[2]], \{j, 1, (v_{\max} + 1)\}, \{i, 0, u_{\max}\}]$$

$$\text{Do}[z[(v_{\max} + 1)i + j] = V[j - 1][i][[3]], \{j, 1, (v_{\max} + 1)\}, \{i, 0, u_{\max}\}]$$

$$\text{Do}[x[i + \text{nodenum}] = x[i] - \text{thick} * \text{Sin}[\theta[i]]\text{Sin}[\alpha[i]], \{i, 1, \text{nodenum}\}]$$

$$\text{Do}[y[i + \text{nodenum}] = y[i] - \text{thick} * \text{Sin}[\theta[i]]\text{Cos}[\alpha[i]], \{i, 1, \text{nodenum}\}]$$

$$\text{Do}[z[i + \text{nodenum}] = z[i] + \text{thick}, \{i, 1, \text{nodenum}\}]$$

$$\text{Do}[x[i + \text{nodenum}]$$

$$= x[i] - \text{thick}$$

$$* \text{Sin}[\theta[j]]\text{Sin}[\alpha[j]], \{k, 1, \text{layer} - 2\}, \{i, k * \text{nodenum} + 1, (k + 1)$$

$$* \text{nodenum}\}, \{j = i - k * \text{nodenum}\}]$$

$$\text{Do}[y[i + \text{nodenum}]$$

$$= y[i] - \text{thick}$$

$$* \text{Sin}[\theta[j]]\text{Cos}[\alpha[j]], \{k, 1, \text{layer} - 2\}, \{i, k * \text{nodenum} + 1, (k + 1)$$

$$* \text{nodenum}\}, \{j = i - k * \text{nodenum}\}]$$

$$\text{Do}[z[i + \text{nodenum}]$$

$$= z[i] + \text{thick}, \{k, 1, \text{layer} - 2\}, \{i, k * \text{nodenum} + 1, (k + 1)$$

$$* \text{nodenum}\}]$$

$$H[1] = 1/8 (1 - \xi)(1 - \eta)(1 - \mu);$$

$$H[2] = 1/8 (1 + \xi)(1 - \eta)(1 - \mu);$$

$$H[3] = 1/8 (1 + \xi)(1 + \eta)(1 - \mu);$$

$$H[4] = 1/8 (1 - \xi)(1 + \eta)(1 - \mu);$$

$$H[5] = 1/8 (1 - \xi)(1 - \eta)(1 + \mu);$$

$$H[6] = 1/8 (1 + \xi)(1 - \eta)(1 + \mu);$$

$$H[7] = 1/8 (1 + \xi)(1 + \eta)(1 + \mu);$$

$$H[8] = 1/8 (1 - \xi)(1 + \eta)(1 + \mu);$$

$$\begin{aligned}
& \text{Do} \left[X[v_{\max} * i + k + (\text{elnum} * j)] \right. \\
& \quad = \text{Simplify} \left[H[1]x[(v_{\max} + 1) * i + k + (\text{nodenum} * j)] \right. \\
& \quad + H[2]x[(v_{\max} + 1) * i + (k + 1) + (\text{nodenum} * j)] \\
& \quad + H[3]x[(v_{\max} + 1) * i + (k + (v_{\max} + 2)) + (\text{nodenum} * j)] \\
& \quad + H[4]x[(v_{\max} + 1) * i + (k + (v_{\max} + 1)) + (\text{nodenum} * j)] \\
& \quad + H[5]x[(v_{\max} + 1) * i + (\text{nodenum} + k) + (\text{nodenum} * j)] \\
& \quad + H[6]x[(v_{\max} + 1) * i + (\text{nodenum} + k + 1) + (\text{nodenum} * j)] \\
& \quad + H[7]x[(v_{\max} + 1) * i + (\text{nodenum} + k + (v_{\max} + 2)) \\
& \quad + (\text{nodenum} * j)] \\
& \quad + H[8]x[(v_{\max} + 1) * i + (\text{nodenum} + k + (v_{\max} + 1)) \\
& \quad + (\text{nodenum} * j)] \left. \right], \{k, 1, v_{\max}\}, \{j, 0, \text{layer} - 1\}, \{i, 0, (u_{\max} - 1)\} \left. \right]
\end{aligned}$$

$$\begin{aligned}
& \text{Do} \left[Y[v_{\max} * i + k + (\text{elnum} * j)] \right. \\
& \quad = \text{Simplify} \left[H[1]y[(v_{\max} + 1) * i + k + (\text{nodenum} * j)] \right. \\
& \quad + H[2]y[(v_{\max} + 1) * i + (k + 1) + (\text{nodenum} * j)] \\
& \quad + H[3]y[(v_{\max} + 1) * i + (k + (v_{\max} + 2)) + (\text{nodenum} * j)] \\
& \quad + H[4]y[(v_{\max} + 1) * i + (k + (v_{\max} + 1)) + (\text{nodenum} * j)] \\
& \quad + H[5]y[(v_{\max} + 1) * i + (\text{nodenum} + k) + (\text{nodenum} * j)] \\
& \quad + H[6]y[(v_{\max} + 1) * i + (\text{nodenum} + k + 1) + (\text{nodenum} * j)] \\
& \quad + H[7]y[(v_{\max} + 1) * i + (\text{nodenum} + k + (v_{\max} + 2)) \\
& \quad + (\text{nodenum} * j)] \\
& \quad + H[8]y[(v_{\max} + 1) * i + (\text{nodenum} + k + (v_{\max} + 1)) \\
& \quad + (\text{nodenum} * j)] \left. \right], \{k, 1, v_{\max}\}, \{j, 0, \text{layer} - 1\}, \{i, 0, (u_{\max} - 1)\} \left. \right]
\end{aligned}$$

$$\begin{aligned}
& \text{Do} \left[Z[v_{\max} * i + k + (\text{elnum} * j)] \right. \\
& \quad = \text{Simplify} \left[H[1]z[(v_{\max} + 1) * i + k + (\text{nodenum} * j)] \right. \\
& \quad + H[2]z[(v_{\max} + 1) * i + (k + 1) + (\text{nodenum} * j)] \\
& \quad + H[3]z[(v_{\max} + 1) * i + (k + (v_{\max} + 2)) + (\text{nodenum} * j)] \\
& \quad + H[4]z[(v_{\max} + 1) * i + (k + (v_{\max} + 1)) + (\text{nodenum} * j)] \\
& \quad + H[5]z[(v_{\max} + 1) * i + (\text{nodenum} + k) + (\text{nodenum} * j)] \\
& \quad + H[6]z[(v_{\max} + 1) * i + (\text{nodenum} + k + 1) + (\text{nodenum} * j)] \\
& \quad + H[7]z[(v_{\max} + 1) * i + (\text{nodenum} + k + (v_{\max} + 2)) \\
& \quad + (\text{nodenum} * j)] \\
& \quad + H[8]z[(v_{\max} + 1) * i + (\text{nodenum} + k + (v_{\max} + 1)) \\
& \quad + (\text{nodenum} * j)] \left. \right], \{k, 1, v_{\max}\}, \{j, 0, \text{layer} - 1\}, \{i, 0, (u_{\max} - 1)\} \\
& \text{Do} \left[\text{Jmat}[i] = \begin{pmatrix} D[X[i], \xi] & D[Y[i], \xi] & D[Z[i], \xi] \\ D[X[i], \eta] & D[Y[i], \eta] & D[Z[i], \eta] \\ D[X[i], \mu] & D[Y[i], \mu] & D[Z[i], \mu] \end{pmatrix}, \{i, 1, (\text{elnum} * (\text{layer} - 1))\} \right] \\
& \text{Do}[\text{jac}[i] = \text{Det}[\text{Jmat}[i]], \{i, 1, (\text{elnum} * (\text{layer} - 1))\}] \\
& \text{Do}[\text{Jinv}[i] = \text{Inverse}[\text{Jmat}[i]], \{i, 1, (\text{elnum} * (\text{layer} - 1))\}] \\
& \text{Do}[\text{d}\xi\text{d}x[i] = \text{Jinv}[i][[1]][[1]], \{i, 1, (\text{elnum} * (\text{layer} - 1))\}] \\
& \text{Do}[\text{d}\xi\text{d}y[i] = \text{Jinv}[i][[2]][[1]], \{i, 1, (\text{elnum} * (\text{layer} - 1))\}] \\
& \text{Do}[\text{d}\xi\text{d}z[i] = \text{Jinv}[i][[3]][[1]], \{i, 1, (\text{elnum} * (\text{layer} - 1))\}] \\
& \text{Do}[\text{d}\eta\text{d}x[i] = \text{Jinv}[i][[1]][[2]], \{i, 1, (\text{elnum} * (\text{layer} - 1))\}] \\
& \text{Do}[\text{d}\eta\text{d}y[i] = \text{Jinv}[i][[2]][[2]], \{i, 1, (\text{elnum} * (\text{layer} - 1))\}] \\
& \text{Do}[\text{d}\eta\text{d}z[i] = \text{Jinv}[i][[3]][[2]], \{i, 1, (\text{elnum} * (\text{layer} - 1))\}] \\
& \text{Do}[\text{d}\mu\text{d}x[i] = \text{Jinv}[i][[1]][[3]], \{i, 1, (\text{elnum} * (\text{layer} - 1))\}] \\
& \text{Do}[\text{d}\mu\text{d}y[i] = \text{Jinv}[i][[2]][[3]], \{i, 1, (\text{elnum} * (\text{layer} - 1))\}] \\
& \text{Do}[\text{d}\mu\text{d}z[i] = \text{Jinv}[i][[3]][[3]], \{i, 1, (\text{elnum} * (\text{layer} - 1))\}] \\
& \text{Do}[\text{L}[j][i] = D[H[i], \xi]\text{d}\xi\text{d}x[j] + D[H[i], \eta]\text{d}\eta\text{d}x[j] \\
& \quad + D[H[i], \mu]\text{d}\mu\text{d}x[j], \{i, 1, 8\}, \{j, 1, (\text{elnum} * (\text{layer} - 1))\}] \\
& \text{Do}[\text{M}[j][i] = D[H[i], \xi]\text{d}\xi\text{d}y[j] + D[H[i], \eta]\text{d}\eta\text{d}y[j] \\
& \quad + D[H[i], \mu]\text{d}\mu\text{d}y[j], \{i, 1, 8\}, \{j, 1, (\text{elnum} * (\text{layer} - 1))\}]
\end{aligned}$$

$$\text{Do}[Q[j][i] = D[H[i], \xi]d\xi dz[j] + D[H[i], \eta]d\eta dz[j] \\ + D[H[i], \mu]d\mu dz[j], \{i, 1, 8\}, \{j, 1, (\text{elnum} * (\text{layer} - 1))\}]]$$

$$\text{Do}[Bmat[i]$$

$$= (\{\{L[i][1], L[i][2], L[i][3], L[i][4], L[i][5], L[i][6], L[i][7], L[i][8]\}, \{M[i][1], M[i][2], M[i][3], M[i][4], M[i][5], M[i][6], M[i][7], M[i][8]\}\} \\ * (\text{layer} - 1)\})$$

$$\text{Do}[\text{intg}[i] = ((\text{Transpose}[Bmat[i]].Bmat[i])(\text{jac}[i])), \{i, 1, (\text{elnum} \\ * (\text{layer} - 1))\}]]$$

$$q1 = -0.577350269; q2 = -q1; w1 = 1; w2 = 1;$$

$$\text{Do}[KK[i] = (\text{intg}[i] * w1 * w1 * w1/.\{\xi \rightarrow q1, \eta \rightarrow q1, \mu \\ \rightarrow q1\}) + (\text{intg}[i] * w1 * w2 * w1/.\{\xi \rightarrow q1, \eta \rightarrow q2, \mu \\ \rightarrow q1\}) + (\text{intg}[i] * w2 * w1 * w1/.\{\xi \rightarrow q2, \eta \rightarrow q1, \mu \\ \rightarrow q1\}) + (\text{intg}[i] * w2 * w2 * w1/.\{\xi \rightarrow q2, \eta \rightarrow q2, \mu \\ \rightarrow q1\}) + (\text{intg}[i] * w1 * w1 * w2/.\{\xi \rightarrow q1, \eta \rightarrow q1, \mu \\ \rightarrow q2\}) + (\text{intg}[i] * w1 * w2 * w2/.\{\xi \rightarrow q1, \eta \rightarrow q2, \mu \\ \rightarrow q2\}) + (\text{intg}[i] * w2 * w1 * w2/.\{\xi \rightarrow q2, \eta \rightarrow q1, \mu \\ \rightarrow q2\}) + (\text{intg}[i] * w2 * w2 * w2/.\{\xi \rightarrow q2, \eta \rightarrow q2, \mu \\ \rightarrow q2\}), \{i, 1, (\text{elnum} * (\text{layer} - 1))\}]]$$

$$\text{Do}[K[e][i][j] = KK[e][i][j], \{e, 1, (\text{elnum} * (\text{layer} - 1))\}, \{i, 1, 8\}, \{j, 1, 8\}]$$

$$\text{col1} = \{\{1, 1\} \rightarrow K[1][1][1], \{((\text{vmax} + 1) * \text{umax}) + 1, ((\text{vmax} + 1) * \text{umax}) + 1\} \\ \rightarrow K[1][4][4], \{\text{nodenum}, \text{nodenum}\} \\ \rightarrow K[\text{elnum}][3][3]\};$$

$$\text{kose} = \{\{\text{vmax}, \text{vmax} + 1\} \rightarrow K[\text{vmax}][1][2], \{\text{vmax} + 1, \text{vmax} + 1\} \\ \rightarrow K[\text{vmax}][2][2], \{2\text{vmax} + 1, \text{vmax} + 1\} \\ \rightarrow K[2][4][2], \{2\text{vmax} + 2, \text{vmax} + 1\} \rightarrow K[2][3][2]\};$$

$$\text{Do}[\text{col2}[\text{vmax} * i + j] = \{((\text{vmax} + 1) * i + j), ((\text{vmax} + 1) * i + j + \text{vmax} + 2)\} \\ \rightarrow (K[\text{vmax} * i + j][1][3]), \{j, 1, \text{vmax}\}, \{i, 0, (\text{umax} - 1)\}]$$

$$\text{Do}[\text{col3}[(\text{vmax} - 1) * i + j] \\ = \{((\text{vmax} + 1) * i + j + 1), ((\text{vmax} + 1) * i + j + \text{vmax} + 2)\} \\ \rightarrow (K[\text{vmax} * i + j][2][3] + K[\text{vmax} * i + j + 1][1][4]), \{j, 1, \text{vmax} \\ - 1\}, \{i, 0, \text{umax} - 1\}]$$

$$\begin{aligned}
& \text{Do}[\text{col4}[(\text{vmax}) * i + j] \\
& \quad = \{((\text{vmax} + 1) * i + j + 1), ((\text{vmax} + 1) * i + j + \text{vmax} + 1)\} \\
& \quad \rightarrow (K[\text{vmax} * i + j][2][4]), \{j, 1, \text{vmax}\}, \{i, 0, \text{umax} - 1\}] \\
& \text{Do}[\text{col5}[(\text{vmax}) * i + j] \\
& \quad = \{((\text{vmax} + 1) * (i + 1) + j), ((\text{vmax} + 1) * (i + 1) + j + 1)\} \\
& \quad \rightarrow (K[\text{vmax} * i + j][4][3] \\
& \quad + K[\text{vmax} * i + j + \text{vmax}][1][2]), \{j, 1, \text{vmax}\}, \{i, 0, \text{umax} - 2\}] \\
& \text{Do}[\text{kosegen}[(\text{vmax} - 1) * i + j] \\
& \quad = \{((\text{vmax} + 1) * i + j + \text{vmax} + 2), ((\text{vmax} + 1) * i + j + \text{vmax} \\
& \quad + 2)\} \\
& \quad \rightarrow (K[\text{vmax} * i + j][3][3] + K[\text{vmax} * i + j + 1][4][4] \\
& \quad + K[\text{vmax} * i + \text{vmax} + j][2][2] \\
& \quad + K[\text{vmax} * i + \text{vmax} + j + 1][1][1]), \{j, 1, \text{vmax} - 1\}, \{i, 0, \text{umax} \\
& \quad - 1\}] \\
& \text{Do}[\text{col6}[(\text{vmax}) * i + j] \\
& \quad = \{((\text{vmax} + 1) * i + j + \text{vmax} + 2), ((\text{vmax} + 1) * i + j + \text{vmax} \\
& \quad + 1)\} \\
& \quad \rightarrow K[\text{vmax} * i + j][3][4] \\
& \quad + K[\text{vmax} * i + \text{vmax} + j][2][1], \{j, 1, \text{vmax}\}, \{i, 0, \text{umax} - 2\}] \\
& \text{Do}[\text{col7}[(\text{vmax}) * i + j] \\
& \quad = \{((\text{vmax} + 1) * i + j + \text{vmax} + 1), ((\text{vmax} + 1) * i + j + 1)\} \\
& \quad \rightarrow K[\text{vmax} * i + j][4][2], \{j, 1, \text{vmax}\}, \{i, 0, \text{umax} - 1\}] \\
& \text{Do}[\text{col8}[(\text{vmax} - 1) * i + j] \\
& \quad = \{((\text{vmax} + 1) * i + j + \text{vmax} + 2), ((\text{vmax} + 1) * i + j + 1)\} \\
& \quad \rightarrow K[(\text{vmax}) * i + j][3][2] \\
& \quad + K[(\text{vmax}) * i + j + 1][4][1], \{j, 1, \text{vmax} - 1\}, \{i, 0, \text{umax} - 1\}] \\
& \text{Do}[\text{col9}[\text{vmax} * i + j] = \{((\text{vmax} + 1) * i + j + \text{vmax} + 2), ((\text{vmax} + 1) * i + j)\} \\
& \quad \rightarrow (K[\text{vmax} * i + j][3][1]), \{j, 1, \text{vmax}\}, \{i, 0, (\text{umax} - 1)\}] \\
& \text{Do}[\text{col10}[i] = \{((\text{vmax} + 1) * \text{umax}) + i, ((\text{vmax} + 1) * \text{umax}) + i + 1\} \\
& \quad \rightarrow K[((\text{umax} - 1) * \text{vmax}) + i][4][3], \{i, 1, \text{vmax}\}]
\end{aligned}$$

$\text{Do}[\text{col11}[i] = \{((\text{vmax} + 1) * \text{umax}) + i + 1, ((\text{vmax} + 1) * \text{umax}) + i\}$
 $\quad \rightarrow K[(\text{umax} - 1) * \text{vmax} + i][3][4], \{i, 1, \text{vmax}\}]$

$\text{Do}[\text{col12}[i] = \{((\text{vmax} + 1) * \text{umax}) + i + 1, ((\text{vmax} + 1) * \text{umax}) + i + 1\}$
 $\quad \rightarrow K[(\text{umax} - 1) * \text{vmax} + i][3][3]$
 $\quad + K[(\text{umax} - 1) * \text{vmax} + i + 1][4][4], \{i, 1, \text{vmax} - 1\}]$

$\text{Do}[a[i] = \{i, i + 1\} \rightarrow K[i][1][2], \{i, 1, \text{vmax}\}]$

$\text{Do}[g[i] = \{i + 1, i + 1\} \rightarrow (K[i][2][2] + K[i + 1][1][1]), \{i, 1, \text{vmax} - 1\}]$

$\text{Do}[c[i] = \{i + 1, i\} \rightarrow K[i][2][1], \{i, 1, \text{vmax}\}]$

$\text{Do}[d[i + 1] = \{(\text{vmax} + 1) * i + 1, (\text{vmax} + 1) * i + (\text{vmax} + 1) + 1\}$
 $\quad \rightarrow K[\text{vmax} * i + 1][1][4], \{i, 0, \text{umax}\}]$

$\text{Do}[e[i + 1] = \{(\text{vmax} + 1) * i + (\text{vmax} + 1) + 1, (\text{vmax} + 1) * i + 1\}$
 $\quad \rightarrow K[\text{vmax} * i + 1][4][1], \{i, 0, \text{umax}\}]$

$\text{Do}[f[i + 1] = \{(\text{vmax} + 1) * i + (\text{vmax} + 1) + 1, (\text{vmax} + 1) * i + (\text{vmax} + 1) + 1\}$
 $\quad \rightarrow K[\text{vmax} * i + 1][4][4]$
 $\quad + K[\text{vmax} * i + 1 + \text{vmax}][1][1], \{i, 0, \text{umax} - 2\}]$

$\text{Do}[h[i] = \{(\text{vmax} + 1) * i, (\text{vmax} + 1) * (i + 1)\} \rightarrow K[\text{vmax} * i][2][3], \{i, 1, \text{umax}\}]$

$\text{Do}[l[i] = \{(\text{vmax} + 1) * (i + 1), (\text{vmax} + 1) * i\} \rightarrow K[\text{vmax} * i][3][2], \{i, 1, \text{umax}\}]$

$\text{Do}[k[i + 1] = \{(\text{vmax} + 1) * (i + 2), (\text{vmax} + 1) * (i + 2)\}$
 $\quad \rightarrow (K[\text{vmax} * (i + 1)][3][3] + K[\text{vmax} * (i + 2)][2][2]), \{i, 0, \text{umax}$
 $\quad - 2\}]$

$\text{FR} = \text{Array}[a, \text{vmax}]; \text{SR} = \text{Array}[g, \text{vmax} - 1]; \text{TR} = \text{Array}[c, \text{vmax}];$

$\text{FoR} = \text{Array}[d, \text{umax}]; \text{FiR} = \text{Array}[e, \text{umax}]; \text{SiR} = \text{Array}[f, \text{umax} - 1];$

$\text{SeR} = \text{Array}[h, \text{umax}]; \text{ER} = \text{Array}[l, \text{umax}]; \text{NR} = \text{Array}[k, \text{umax} - 1];$

$\text{ThR} = \text{Array}[\text{col2}, (\text{vmax} * (\text{umax} - 1)) + \text{vmax}];$

$\text{ForR} = \text{Array}[\text{col3}, ((\text{vmax} - 1) * (\text{umax} - 1)) + \text{vmax} - 1];$

$\text{FivR} = \text{Array}[\text{col4}, (\text{vmax} * (\text{umax} - 1)) + \text{vmax}];$

$\text{SixR} = \text{Array}[\text{col5}, (\text{vmax} * (\text{umax} - 2)) + \text{vmax}];$

$\text{Kosegen} = \text{Array}[\text{kosegen}, ((\text{vmax} - 1) * (\text{umax} - 2)) + \text{vmax} - 1];$

$\text{SevR} = \text{Array}[\text{col6}, (\text{vmax} * (\text{umax} - 2)) + \text{vmax}];$

$\text{EiR} = \text{Array}[\text{col7}, (\text{vmax} * (\text{umax} - 1)) + \text{vmax}];$

$\text{NiR} = \text{Array}[\text{col8}, ((\text{vmax} - 1) * (\text{umax} - 1)) + \text{vmax} - 1];$

$\text{TeR} = \text{Array}[\text{col9}, (\text{vmax} * (\text{umax} - 1)) + \text{vmax}];$

```

ToR = Array[col10, vmax]; TtR = Array[col11, vmax]; TFR
      = Array[col12, vmax - 1];
Stf[1][1]
= Join[FR, SR, TR, FoR, FiR, SiR, SeR, ER, NR, col1, kose, ThR, ForR, FivR, SixR, Kosegen,
      SevR, EiR, NiR, TeR, ToR, TtR, TFR]
Do[STF[i][i] = Stf[1][1]/.K[x_] → K[x + elnum * i], {i, 1, layer - 2}]
Do[STTF[j + 1][j + 1] = Stf[1][1]/.K[x_][y_][z_]
      → K[x + elnum * j][y + 4][z + 4], {j, 0, layer - 1}]
Do[top[i][i] = SparseArray[STF[i][i]], {i, 1, layer - 2}]
Do[tap[i][i] = SparseArray[STTF[i][i]], {i, 1, layer - 2}]
Do[key[i + 1][i + 1] = top[i][i] + tap[i][i], {i, 1, layer - 2}]
Stf[1][2] = Stf[1][1]/.K[x_][y_][z_] → K[x][y][z + 4];
key[1][1] = SparseArray[Stf[1][1]];
Do[Stf[i][i + 1] = Stf[1][1]/.K[x_][y_][z_]
      → K[x + elnum * j][y][z + 4], {i, 1, layer - 1}, {j = i - 1}]
Do[key[i][i + 1] = SparseArray[Stf[i][i + 1]], {i, 1, layer - 1}]
Do[key[i + 2][i + 1] = Transpose[key[i + 1][i + 2]], {i, 0, layer - 2}]
Vf = 1; V[v] = 8; kc = 0.025; fi = 0; volt = 10;
Alan = NIntegrate[unit, {u, 0, 1}, {v, 0, 1}]/elnum;
c[1] = Alan * (Vf/(V[v] * kc)) * Cos[θ[1]] * volt;
Do[c[p] = 4 * Alan * (Vf/(V[v] * kc)) * Cos[θ[p]]
      * volt, {k, 1, (vmax - 1)}, {i, 1, (umax - 1)}, {p
      = ((vmax + 1) * i) + (k + 1)}]
Do[c[p] = 2 * Alan * (Vf/(V[v] * kc)) * Cos[θ[p]]
      * volt, {i, 1, (umax - 1)}, {p = ((vmax + 1) * i) + 1}]
Do[c[p] = 2 * Alan * (Vf/(V[v] * kc)) * Cos[θ[p]] * volt, {i, 1, (umax - 1)}, {p
      = ((vmax + 1) * (i + 1))}]
Do[c[i + 1] = 2 * Alan * (Vf/(V[v] * kc)) * Cos[θ[i + 1]] * volt, {i, 1, vmax}]
Do[c[i] = 2 * Alan * (Vf/(V[v] * kc)) * Cos[θ[i]]
      * volt, {i, (nodenum - (vmax - 1)), (nodenum - 1)}]
c[vmax + 1] = Alan * (Vf/(V[v] * kc)) * Cos[θ[vmax + 1]] * volt;
c[nodenum - vmax] = Alan * (Vf/(V[v] * kc)) * Cos[θ[nodenum - vmax]] * volt;

```

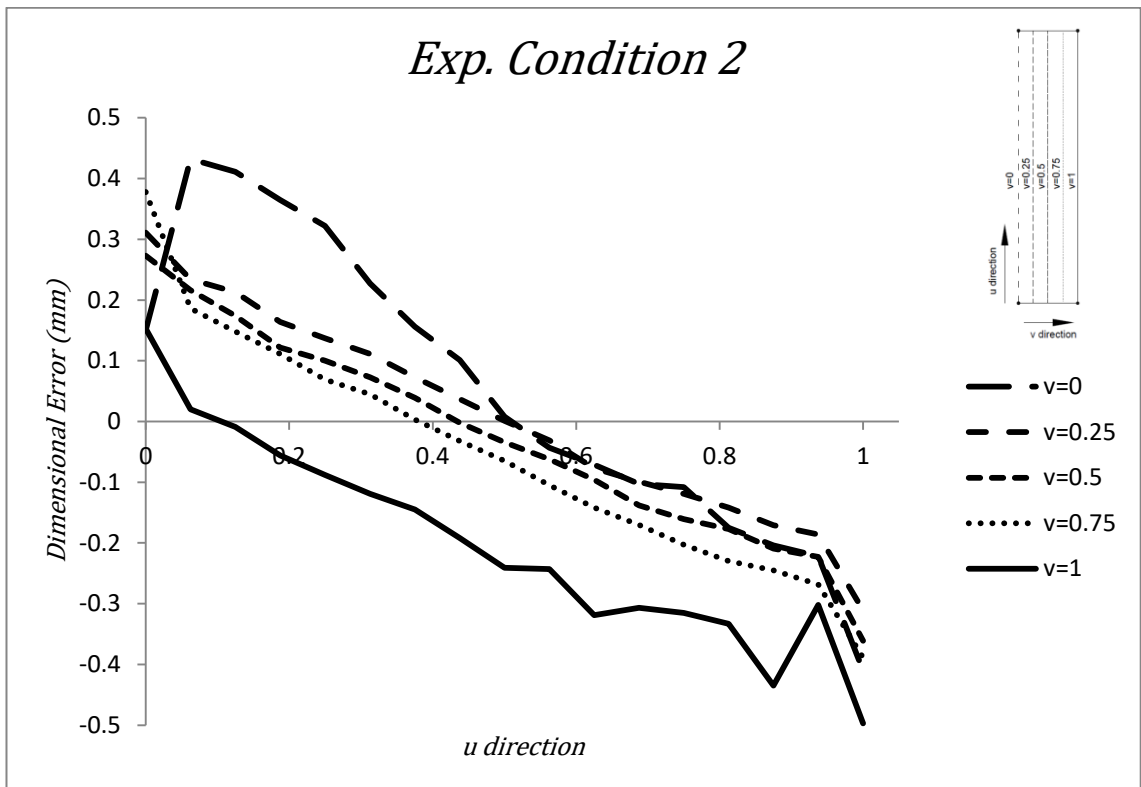
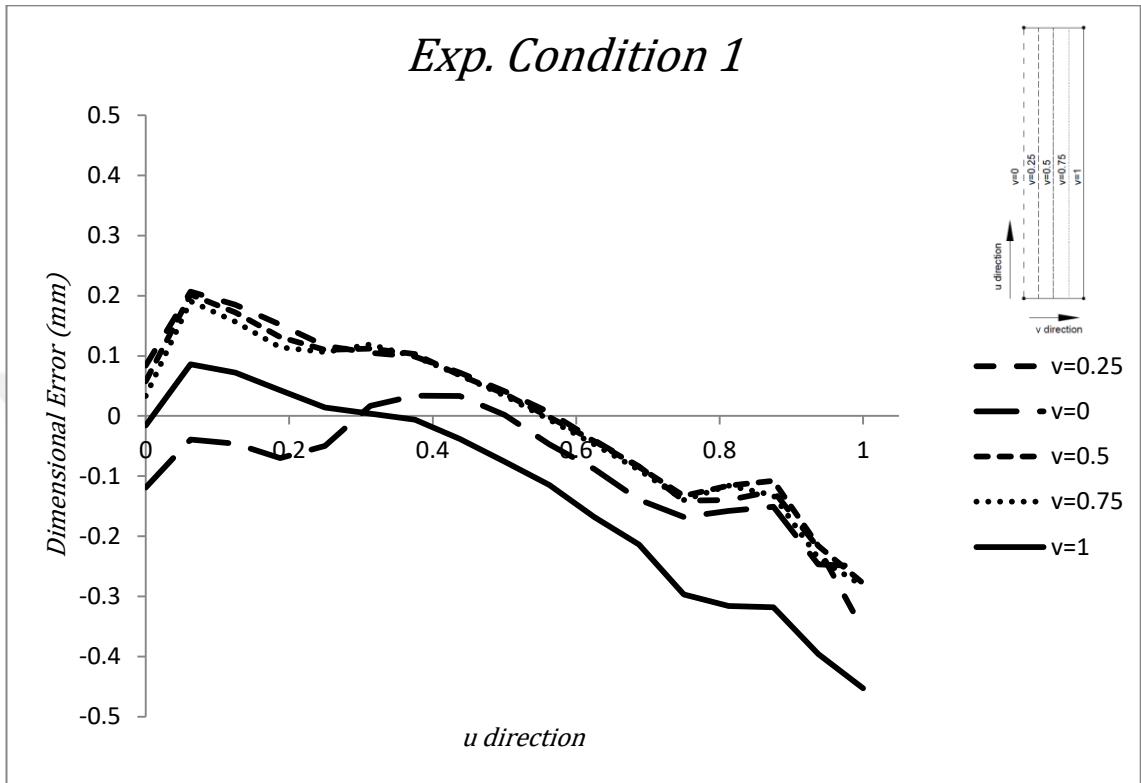
```

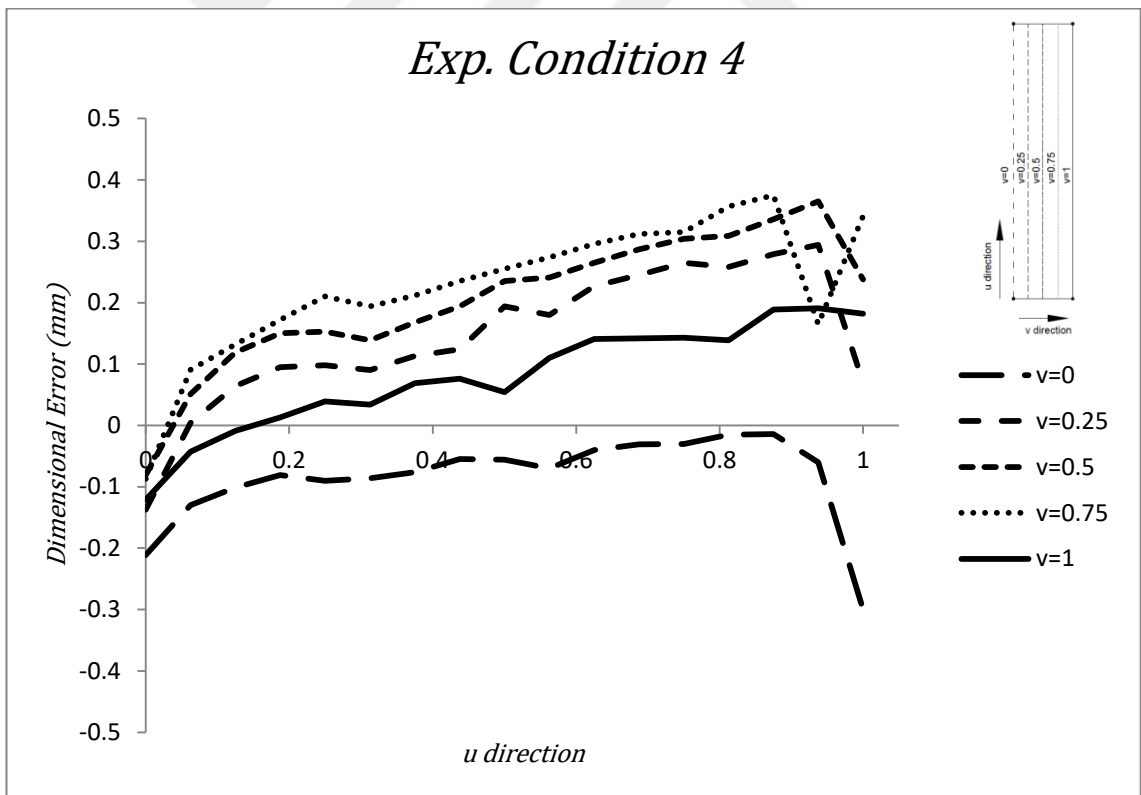
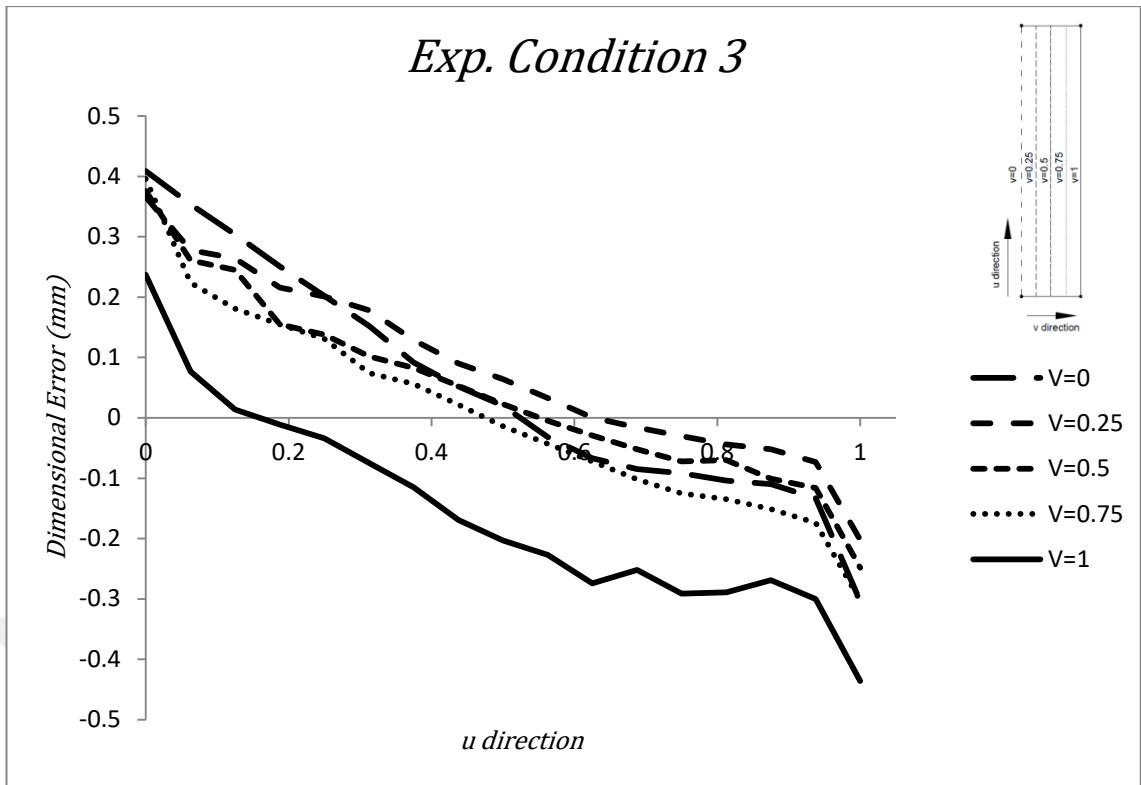
c[nodenum] = Alan * (Vf/(V[v] * kc)) * Cos[θ[nodenum]] * volt;
cc = Array[c, nodenum];
Do[U[i] = fi, {i, nodenum}]
φ[1] = Array[U, nodenum];
φ[2] = -Inverse[key[1][2]].(key[1][1]. φ[1] - cc);
φ[3] = -Inverse[key[2][3]].(key[2][1]. φ[1] + key[2][2]. φ[2]);
φ[4] = -Inverse[key[3][4]].(key[3][2]. φ[2] + key[3][3]. φ[3]);
φ[5] = -Inverse[key[4][5]].(key[4][3]. φ[3] + key[4][4]. φ[4]);

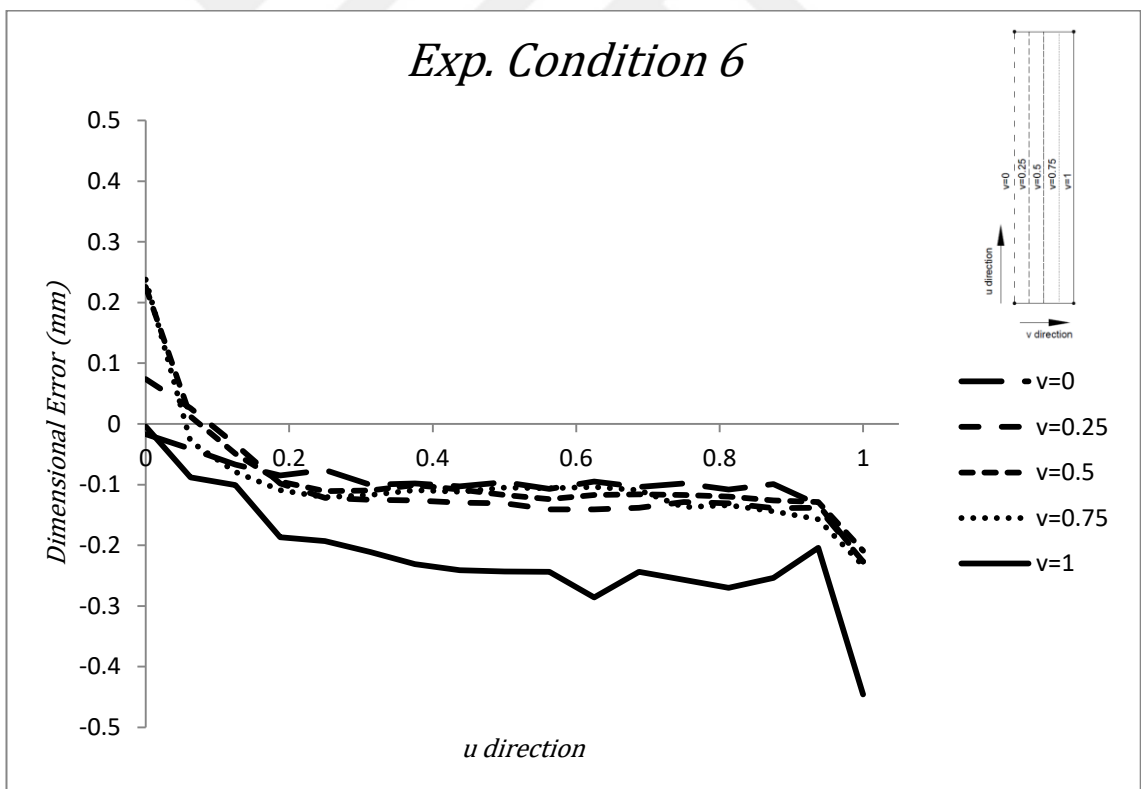
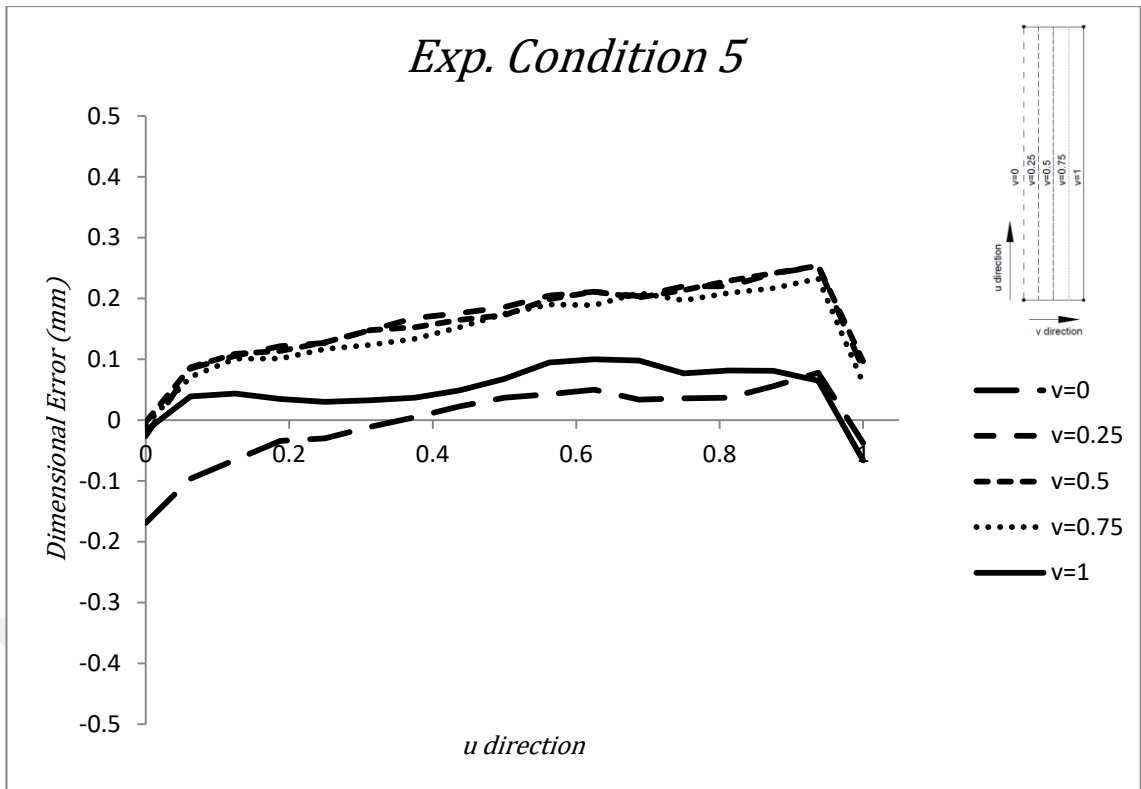
```

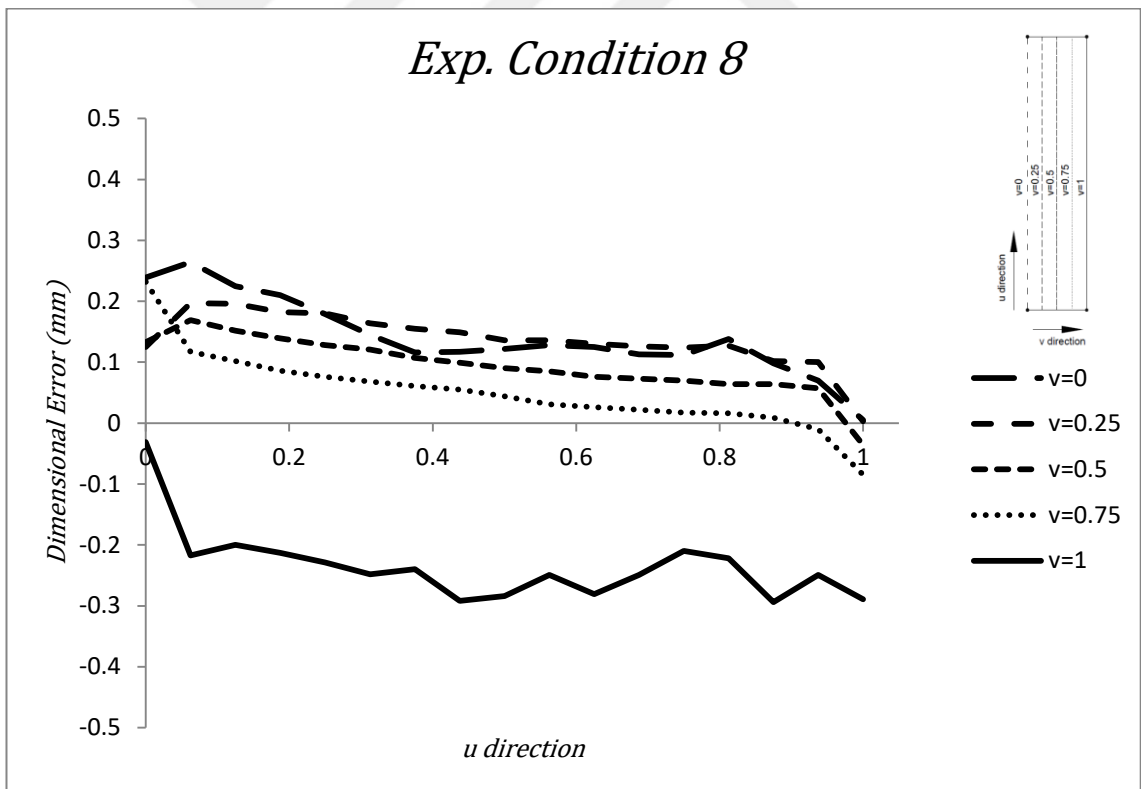
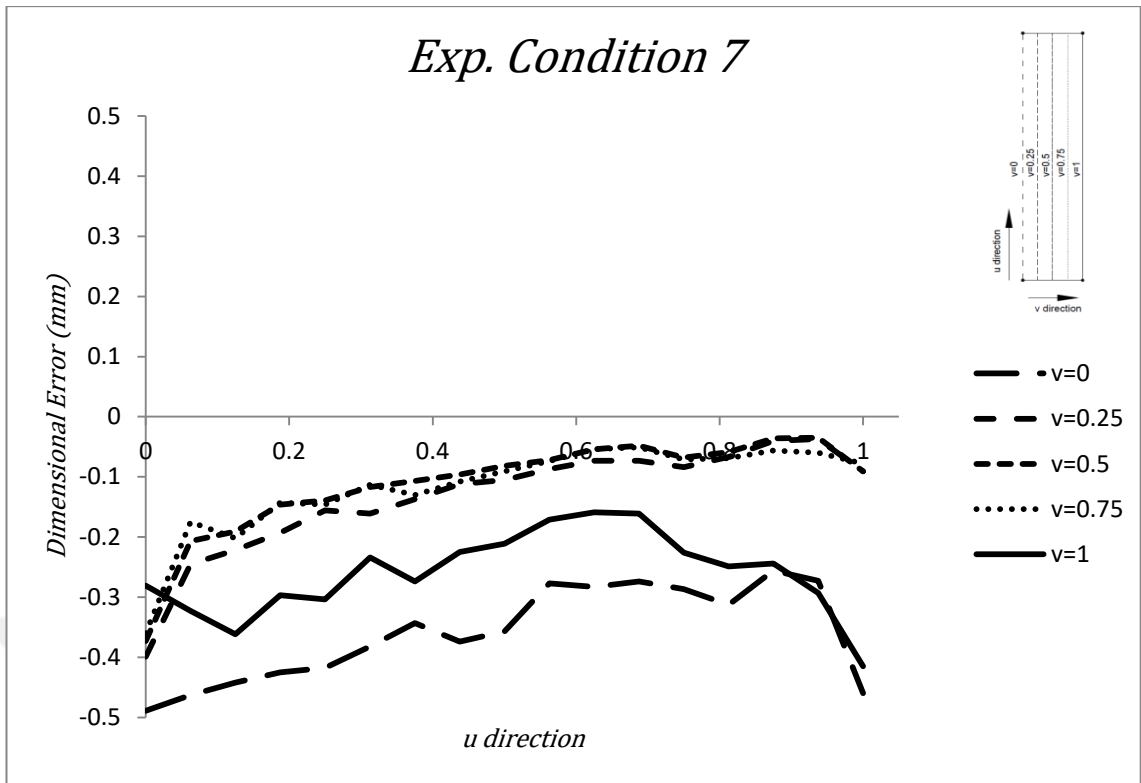


Appendix C: Variation of DE Along u Direction for Experimental Conditions

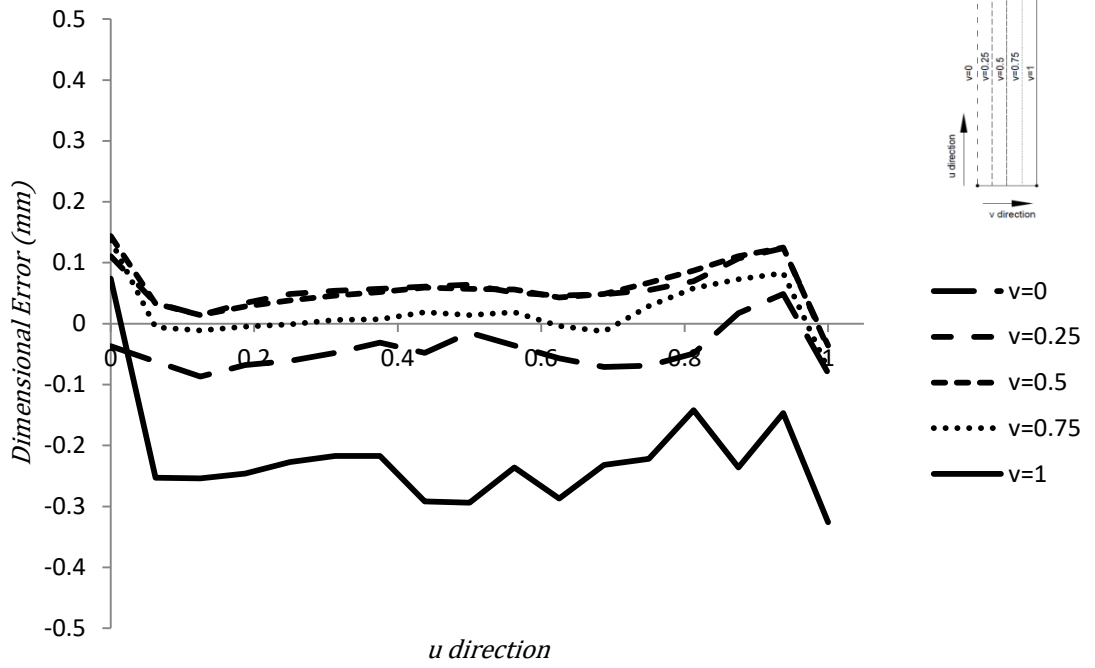








Exp. Condition 9



CURRICULUM VITAE

PERSONAL INFORMATION

Name and Surname: Hasan DEMİRTAŞ

Nationality: Turkish

Birth place and date: KONYA/Doğanhisar - 08.10.1984

Marital status: Married

Phone number: +905433672984

Email: hdemirtas@kilis.edu.tr

EDUCATION

	Graduate school	Year
Master	Niğde Ömer Halisdemir University	2009
Bachelor	Niğde Ömer Halisdemir University	2006
High School	Akşehir High School	2002

Work experience

	Place	Enrollment
2010-Present	Kilis 7 Aralık University	Instructor
2006-2010	Erman Doğalgaz	Supervising Engineer

PUBLICATIONS

Refereed Journal Publications

Demirtas, H., Yilmaz, O., Kanber, B., (2017). A simplified mathematical model development for the design of free-form cathode surface in electrochemical machining, *Machining Science and Technology: An International Journal*, **21**(1), 157-173.

Demirtas, H., Yilmaz, O., Kanber, B., (2017). Investigation of Machining Parameter Effects in Electrochemical Machining Process for Macro/Micro Manufacturing, *Makina Tasarım ve İmalat Dergisi*, **15**(1), 11-18.

Refereed Conference Proceedings

Demirtas, H., Yilmaz, O., Kanber, B., (2013). Cathode Design For Electro-Chemical Machining of Turbine Blades, *4. Ulusal Talaşlı İmalat Sempozyumu*, Aydın, Turkey.

Demirtas, H., Yilmaz, O., Kanber, B., (2016). Development of a Desktop Size Electrochemical Machine for Micro/Macro Manufacturing, *The 17th International Conference on Machine Design and Production*, Bursa Turkey.

Demirtas, H., Yilmaz, O., Kanber, B., (2017). Experimental Investigation of Cavitation, Short-Circuit and Oxide Layer Formation in Electrochemical Machining of Free-Form Surfaces, *8th International Symposium on Machining*, Antalya, Turkey.

FOREIGN LANGUAGE

English, UDS, 65, 2009.

HOBBIES